

DISS. ETH NO. 26529

Accelerating High-Dimensional Magnetic Resonance Flow Imaging

A thesis submitted to attain the degree of

DOCTOR OF SCIENCES of ETH ZURICH

(Dr. sc. ETH Zurich)

presented by

JONAS STEFFEN WALHEIM

MSc, Karlsruhe Institute of Technology

born on 12.07.1989

citizen of Germany

accepted on the recommendation of

Prof. Dr. Sebastian Kozerke

Prof. Dr. Michael Markl

2020

Abstract

The quantification of turbulent flow by phase-contrast Magnetic Resonance Imaging (MRI) enables the assessment of cardiac hemodynamics and holds promise for improvements in the diagnosis of valvular pathologies. However, long scan times hamper wide-spread in-vivo use of the technique. Thus, this work focuses on accelerating imaging of valvular flow. To this end, more efficient acquisition methods are developed by exploiting data redundancies along multiple dimensions enabling faster and more robust flow quantification. Moreover, the improved scan efficiency is utilized to extend the sequence for quantification of both mean and turbulent flows including the Reynolds stress tensor.

In previous work it has been suggested that the relatively simple partial Fourier technique can be used to accelerate flow MRI. Here, it is shown that spatial phase fluctuations, which occur when imaging turbulent flows, lead to inadequacy of the underlying model assumption which is based on Hermitian symmetry. Thus, the reconstruction cannot recover missing samples without producing image artifacts highlighting the need for more advanced acceleration techniques.

As part of the present thesis, 5D Flow MRI is introduced to address scan inefficiencies due to respiratory motion while enabling predictable scan times. A pseudo-radial Cartesian Golden angle sampling trajectory is proposed to capture data from the entire respiratory cycle and to attribute them to discrete respiratory states. Reconstruction of highly undersampled data is performed by exploiting redundancies between cardiac phases and respiratory states. As a result, a fixed scan time of 4 minutes is achieved for multi-point assessment of mean and turbulent flow. The concept is demonstrated in an in-vivo study with 9 subjects.

To enable quantification of the Reynolds stress tensor, the 5D Flow MRI sequence is extended with additional velocity encoding directions. Multipoint encoding ensures accurate turbulence assessment in the value range of turbulence intensities found in healthy and pathological flows. A numerical study demonstrates high precision but moderate overestimation of values at achievable signal-to-noise ratios and resolution. In an in-vivo study the ability to quantify turbulent flow downstream of a bio-prosthetic heart valves in a scan time of 10 minutes is shown.

While enabling faster scans, accelerated imaging methods typically come with the drawback of a considerable increase in reconstruction times. To enable rapid reconstruction of undersampled data, a deep neural network architecture is presented. Training is performed with retrospectively undersampled flow data which were acquired in healthy volunteers. Results reveal that the network accurately reconstructs both normal and pathological flows. Further, an in-vivo study with 7 healthy subjects shows good agreement of flow parameters with reference measurements.

To summarize, a framework for high-dimensional flow imaging has been implemented and validated. The methodology allows for fast, robust and comprehensive mean and turbulent flow quantification in vivo. Examination of turbulent kinetic energy can be performed within 4 minutes while quantification of the entire Reynolds stress tensor is possible within 10 minutes. To further facilitate clinical use, rapid image reconstruction based on neural networks is presented which can be readily extended to higher dimensions in the future.

Kurzfassung

Die Quantifizierung von turbulentem Fluss mittels Phasenkontrastmagnetresonanztomographie ermöglicht die Beurteilung der Hämodynamik des Herzens und verspricht Verbesserungen in der Diagnose von Herzklappenerkrankungen. Lange Messzeiten verhindern jedoch eine weitverbreitete Nutzung der Technik. Darum ist diese Arbeit auf die beschleunigte Bildgebung von Fluss durch Herzklappen ausgerichtet. Effizientere Akquisitionsmethoden werden vorgestellt, die Datenredundanzen entlang mehrerer Dimensionen ausnutzen und damit eine schnellere und robustere Flussquantifizierung ermöglichen. Die resultierende, erhöhte Effizienz der Messung wird darüber hinaus genutzt, um die Sequenz für die Quantifizierung von gemitteltem und turbulentem Fluss inklusive des Reynolds'schen Spannungstensors zu erweitern.

In älteren Arbeiten wurde vorgeschlagen, dass die relativ einfache «partial Fourier» Technik genutzt werden kann, um Flussbildgebung zu beschleunigen. Hier wird gezeigt, dass räumliche Phasenfluktuationen, wie sie bei der Messung von turbulentem Fluss auftreten, zur einer Diskrepanz der zu Grunde liegenden Modellannahme führen, welche auf hermetischer Symmetrie beruhen. Daher führt diese Rekonstruktionsmethode zu starken Bildartefakten. Entsprechend besteht die Notwendigkeit der Verwendung von fortgeschrittenen Beschleunigungsmethoden.

Als Teil der vorliegenden Dissertation wird die 5-dimensionale Flussbildgebung vorgestellt. Das Verfahren erlaubt es, Ineffizienzen, die durch Atembewegung entstehen, zu reduzieren und damit Messzeiten vorherzusagen bzw. vorab festzulegen. Eine pseudo-radiale kartesische Abtastung mit goldenem Winkel gestattet es, Daten des gesamten Atemzyklus zu nutzen, indem diese diskreten Atemzuständen zugewiesen werden. Die Rekonstruktion der stark unterabgetasteten Daten erfolgt, indem Korrelationen zwischen verschiedenen Herzphasen und Atemzuständen ausgenutzt werden. Als Ergebnis resultiert eine konstante Messzeit von 4 Minuten für eine Multipunktmessung von gemitteltem und turbulentem Fluss. Das Konzept wird in einer in vivo Studie mit 9 Probanden demonstriert.

Um die Quantifizierung des Reynolds'schen Spannungstensors zu ermöglichen, wird eine erweiterte 5D-Fluss-Sequenz mit zusätzlichen Geschwindigkeitskodierungen vorgestellt. Die Multipunktkodierung sorgt für eine präzise Turbulenzquantifizierung in dem Wertebereich von Turbulenzintensitäten, welcher in gesundem sowie pathologischem Fluss ermittelt wurde. Eine numerische Studie zeigt eine hohe Präzision aber eine moderate Überschätzung der Werte für realistische Signal-zu-Rausch-Verhältnisse sowie räumliche Auflösungen. In einer in vivo Studie wird die Fähigkeit zur Quantifizierung von turbulentem Fluss hinter bioprothetischen Herzklappen bei einer Messzeit von 10 Minuten gezeigt.

Beschleunigte Bildgebungsmethoden bringen üblicherweise den Nachteil einer deutlichen Zunahme der Rekonstruktionszeit mit sich. Um eine schnelle Rekonstruktion der unterabgetasteten Daten zu ermöglichen, wird eine neuronale Netzwerkarchitektur präsentiert. Das Training erfolgt mit retrospektive unterabgetasteten Flussdaten gesunder Probanden. Die Ergebnisse zeigen, dass das Netzwerk sowohl normalen als auch pathologischen Fluss präzise rekonstruieren kann. Weiterhin zeigt eine in vivo Studie mit 7 gesunden Probanden eine gute Übereinstimmung der Flussparameter mit Referenzwerten.

Zusammenfassend umfasst die vorliegende Arbeit wesentliche Beiträge für die hochdimensionale Flussbildgebung. Die Methodik ermöglicht eine schnelle, robuste und umfassende Flussquantifizierung in vivo. Eine Untersuchung der turbulenten kinetischen Energie kann innerhalb von 4 Minuten durchgeführt werden, während die Quantifizierung des gesamten Reynolds'schen Spannungstensors innerhalb von 10 Minuten möglich ist. Die zukünftige klinische Nutzung wird unterstützt durch eine schnelle Bildrekonstruktion basierend auf neuronalen Netzwerken, welche in Zukunft leicht auf weitere Dimensionen erweitert werden kann.

Table of contents

| | |
|--|-----------|
| Abstract | 1 |
| Kurzfassung | 2 |
| Chapter 1 Introduction | 7 |
| 1.1 Contribution of the thesis | 8 |
| Chapter 2 Phase contrast magnetic resonance imaging | 10 |
| 2.1 Phase Contrast Encoding of Laminar Flow | 10 |
| 2.1.1 Velocity Encoding and Velocity-to-Noise-Ratio | 11 |
| 2.1.2 Cine Phase Contrast MRI | 12 |
| 2.1.3 4D Flow MRI | 12 |
| 2.1.4 Segmented k-Space Acquisition | 13 |
| 2.1.5 Respiratory Navigation | 13 |
| 2.2 Turbulent Flow | 13 |
| 2.2.1 Generalized Phase Contrast Magnetic Resonance Imaging | 14 |
| 2.2.2 Turbulent Kinetic Energy | 15 |
| 2.2.3 Reynolds Stress Tensor | 16 |
| Chapter 3 Accelerated Phase Contrast MRI | 17 |
| 3.1 Partial Fourier | 17 |
| 3.2 Parallel Imaging | 19 |
| 3.3 k-t BLAST and k-t PCA | 21 |
| 3.4 Compressed Sensing | 21 |
| 3.4.1 Undersampling Strategies | 22 |
| 3.4.2 Sparse Transform Domains for Flow Imaging..... | 23 |
| 3.5 Deep Learning | 26 |
| Chapter 4 On the Limitations of Partial Fourier Acquisition in Phase-Contrast MRI of Turbulent Kinetic Energy | 30 |
| 4.1 Introduction | 30 |
| 4.2 Theory | 31 |
| 4.3 Methods | 34 |
| 4.4 Results | 37 |
| 4.5 Discussion | 37 |
| 4.6 Conclusion | 42 |
| 4.7 Acknowledgements | 42 |

| | | |
|---|---------------------------------|----|
| 4.8 | Supplementary Information | 42 |
| Chapter 5 Multipoint 5D Flow Imaging - Accelerated Cardiac- and Respiratory-Motion | | |
| Resolved Mapping of Mean and Turbulent Velocities..... 45 | | |
| 5.1 | Background | 45 |
| 5.2 | Methods..... | 46 |
| 5.3 | Results | 54 |
| 5.4 | Discussion | 59 |
| 5.5 | Conclusion..... | 62 |
| 5.6 | Acknowledgements..... | 63 |
| Chapter 6 Comprehensive Turbulence Assessment with 5D flow Tensor MRI..... 64 | | |
| 6.1 | Introduction | 64 |
| 6.2 | Results | 66 |
| 6.3 | Discussion | 70 |
| 6.4 | Methods..... | 73 |
| 6.5 | Acknowledgements..... | 78 |
| Chapter 7 A Deep Variational Network for Rapid 4D flow MRI Reconstruction..... 80 | | |
| 7.1 | Introduction | 80 |
| 7.2 | FlowVN | 82 |
| 7.3 | Results | 84 |
| 7.4 | Discussion | 86 |
| 7.5 | Methods..... | 89 |
| 7.6 | Supplementary Materials | 94 |
| Chapter 8 Summary | | |
| 8.1 Discussion | | |
| 8.2 Outlook..... | | |
| Chapter 9 References..... 99 | | |
| Chapter 10 Acknowledgements | | |
| Chapter 11 List of Publications..... 118 | | |
| Chapter 12 Curriculum Vitae.....Fehler! Textmarke nicht definiert. | | |

Chapter 1 Introduction

Four-dimensional (4D) flow Magnetic Resonance Imaging (MRI) provides spatiotemporally resolved quantitative assessment of flow and thus enables the comprehensive assessment of hemodynamic parameters in the heart and greater vessels [1]. Various applications with clinical relevance have emerged in recent years, including the characterization of changes of mean and peak velocities [2], flow displacement [3], [4], vorticity and helicity [5], [6], wall shear rates [7]–[9], relative pressure gradients [10]–[12], pulse wave velocities [13]–[15], and viscous energy losses [16].

In conventional 4D Flow MRI, turbulent velocity fluctuations are typically ignored. However, turbulence can be considerable in pathological flows [17] with turbulent energy losses being a major contributor to increased workload for the ventricle [18]. Moreover, neglecting turbulence in the calculation of relative pressure gradients can lead to inaccurate estimates [19].

It has been suggested to derive statistical surrogates of intra-voxel turbulence from the intra-voxel phase dispersion of velocity encoded measurements [20]. To this end, turbulent kinetic energy (TKE) can be gauged, which indicates how much energy is stored in turbulent velocity fluctuations. First clinical studies have already demonstrated the potential of TKE quantification with 4D Flow MRI for the assessment of stenotic heart valves [21], [22] and in dilated cardiomyopathy [23].

The use of velocity encoding schemes, similar to principles used in diffusion tensor imaging [24], enables the quantification of the Reynolds stress tensor (RST) [25]. Accordingly, a comprehensive assessment of turbulent flow can be provided offering promising clinical use cases such as improved mapping of pressure gradients [19], new clinical parameters for the assessment of stenotic heart valves [26] or identification of elevated shear stresses which indicate an increased risk of hemolysis [27].

While first clinical studies have been performed to assess TKE in patients [22], [23], clinical adaptation is still hampered by the long scan times. Moreover, RST assessment has been mostly limited to in-vitro applications [19], [27]–[29] as required modifications to the sequence design further prolong scan time. Hitherto, no in vivo studies of the RST have been reported in the journal literature.

In order to foster and translate turbulence assessment using MRI to a wider clinical community, significant reductions in scan time are indispensable. A number of approaches exist to exploit redundant structures in the data in order to reconstruct images from a reduced number of measurements, including concepts based on Hermitian symmetry [30], [31], sparsity [32] or low-rankedness of data [33]–[35]. Moreover, recent advances in respiratory motion resolved imaging [36] hold promise to address scan inefficiencies and limited robustness as a result of respiratory motion in vivo.

The aim of the present thesis is to lay the foundation for clinical adaptation of mean and turbulent flow assessment using MRI. To this end, different reconstruction methods and respiratory motion resolved imaging are investigated and developed. Moreover, an efficient method for rapid in-vivo assessment of the Reynolds stress tensor is proposed.

Outline

Chapter 2 provides a general introduction of phase-contrast MRI (PC-MRI), 4D Flow MRI and the generalization of PC-MRI to turbulent flow.

Chapter 3 introduces concepts for accelerated MRI including different approaches to exploit data redundancies, comprising partial Fourier [37], parallel imaging [38], compressed sensing [32], and different approaches based on deep neural networks [39].

In Chapter 4 the concept of partial Fourier imaging [30], [31] for the assessment of turbulent flow is investigated. The inadequacy of the underlying assumption of limited spatial phase variations when imaging turbulent flow is proven.

Chapter 5 introduces 5D Flow MRI which extends 4D Flow MRI with a respiratory motion dimension in order to exploit correlations along cardiac and respiratory signal dimensions to enable rapid flow assessment within fixed scan times.

Chapter 6 introduces a concept for comprehensive in vivo assessment of turbulent flow in the aorta by extending 5D Flow MRI with velocity encoding along 6 non-collinear directions. Results of flow downstream of healthy and bio-prosthetic heart valves are demonstrated.

Chapter 7 addresses the long reconstruction times required by iterative reconstruction methods. A variational neural network is proposed with which adaptive filter kernels and activation functions are learned based on retrospectively undersampled volunteer data enabling rapid image reconstruction of undersampled data.

0 summarizes the findings of this thesis and an outlook of future steps is provided.

1.1 Contribution of the thesis

Accelerated imaging methods are indispensable to help translate turbulent flow assessment using MRI to a wider clinical community. In this work, different accelerated imaging methods are investigated and developed to enable time-efficient assessment of turbulent flow.

Model assumptions in partial Fourier (PF) imaging, which is based on Hermitian symmetry, are shown to be inadequate for turbulent flow imaging. While PF has been used in 4D Flow MRI in the past, our study shows that PF does not yield a benefit over symmetric bandwidth limitation in k-space.

To address inefficiencies due to respiratory gating, advances in respiratory motion resolved imaging are adopted to flow imaging. Accordingly, a method is provided which exploits redundancies between respiratory motion states to enable flow assessment in reduced scan times and independent of respiratory motion. Using a combination of Cartesian Golden angle undersampling, data-driven motion detection and locally low-rank image reconstruction, assessment of mean and turbulent flow velocities is demonstrated for a scan time of 4 minutes.

Highly accelerated flow imaging enables the incorporation of additional readouts into the sequence. As part of the present thesis, encoding of the Reynolds stress tensor is investigated and sequence modifications are proposed to enable robust in vivo assessment of the Reynolds stress tensor using 5D Flow MRI. The study provides the first demonstration of the in vivo assessment of the Reynolds stress tensor and demonstrates the ability of the method to quantify turbulent flow downstream of bio-prosthetic aortic valves.

Finally, image reconstruction based on deep neural networks to enable short reconstruction times is proposed. The method allows for the reconstruction of 4D MRI data in less than a minute. Moreover, the proposed architecture is demonstrated to generalize well permitting reconstruction of pathological flow patterns and of prospectively undersampled data based on training with a limited number of retrospectively undersampled datasets of healthy subjects.

2.1 Phase Contrast Encoding of Laminar Flow

Phase Contrast MRI (PC-MRI) relies on the fact that motion in the presence of a magnetic field gradient produces a change in phase of transverse magnetization. By playing out two acquisitions with different bipolar velocity encoding gradients, flow-dependent phase changes can be detected [1].

The Larmor frequency ω_L at location \mathbf{r} in a gradient field $\mathbf{G}(t)$ is given as

$$\omega_L(\mathbf{r}, t) = \gamma B_0 + \gamma \mathbf{G}(t)^T \mathbf{r}(t). \quad (2.1)$$

Assuming an excitation pulse at t_0 , the phase of precessing magnetization at location \mathbf{r} and time t_e is given by

$$\phi(\mathbf{r}, t_e) = \int_{t_0}^{t_e} \gamma B_0 dt + \int_{t_0}^{t_e} \gamma \mathbf{G}(t)^T \mathbf{r}(t) dt. \quad (2.2)$$

The phase term which depends on B_0 can be neglected, as the signal is demodulated with ω_0 on detection. Expanding the trajectory $\mathbf{r}(t)$ of magnetization using a Taylor series with an expansion point at the center t_m of the bipolar gradient waveform, the phase of magnetization at location $\mathbf{r}_m = \mathbf{r}(t_m)$ can be approximated as

$$\begin{aligned} \phi(\mathbf{r}_m, t) &= \int_{t_m - \frac{T}{2}}^{t_m + \frac{T}{2}} \gamma \mathbf{G}(t)^T \sum_{n=0}^{\infty} \frac{\mathbf{r}(t)^{(n)}}{n!} (t - t_m)^n dt \\ &= \int_{t_m - \frac{T}{2}}^{t_m + \frac{T}{2}} \gamma \mathbf{G}(t)^T [\mathbf{r}_m + \mathbf{v}_m (t - t_m) + \dots] dt \\ &= \gamma [\mathbf{M}_0^T \mathbf{r}_m + \mathbf{M}_1^T \mathbf{v}_m + \dots] \end{aligned} \quad (2.3)$$

where T is the total duration of the bipolar gradient, $\mathbf{M}_n = \int_{t_m - \frac{T}{2}}^{t_m + \frac{T}{2}} \mathbf{G}(t) (t - t_m)^n dt$ is referred to as n -th gradient moment and $\mathbf{r}_m, \mathbf{v}_m$ denote mean position and mean velocity. The net phase shift due to mean acceleration is zero, as an expansion point at t_m is selected [40]. Higher order terms of the Taylor expansion beyond acceleration are typically considered negligible [41].

Summarizing error terms due to field inhomogeneities, eddy currents, etc. as Θ , the measured signal becomes

$$s(\mathbf{r}_m) = s_0(\mathbf{r}_m)e^{i(\gamma\mathbf{M}_1^T \mathbf{v}_m(\mathbf{r}_m)+\theta)} \quad (2.4)$$

where $s_0(\mathbf{r}_m)$ depends on sequence and tissue parameters and is independent of the velocity encoding.

In order to eliminate the undesired phase component θ , a second measurement needs to be performed. Typically, an inverted velocity encoding gradient or a velocity compensated reference is used. Taking the phase difference of these two scans provides us with a phase which is proportional to the average velocity in the excited voxel volume at \mathbf{r}_m .

As the complex exponential is periodic, the maximum velocity which can be encoded by a sequence is determined by the first gradient moment of the sequence and is denoted as

$$VENC = \frac{\pi}{\gamma\|\Delta\mathbf{M}_1\|} \quad (2.5)$$

where $\Delta\mathbf{M}_1$ denotes the difference in first gradient moments per gradient axis between the two measurements.

The encoding can also be denoted by the encoding velocity frequency

$$\mathbf{k}_v = \gamma\Delta\mathbf{M}_1. \quad (2.6)$$

Consequently, the signal equation using \mathbf{k}_v reads

$$s(\mathbf{r}_m) = s_0(\mathbf{r}_m)e^{i(\mathbf{k}_v^T \mathbf{v}_m(\mathbf{r}_m)+\theta)}. \quad (2.7)$$

2.1.1 Velocity Encoding and Velocity-to-Noise-Ratio

The velocity-to-noise ratio (VNR) is related to the signal-to-noise ratio of the image magnitude and is inversely proportional to $VENC$ [41]

$$VNR \propto SNR_{mag} \frac{V}{VENC}. \quad (2.8)$$

This suggests that an ideal $VENC$ would be as low as possible. However, an accumulated phase which exceeds π leads to aliasing, i.e. the signal phase is interpreted as a lower velocity, corresponding to a phase within the interval $(-\pi, \pi)$. Therefore, setting the right $VENC$ is always a trade-off between avoiding aliasing and reaching the optimal SNR. To a certain degree, phase unwrapping algorithms can reduce phase-aliasing in the aliased image, but in general $VENC$ is set sufficiently high to avoid phase wraps. Multi-VENC approaches [42] can also be used to derive flow fields with the value range of a high $VENC$ acquisition and the VNR of a low $VENC$ acquisition at the cost of an increase in scan time.

2.1.2 Cine Phase Contrast MRI

The combination of flow-dependent phase contrast imaging with temporally resolved images throughout the cardiac cycle is referred to as cine PC-MRI [41]. For a given slice placed within the vessel of interest, the sequence provides temporally resolved quantitative information about the velocity-components within the slice. In clinical practice, cine PC-MRI is typically used to assess through-plane velocities [43]. However, correct positioning of the measurement plane is crucial. When the slice is not orthogonal to the flow of interest, peak velocities are underestimated. By encoding velocities in all three spatial dimensions, this underestimation can be addressed [44].

2.1.3 4D Flow MRI

4D Flow MRI refers to time-resolved volumetric imaging with three-directional velocity encoding. The three different velocity components can be measured by performing three consecutive scans, encoding velocities in three non-collinear directions.

Velocity encodings for 4D Flow MRI are typically denoted in matrix form. The forward model is

$$\boldsymbol{\phi} = \frac{\pi}{VENC} \mathbf{H} \mathbf{v} = \begin{pmatrix} \mathbf{k}_{v1}^T \\ \dots \\ \mathbf{k}_{vn}^T \end{pmatrix} \mathbf{v} \quad (2.9)$$

where \mathbf{H} describes the combination of gradient moments along the Cartesian directions encoded with VENC while the vector $\boldsymbol{\phi}$ contains the measured phases.

In the 4-point referenced encoding method [45] the velocity components in the three Cartesian directions are encoded independently using three velocity-encoded scans and one non-encoded reference scan:

$$\mathbf{H}_{4P,ref} = \begin{pmatrix} 0 & 0 & 0 \\ 1 & 0 & 0 \\ 0 & 1 & 0 \\ 0 & 0 & 1 \end{pmatrix} \quad (2.10)$$

The Hadamard encoding scheme employs simultaneous encodings in all directions for each measurement:

$$\mathbf{H}_{Hadamard} = \frac{1}{2} \begin{pmatrix} -1 & -1 & -1 \\ -1 & +1 & +1 \\ +1 & -1 & +1 \\ +1 & +1 & -1 \end{pmatrix}. \quad (2.11)$$

Hadamard encoding provides better noise statistics than 4-point referenced encoding, as the noise-level is direction independent [45]. However, the method lacks a non-encoded reference scan. Therefore, it cannot be used for encoding intravoxel standard deviations of turbulent velocities. A 5-point encoding [46] has been suggested to combine advantages of 4-point referenced and Hadamard

encoding. Moreover, redundant encoding schemes [47] using a higher number of velocity encodings which are not orthogonal and thus share some information have been proposed. These methods have been shown to yield a higher increase in VNR than multi-VENC approaches with the same number of velocity encodings [47].

2.1.4 Segmented k-Space Acquisition

The amount of k-space data required for 4D Flow MRI and most standard cine PC-MRI exams is too large to be acquired in a single heartbeat (although some advanced imaging techniques allow for real-time cine PC-MRI [48], [49]). Therefore, segmented k-space acquisition is performed. In each cardiac cycle, a subset of the required phase encodes is acquired for each time frame and the final image is reconstructed from data collected over several cardiac cycles [1].

2.1.5 Respiratory Navigation

Clinically feasible breathhold durations of 10-20 seconds make 4D Flow MRI acquisition impossible during breathhold. While it was suggested that respiratory motion might be ignored in order to speed up 4D Flow acquisitions [50], this can deteriorate spatial information [51] and, hence, respiratory motion suppression is generally recommended for 4D Flow exams [52]. To this end, respiratory motion may be recorded using navigators, a respiratory bellow [53], or self-gating approaches [54]. Samples which were acquired while the respiratory motion signal was not in the desired range of motion are discarded and need to be re-acquired. Accordingly, the net scan time becomes dependent on the breathing pattern of the subject.

In recent years, alternative approaches have been suggested to acquire data throughout the respiratory cycle while exploiting data correlations among different parts of the respiratory cycle during reconstruction [36], [55], [56].

2.2 Turbulent Flow

Turbulent flow is characterized by random spatial and temporal velocity fluctuations. Turbulent flow was found to occur in valvular pathologies but also in healthy subjects [17].

The random nature of turbulent flow makes it impossible to describe motion of magnetization analytically. A statistical description of turbulent flow is provided by the Reynolds decomposition [57] which represents net velocities as a sum of mean and fluctuating components:

$$\boldsymbol{v} = \bar{\boldsymbol{v}} + \boldsymbol{v}'. \quad (2.12)$$

v' denotes the velocity fluctuations around the time-averaged baseline provided by \bar{v} and can be described by statistical means, i.e. the standard deviation over time and/or space. An example of 1-dimensional turbulent flow and its representation in terms of \bar{v} and v' is provided in Figure 2.1.

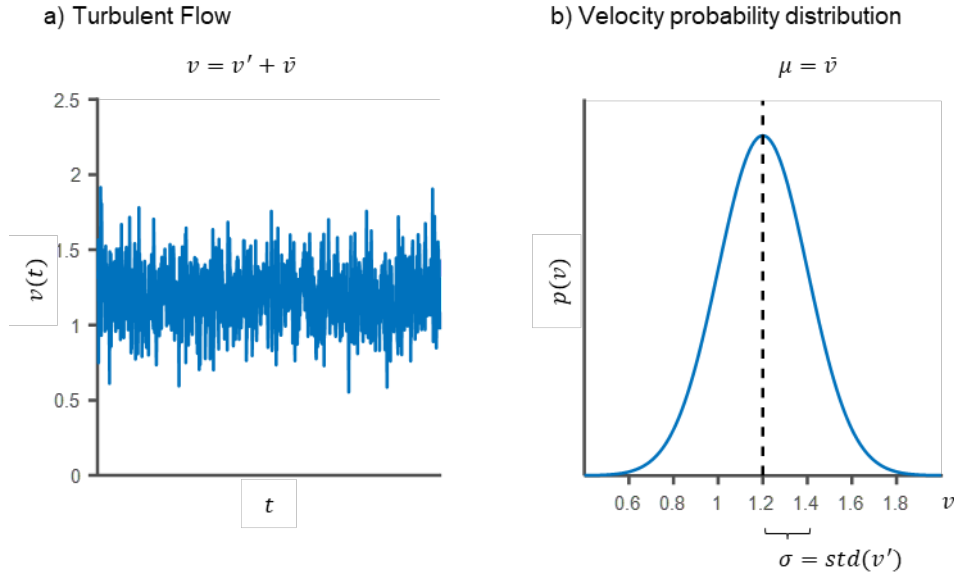


Figure 2.1: Illustration of the Reynolds decomposition of turbulent flow in one dimension. Turbulent flow is characterized by random spatial and temporal velocity fluctuations. Assuming a Gaussian velocity distribution, this flow can be fully characterized by its mean $\mu = \bar{v}$ and its standard deviation $\sigma = v'$.

2.2.1 Generalized Phase Contrast Magnetic Resonance Imaging

In conventional 4D Flow MRI spatiotemporally averaged velocities are derived from the signal phase while turbulent velocity fluctuations cannot be detected. However, the occurrence of different velocities within a voxel leads to phase dispersion and a measurable attenuation in the MR signal. This can be exploited to derive intra-voxel standard deviations of velocities σ from a PC-MRI acquisition [20].

In the one-dimensional case with $k_v = \|\mathbf{k}_v\|$ and scalar mean-velocities and given a Gaussian intra-voxel velocity distribution $p(v)$ with standard deviation σ and mean velocity \bar{v} in the direction indicated by \mathbf{k}_v

$$p(v) = \frac{1}{\sigma\sqrt{2\pi}} e^{-\frac{1}{2\sigma^2}v^2} \quad (2.13)$$

the signal can be determined as [20]

$$s(\sigma, \mathbf{k}_v) = s_0 \int_{-\infty}^{\infty} p(v) e^{-i\|\mathbf{k}_v\|v} dv = s_0 e^{-\frac{\sigma^2\|\mathbf{k}_v\|^2}{2}} e^{i\|\mathbf{k}_v\|\bar{v}}. \quad (2.14)$$

Thus, turbulence results in a reduction of the signal magnitude which depends on the intra-voxel standard deviation σ and the encoding strength $\|\mathbf{k}_v\|$. The effect on the relative signal magnitude for different gradient moment strengths and different values of σ is illustrated in Figure 2.2.

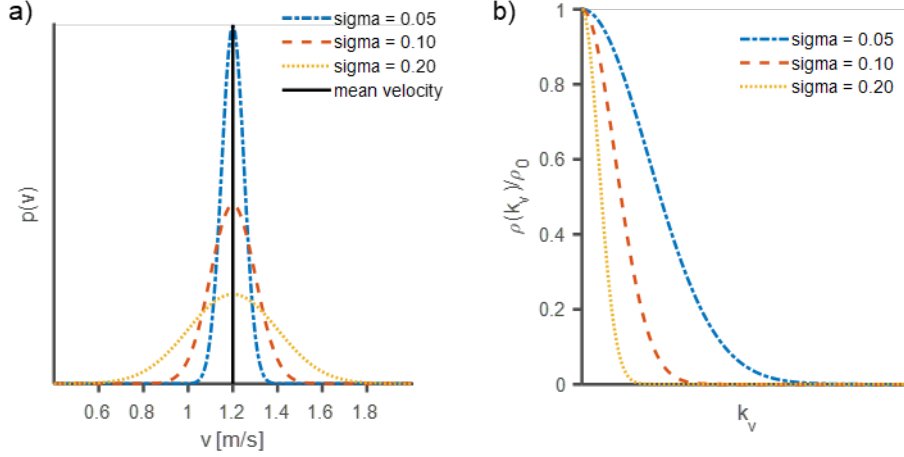


Figure 2.2: Impact of intravoxel velocity distribution on the relative signal magnitude measured with PC-MRI. a) illustrates velocity distributions within a voxel with different turbulence intensities, i.e. different intra-voxel standard deviations of velocities. b) shows the resulting reduction in signal magnitude which depends on the encoding strength k_v .

With the given signal model, the standard deviation σ of fluctuations in the encoded direction can be determined by dividing the magnitudes of a signal acquired without velocity encoding $s(\|\mathbf{k}_v\| = 0)$ and of a velocity-encoded acquisition $s(\|\mathbf{k}_v\| > 0)$.

$$\sigma = \sqrt{\frac{2 \ln \left| \frac{s(\|\mathbf{k}_v\| = 0)}{s(\|\mathbf{k}_v\| > 0)} \right|}{\|\mathbf{k}_v\|^2}} \quad (2.15)$$

The relationship between intravoxel standard deviations and the relative signal magnitude is non-linear. Hence, turbulent velocities are only accurately determined for a limited dynamic range, determined by the first gradient moment of the velocity encoding gradients. To assess turbulence with an improved dynamic range, a multi-point approach [58] has been suggested to probe the flow field at different values of $VENC$ and combine the information of the different measurements.

2.2.2 Turbulent Kinetic Energy

By playing out velocity encoding gradients in three orthogonal directions, turbulent kinetic energy (TKE) can be determined [20]

$$TKE = \frac{\rho}{2} (\sigma_x^2 + \sigma_y^2 + \sigma_z^2) \quad (2.16)$$

indicating how much energy is stored in velocity fluctuations.

2.2.3 Reynolds Stress Tensor

In 3D velocity fields, a statistical description of fluctuations includes variances and covariances as represented by the Reynolds stress tensor (RST) [57]

$$R = \rho \begin{bmatrix} \overline{v'_x v'_x} & \overline{v'_x v'_y} & \overline{v'_x v'_z} \\ \overline{v'_x v'_y} & \overline{v'_y v'_y} & \overline{v'_y v'_z} \\ \overline{v'_x v'_z} & \overline{v'_y v'_z} & \overline{v'_z v'_z} \end{bmatrix} \quad (2.17)$$

with standard deviations $\overline{v'_i v'_i}$, covariances $\overline{v'_i v'_j}$ and fluid density ρ .

Accordingly, the signal equation reads

$$|s(\mathbf{k}_v)| = |s_0| e^{-\frac{1}{2\rho} \mathbf{k}_v^T \mathbf{R} \mathbf{k}_v} e^{i \mathbf{k}_v^T \bar{\mathbf{v}}}. \quad (2.18)$$

Similar to encoding principles in diffusion tensor imaging [59], the components of the RST can be assessed by playing out velocity encodings along at least six non-collinear directions [28]. This approach will be assessed in detail in Chapter 6.

Chapter 3 Accelerated Phase Contrast MRI

The high dimensionality and large amount of data in 4D Flow MRI leads to long acquisition and reconstruction times, but also yields data redundancies which can be exploited by advanced image reconstruction methods to reconstruct images from highly undersampled acquisitions.

Data in flow MRI correspond to a high-dimensional tensor

$$\mathcal{S} \in \mathbb{C}^{N_x \times N_y \times N_z \times N_{coil} \times N_{cph} \times N_{kv} \times N_{rs}} \quad (3.1)$$

where N_x, N_y, N_z denote the spatial dimensions, N_{kv} represents the velocity encodings, N_{coil} the number of receiver elements of the coil, and N_{cph} and N_{rs} represent the cardiac phases and respiratory states, respectively. Reconstruction approaches typically use a vector or matrix representation of the data. Often, redundancies are exploited among a subset of these dimensions only. In the following, when a dimension is not mentioned explicitly, the reconstruction is performed separately for each element along that particular dimension. For example, when an image $\mathbf{s} \in \mathbb{C}^{N_x N_y N_z}$ is considered, the same operation is repeated $N_{cph} N_{kv} N_{rs}$ times, i.e. for each cardiac phase, velocity encoding and respiratory state.

The present chapter provides an overview of different acceleration methods based on exploiting data redundancies. A brief summary of the different approaches is provided in Table 1. While the focus of this work is on Cartesian sampling strategies, many of the mentioned methods can be also combined with non-Cartesian sequences.

3.1 Partial Fourier

Partial Fourier (PF) [60] is one of the earliest concepts to reduce scan time by exploiting redundancies inherent in the signal by using a constrained reconstruction. Real-valued objects show Hermitian symmetry in the Fourier domain. While in practice MR images are not real-valued, the method uses a phase estimate to correct for the image phase prior to enforcing Hermitian symmetry. Given a signal $s(x)$ and a phase estimate $\phi_{est}(x)$, this reads

$$\mathcal{F}\{s(x)e^{-i\phi_{est}(x)}\}(k) = [\mathcal{F}\{s(x)e^{-i\phi_{est}(x)}\}(-k)]^* \quad (3.2)$$

where \mathcal{F} is the Fourier Transform.

Accordingly, knowing the k-space signal in locations $k \in [0, k_{max}]$ allows to calculate the values for $k \in [-k_{max}, 0)$. To obtain an estimate of the image phase, a center fraction of k-space is typically sampled symmetrically, reducing the actual reduction factor to ca. 1/0.625 to 1/0.75.

Table 1: Overview of different approaches for accelerated imaging.

| | ASSUMPTION | SAMPLING STRATEGY |
|-------------------------------|---|--|
| PARTIAL FOURIER | Exploits Hermitian symmetry of real valued objects, assuming that the image phase can be corrected for using a low-resolution estimate. | One half of k-space is fully sampled. For the other half, only a small number of samples is acquired to obtain a low-resolution phase estimate. |
| PARALLEL IMAGING | Coil array elements receive the signal with different spatial sensitivities. This leads to an overdetermined forward model which allows reconstruction from an undersampled acquisition. | Typically, regular undersampling is used (e.g. every other k-space line), but the method can be used with arbitrary k-space trajectories [61]. Using autocalibration methods a fully sampled centre region in k-space is acquired to determine the relationship between different coil receiver channels. Alternatively, a separate calibration scan can be performed. |
| K-T BLAST/ K-T PCA | Spatial and temporal variations in dynamic MRI can be separated up to a certain order, i.e. the dynamic image series does not have full rank when written in a Casorati matrix. | The centre of K-space is fully sampled whereas the periphery is sampled on a sheared grid which leads to regular aliasing in the spatiotemporal domain. |
| COMPRESSED SENSING | The signal is compressible in some transform domain, i.e. it can be represented with few coefficients. Prior knowledge about this compressibility allows to reconstruct signals from incomplete measurements. | Sampling is designed to produce sampling incoherency, i.e. undersampling artifacts which spread uniformly over the object. Methods include variable density pseudorandom undersampling [32] or Golden angle sampling [62], [63]. |

Of note, Hermitian symmetry can only be exploited for undersampling in one dimension. When only data in the quadrant with $k_x > 0$ and $k_y > 0$ are available, missing k-space locations cannot be repopulated for the quadrants with $k_x < 0$ and $k_y > 0$ and $k_x > 0$ and $k_y < 0$, as $\mathcal{F}\{s(x, y)\}(k_x, k_y) = [\mathcal{F}\{s(x, y)\}(-k_x, -k_y)]^*$.

PF is listed as an option to reduce scan durations in 4D Flow MRI [52]. However, it has been shown that approaches based on approximating Hermitian symmetry perform worse than simply zero-filling the missing k-space locations in case objects exhibit accentuated spatial phase fluctuations [60], [64]. The suitability of PF for imaging of turbulent flow is investigated in detail in Chapter 4.

3.2 Parallel Imaging

Parallel imaging (PI) exploits differences in spatial sensitivities of coil elements in a multi-coil receiver array to repopulate missing k-space locations [38].

In a multi coil receiver array, each coil array element receives the same MR signal, but with a different spatial weighting. An image $\mathbf{s} \in \mathbb{C}^{N_x N_y N_z}$ is thus encoded as

$$\mathbf{S}_{coil} = \mathbf{C} \circ \mathbf{s} \quad (3.3)$$

where $\mathbf{C} = (\mathbf{C}_{coil_1} \ \dots \ \mathbf{C}_{coil_n})^T \in \mathbb{C}^{N_x N_y N_z \times N_{coil}}$ and $\mathbf{S}_{coil} = (\mathbf{S}_{coil_1} \ \dots \ \mathbf{S}_{coil_n})^T \in \mathbb{C}^{N_x N_y N_z \times N_{coil}}$ correspond to the spatial sensitivities and spatial signals received by the different coil array elements and \circ denotes the element-wise multiplication.

This makes the forward model an overdetermined linear system which can be used for SNR enhancement [65] or to recover images from an undersampled acquisition [38].

For regular Cartesian undersampling patterns, the original image can be recovered using the pseudo-inverse [38]. A more general solution for arbitrary k-space sampling can be formulated as an optimization problem which can be solved by iterative optimization methods [61]. This also allows for the incorporation of regularization terms $R(\mathbf{i})$.

$$\hat{\mathbf{s}} = \underset{\mathbf{s}}{\operatorname{argmin}} \|\Omega \mathcal{F} \mathbf{C}(\mathbf{s}) - \mathbf{d}\|_2^2 + \lambda R(\mathbf{s}) \quad (3.4)$$

Ω denotes the k-space sampling pattern, \mathcal{F} is the Fourier transform, \mathbf{C} denotes the coil sensitivity mapping from the image to the sensitivity weighted images seen by the coil elements and $\mathbf{d} \in \mathbb{C}^{N_x N_y N_z N_{coil}}$ corresponds to the acquired k-space data. λ is a weighting factor between consistency with the acquired data and regularization $R(\mathbf{s})$, which typically favors a minimum norm solution [66] or sparsity in some transform domain [32].

Different approaches exist to establish the relative spatial sensitivities of the different coil elements. SENSE [38] models the physical process behind a multi-coil acquisition and resolves aliasing by explicit knowledge of the spatial sensitivities of the coil elements. A low-resolution full field-of-view scan is performed using the coil array as well as the body coil. The relative coil sensitivity of the i -th coil element in a given location $c_i(\mathbf{r})$ can then be calculated as [38]

$$c_i(\mathbf{r}) = s_i(\mathbf{r})/s_{BC}(\mathbf{r}) \quad (3.5)$$

with $s_i(\mathbf{r})$ and $s_{BC}(\mathbf{r})$ denoting the signal measured in the given location by the coil element and the body coil respectively. If no measurement with the body coil was performed, one can also divide by the sum of squares of the signal received in the different coil channels, i.e.

$$c_i(\mathbf{r}) = s_i(\mathbf{r}) / \sqrt{\sum_{j=1, \dots, N_C} s_j(\mathbf{r})^2}. \quad (3.6)$$

A drawback of the latter approach, however, is that the image intensity will be weighted according to the spatial sensitivities of the coil array, i.e. intensities will be increased in locations close to the receiver coil relative to more remote locations. For example, in the case of 4D Flow MRI the chest wall can be very bright whereas the signal in the descending aorta will be rather low.

Another class of parallel imaging algorithms exploits the fact that coil sensitivities are spatially smooth and therefore have a narrow-band representation in k-space. Multiplication with smooth coil sensitivities in image-space can be written as a convolution with relatively small filter kernels in k-space. GRAPPA [67] and SPIRiT [68] explicitly determine such filter kernels by fitting a fully sampled region in k-space. GRAPPA then synthesizes missing k-space samples using the previously learned interpolation kernels whereas SPIRiT uses an iterative reconstruction to find a trade-off between closeness to the measured data and consistency with the learned filter weights.

ESPIRiT [69] builds on the same idea as SPIRiT but provides explicit coil maps which can be used with the same iterative reconstruction formalism as SENSE, i.e. using equation (3.3). A so-called autocalibration matrix is established from the fully sampled k-space center. Explicit coil maps are then determined from the null space of the autocalibration matrix, assuming that this null-space is valid globally in the acquired k-space dataset. Of note, images reconstructed with ESPIRiT show spatial intensity weighting similar to SENSE maps which were determined without the body coil.

While parallel imaging has been widely used for accelerated imaging, noise amplification remains a limiting factor for high acceleration factors [70].

3.3 k-t BLAST and k-t PCA

It was shown empirically, that spatial and temporal variations in dynamic MRI can be separated up to a certain order [71], [72]. As the images are correlated over time, a limited set of basis functions along time can be considered sufficient to represent all the temporal variation of the signal. Thus, elements of a signal $\mathbf{S} \in \mathbb{C}^{N_x \times N_{dyn}}$ with spatial dimension x and dynamics dyn can be written as a function of independent basis functions along space $u_x(x)$ and dynamics $v_{l_{dyn}}(dyn)$

$$s(x, dyn) = \sum_{l_x}^{L_x} \sum_{l_{dyn}}^{L_{dyn}} b_{l_x, l_{dyn}} u_{l_x}(x) v_{l_{dyn}}(dyn) \quad (3.7)$$

where $b_{l_x, l_{dyn}}$ is the weight of a combination of two basis functions indicated by the subscript indices. Assuming so-called partial separability for a signal, $L_x < N_x$ and $L_{dyn} < N_{dyn}$ holds.

In matrix-form, equation (3.7) can be formulated as

$$\mathbf{S}_{casorati} = \mathbf{U}^T \mathbf{B} \mathbf{V} \quad (3.8)$$

with the data rearranged in a so-called Casorati matrix as $\mathbf{S}_{casorati} \in \mathbb{C}^{N_x N_y N_z \times N_{dyn}}$, matrices \mathbf{U} and \mathbf{V} of rank L_x and L_{dyn} respectively and the elements of \mathbf{B} corresponding to $b_{l_x, l_{cpk}}$ in equation (3.7).

In k-t BLAST (Broad-use Linear Acquisition Speed-up Technique) [72] temporal basis functions are derived from a training scan with low spatial and high temporal resolution. An undersampled high resolution scan is acquired with sampling locations corresponding to a sheared grid in k-t space. This leads to foldover artifacts in the spatiotemporal domain which can be resolved by enforcing a signal representation which is based on the previously learned basis functions along time. k-t PCA [73] is based on the same assumption as k-t BLAST but uses principal component analysis (PCA) to reduce the number of temporal basis functions.

Of note, an assumption of partial separability can also be extended to the respiratory motion dimension [55].

3.4 Compressed Sensing

It is an empirical finding in signal processing that many types of signals can be well represented by a sparse vector in an appropriate basis or frame [74]. In compressed sensing (CS), this sparsity is exploited in order to reconstruct compressible signals from incomplete measurements.

A signal is called sparse if it has few non-zero coefficients. In mathematical terms, sparsity is expressed with the L_0 -norm, i.e. the number of non-zero coefficients.

$$\|\mathbf{s}\|_0 := \#\{i: s_i \neq 0\} \quad (3.9)$$

Given prior knowledge about signal sparsity in a transform domain, reconstruction of an image \mathbf{s} can be defined as an optimization problem which defines a trade-off between consistency with the measured data \mathbf{d} and sparsity in the sparse transform domain, which is defined by a mapping Ψ .

$$\hat{\mathbf{s}} = \underset{\mathbf{s}}{\operatorname{argmin}} \|\Omega\mathcal{F}\mathcal{C}(\mathbf{s}) - \mathbf{d}\|_2^2 + \lambda \|\Psi\mathbf{s}\|_0 \quad (3.10)$$

Ω denotes the undersampling operator, \mathcal{C} denotes the coil sensitivity mapping and λ is a weighting factor between data fidelity and sparsity.

The L_0 -norm is non-convex and therefore difficult to minimize. It was shown [75], that in most cases the problem formulation can be relaxed to the minimization of the L_1 -norm with $\|\mathbf{s}\|_1 = \sum_{i,j} |s_{i,j}|$.

The minimization of the L_1 -norm is a convex problem with an analytical solution provided by the soft-shrinkage operator [76]. Thus, the reconstruction problem can be reformulated as

$$\hat{\mathbf{s}} = \underset{\mathbf{s}}{\operatorname{argmin}} \|\Omega\mathcal{F}\mathcal{C}(\mathbf{s}) - \mathbf{d}\|_2^2 + \lambda \|\Psi\mathbf{s}\|_1 \quad (3.11)$$

which can be solved by standard algorithms such as FISTA [77] or ADMM [78].

3.4.1 Undersampling Strategies

Besides sparsity, the second prerequisite to the applicability of CS is incoherent aliasing interference. Ideally, undersampling artifacts should spread uniformly over the image and resemble white noise. When applying an appropriate sparsifying transform, the signal energy will be concentrated to few coefficients while the aliasing noise will be distributed globally. Thus, aliasing can be discerned from the sparse signal components in the transform domain and removed by iteratively solving an optimization problem.

Undersampling artifacts in radial [79], [80] and spiral [81] acquisitions show a good degree of incoherence. In contrast, regular Cartesian undersampling leads to very localized aliasing artifacts which cannot be discerned from actual signal components in the transform domain. Thus, they are hard or even impossible to remove from the reconstructed signal. For undersampling on a Cartesian grid it was shown that sampling a purely random subset of the data can often lead to a high degree of incoherence [82], [83].

CS sampling patterns in Cartesian MRI typically use so-called pseudo-random variable density undersampling patterns where the k-space center is sampled more densely than the k-space periphery. This is related to empirical findings that most signal energy is concentrated close to the k-space origin and that coarse-scale image components tend to be less sparse than fine-scale components [32].

To the author’s knowledge, research has not yet provided a general concept for undersampling pattern design in MRI. Properties of non-linear reconstruction are dependent on the signal. A Bayesian approach which selects the sample that minimizes uncertainty given the already measured data and statistical information extracted from representative images has been proposed [84]. Moreover, linearization of the non-linear reconstruction was suggested to assess the impact of different k-space sampling patterns [85]. However, for both methods, to determine the optimal sampling pattern one would need to know the distribution of the class of signals to be acquired. Thus, the optimal sampling pattern according to both methods is application specific.

Spatiotemporal Incoherence and Golden Angle Sampling

Cardiovascular MRI typically exploits redundancies in the temporal dimension, as different cardiac frames are highly correlated. Therefore, sampling incoherence is also required along the temporal dimension. While one might simply pick different random undersampling patterns for each cardiac frame, sampling patterns can also be designed to maximize temporal incoherence [62], [86], [87].

A very high degree of incoherence between temporally adjacent samples can be obtained with the Golden angle acquisition scheme which was originally suggested for radial acquisition [62], but has also been adopted in Cartesian imaging by mapping randomized points from the spokes of a radial or spiral trajectory onto a Cartesian grid [63], [87].

3.4.2 Sparse Transform Domains for Flow Imaging

Common sparse transform domains in CS such as Wavelets and Total Variation (TV) have also been used for flow MRI [56], [63], [88]. Moreover, the temporal Fourier transform is effective in enforcing smooth or periodic temporal behavior in cardiac MRI [89]. However, the high dimensionality yields many further options to apply sparse transforms. In the following, a brief overview of other approaches more specific to flow imaging or cardiac imaging will be provided.

Regularization Based on Physical Knowledge

In several studies flow-specific regularization terms based on physical knowledge have been proposed. Blood is incompressible and the conservation of mass implies that everything, which flows into a location, has to flow out again. Mathematically this translates into a requirement of zero divergence, i.e.

$$\frac{\delta v_x}{\delta x} + \frac{\delta v_y}{\delta y} + \frac{\delta v_z}{\delta z} = 0. \quad (3.12)$$

Divergence of the flow field can be penalized directly [90], or the flow field can be represented in terms of a divergence-free Wavelet dictionary [90], [91]. In reality, however, blood flow measurements with

MRI are not entirely divergence-free due to the limited spatial resolution of MR scans and hence partial volume effects. In response, it has been suggested to decompose the field into divergence-free and a non-divergence free component which can be processed separately [91], [92].

Of note, regularization of velocity components in CS requires separate treatment of magnitude \mathbf{m} and phase $\phi = \frac{\pi}{VENC} \mathbf{H}\mathbf{v} + \theta$ with encoding velocity $VENC$, encoding matrix \mathbf{H} and background phase θ .

This leads to a non-linear non-convex optimization problem

$$\hat{\mathbf{m}}, \hat{\mathbf{v}} = \underset{\mathbf{m}, \mathbf{v}}{\operatorname{argmin}} \left\| \Omega \mathcal{F} \mathcal{C} \left(e^{i \left(\frac{\pi}{VENC} \mathbf{H}\mathbf{v} + \theta \right)} \right) - \mathbf{d} \right\|_2^2 + \lambda_1 \|\Psi_m \mathbf{m}\|_1 + \lambda_2 \left\| \Psi_v \frac{\pi}{VENC} \mathbf{H}\mathbf{v} \right\|_1 \quad (3.13)$$

with sparsifying operators Ψ_m and Ψ_v for magnitude and velocities, and regularization weights λ_1 and λ_2 , respectively. Iterative reconstruction is therefore typically performed by optimizing signal phase and signal magnitude in alternating steps [90], [93]. Moreover, an estimate of the background phase θ is required, e.g. by reconstructing the non-encoded reference image first with another reconstruction method.

Explicit and Implicit Low-Rank Representations

The concept of partial separability as introduced for k-t BLAST and k-t PCA in section 3.3 can also be used for CS reconstructions. Such a model can be enforced in the image reconstruction by either confining the reconstruction to an explicit set of basis function, or by implicitly enforcing a low-rank representation of the Casorati matrix. The first approach is used by methods such as k-t SPARSE [94], or MOCCO [95], while the latter approach can be achieved by regularizing the nuclear norm of the Casorati matrix in an iterative reconstruction [35]. This corresponds to a soft thresholding operation [96], i.e. enforcing sparsity of the singular value matrix.

When the signal comprises multiple dynamics, such as in flow imaging, different dynamics can be combined in the Casorati matrix, e.g. as $\mathcal{S}_{casorati} \in \mathbb{C}^{N_x N_y N_z \times N_{cph} N_{kv}}$ [34], [97].

Instead of enforcing the same low-rank representation for the entire image, improved reconstruction results have been obtained in several studies when enforcing low-rankedness locally by decomposing the images into smaller patches [33], [98], [99].

Of note, all the aforementioned low-rank models are based on sums of products of linear functions. When signal dynamics exhibit non-linear behavior, such as the velocity encodings in phase contrast MRI, the approximation error for a low-rank approximation can become very high.

Low-Rank Tensor Models

Low-rank tensor models have been suggested as an alternative to low-rank matrix representations. Different signal dynamics are represented by separate sets of basis functions [100], [101].

$$\begin{aligned}
& s(x, dyn_1, dyn_2, \dots) \\
& = \sum_{l_x}^{L_x} \sum_{l_{dyn_1}}^{L_{dyn_1}} \dots \sum_{l_{dyn_i}}^{L_{dyn_i}} b_{l_x, l_{dyn_1}, l_{dyn_2}, \dots} u_{l_x}(x) v_{dyn_1}(dyn_1) \dots v_{dyn_i}(dyn_i) \quad (3.14)
\end{aligned}$$

This representation corresponds to the so-called Tucker decomposition [102]. In contrast to performing a singular value decomposition on a Casorati matrix, the Tucker decomposition is non-unique. The method was suggested for 4D Flow reconstruction [103], but to the author's knowledge no comparison between low-rank tensor and low-rank Casorati matrix representations for MR image reconstruction has been performed to date.

Low-Rank + Sparse Decompositions

Low-rank representations can be very sensitive to outliers. To cope with this disadvantage, robust principal component analysis has been proposed [104], which represents the signal as a sum of a low-rank component and a sparse component. The model was adapted for MRI reconstructions in low-rank + sparse (L+S) reconstruction [35], [105] which models dynamic MRI as a superposition of a background which varies slowly over time and is thus highly correlated among different frames, and a dynamic component, which varies rapidly over time.

The method was also extended to 4D Flow MRI [34]. The reconstruction corresponds to solving the following minimization problem.

$$\{\widehat{\mathbf{S}}_L, \widehat{\mathbf{S}}_S\} = \underset{\mathbf{S}_L, \mathbf{S}_S}{\operatorname{argmin}} \|\Omega \mathcal{FC}(\mathbf{S}_L + \mathbf{S}_S) - \mathbf{d}\|_2^2 + \lambda_L \|\mathbf{S}_L\|_* + \lambda_S \|\Psi \mathbf{S}_S\|_1, \quad s.t. \mathbf{S} = \mathbf{S}_L + \mathbf{S}_S \quad (3.15)$$

where the image is reshaped as a Casorati matrix $\mathbf{S} \in \mathbb{C}^{N_x N_y N_z \times N_{cph} N_{kv}}$ and \mathbf{S}_L and \mathbf{S}_S denote the low-rank and sparse component respectively.

Dictionary Learning

Dictionary learning methods can be used to learn sparse representations [106]–[108] and have successfully been used to model cardiac dynamics [107], [109]. Atoms, i.e. the entries of the dictionary can be learned either from separate training data [109], or from the undersampled data itself [107].

Of note, low-rank approaches can also be considered a dictionary approach. However, they do not allow for redundant dictionaries. Moreover, the underlying factorization by linear basis functions might not be optimal when representing non-linear relationships in data.

3.5 Deep Learning

In the last few years, deep neural networks have gained increasing popularity in MR image reconstruction. The key idea is to make a neural network learn abstract features from retrospectively undersampled measurements during training. Thereafter, prospectively undersampled acquisitions can be reconstructed by inference. The reconstruction step can be performed very efficiently on graphical processing units (GPUs) enabling very short reconstruction times. Moreover, reconstruction results can be superior to traditional iterative approaches [110]–[112].

A deep neural network consists of an input layer, followed by several layers of so-called neurons, which take a weighted sum of inputs from the previous layer followed by a non-linear activation function [113]. Finally, an output layer maps the output of the previous layer to the target variable, i.e. the image. Fully connected deep neural networks (also known as a multilayer perceptron) connect the output of all neurons in the previous layer to the input of each neuron in the following layer. Therefore, for typical image sizes, fully connected neural networks lead to a very high number of weights. This implies a need for large amounts of training data and memory, and an increased risk of overfitting making their application in MR image reconstruction challenging.

In imaging applications, convolutional neural networks [113] (CNNs) are typically used. In CNNs each layer consists of convolution kernels followed by some non-linear operations. Typically, down- and upsampling between the layers is included to make the different convolutional layers act on different spatial scales. As the same convolution kernels are applied to each region in the image, the number of parameters to be trained is much smaller than for a fully connected neural network.

End-to-end Reconstruction

It has been suggested that the entire reconstruction pipeline from k-space to the final image can be learned [114]. However, this implies that the network has to implement the Fourier transform, which leads to a considerable increase in training parameters, while an efficient analytical solution for the Fourier transform exists. Most methods therefore start at a later point in the signal processing pipeline.

Image Enhancement Based Approaches

Deep learning approaches have been applied to produce images of diagnostic quality from aliased direct reconstruction of an undersampled k-space acquisition. To this end, the neural network architecture acts as a filter bank enhancing object features while reducing noise-like image structure to provide an image free from aliasing [115]–[117].

A justification for this approach relates to the insight, that the encoding operator in an iterative MR image reconstruction can be written as a convolution [115]. The reconstruction can hence be represented in a block diagram as a sequence of convolutions and point-wise non-linearity, and thus

corresponds to the operations performed in a CNN. However, the authors have reported a lack of transferability between datasets when trying to reconstruct from data acquired at different undersampling rates. Moreover, a recent study [118] has revealed that reconstruction methods purely based on filtering an aliased image do not generalize well to different undersampling rates and can actually perform worse when provided with data acquired at a higher sampling rate.

Incorporation of Data Consistency

Similar to the data-fidelity term in traditional iterative reconstruction methods, convolutional layers of a neural network can be combined with a data consistency step which enforces closeness of the image estimate to the measured data [110], [119]–[121].

Projection based enforcement of data consistency was suggested [119]. Here, k-space locations for which data have been acquired are filled up with a linear combination of the measured data and the current estimate. As an alternative, a gradient step for data consistency can be incorporated in the neural network [110], [122], as explained in more detail in the following section.

Replicating Iterative Methods by Loop Unrolling

The individual iterations of an iterative reconstruction can be represented as layers of a neural network [110], [123], often referred to as loop unrolling. Hammernik et al. [110] proposed to use this approach in combination with fields of experts regularization [124], which is a generalization of TV-regularization. The regularizer consists of convolution kernels and weighting with scalar functions, which makes its representation in a neural network particularly easy.

The iterative reconstruction is defined as the minimization of a cost function

$$\hat{\mathbf{s}} = \underset{\hat{\mathbf{s}}}{\operatorname{argmin}} \|\Omega\mathcal{F}\mathcal{C}(\mathbf{s}) - \mathbf{d}\|_2^2 + \lambda \sum_{i=1}^{N_f} \langle \Phi_i(\mathbf{D}_i\mathbf{s}), \mathbf{1} \rangle \quad (3.16)$$

with N_f filters which are each parameterized by a kernel $\mathbf{D} \in \mathbb{R}^{5 \times 5 \times 5}$ and a scalar potential function $\Phi \in \mathbb{R}$.

In a single iteration, the next estimated solution is

$$\mathbf{s}^{k+1} \leftarrow \mathbf{s}^{(k)} - \alpha^{(k)} \left[\mathcal{C}^T \mathcal{F}^T (\Omega\mathcal{F}\mathcal{C}(\mathbf{s}) - \mathbf{d}) - \lambda \sum_{i=1}^{N_f} \mathbf{D}_i^T \phi_i \operatorname{sign}(\mathbf{D}_i\mathbf{s}^{(k)}) \right] \quad (3.17)$$

with ϕ_i being the derivative of the potential function Φ_i and $\alpha^{(k)}$ denoting the step size.

This operation can be written as a layer of a CNN with filter kernels \mathbf{D} and activation functions Φ_i . Thus, the entire reconstruction is recast as a neural network where each layer corresponds to one iteration as specified above.

To enable reconstruction with a lower number of iterations (typically ca. 5-10), the regularization strength and regularization terms are allowed to vary for each iteration. Thus, each individual layer consists of a data fidelity step and regularization with filter kernels weighted by non-linear activation functions

$$\mathbf{s}^{k+1} \leftarrow \mathbf{s}^{(k)} - \left[\mathcal{C}^T \mathcal{F}^T (\Omega \mathcal{F} \mathcal{C} \mathbf{s} - \mathbf{d}) - \alpha^{(k)} \sum_{i=1}^{N_f} \mathbf{D}_{i,k}^T \phi_{i,k} \mathbf{D}_{i,k} \mathbf{s}^{(k)} \right]. \quad (3.18)$$

Of note, whereas other CNN approaches use predefined activation functions, e.g. sigmoid, tanh, etc., in this application the activation functions are learned during training. The set of trainable parameters therefore consists of step sizes, convolutional layers, and activation functions

$$\Theta = \{ \alpha^{(k)}, \mathbf{D}_{i,k}, \phi_{i,k} \}_{i,k}. \quad (3.19)$$

Generative Adversarial Neural Networks

Generative adversarial neural networks (GANs) [125] consist of two models which are trained simultaneously. The generative model aims to capture the data distribution whereas the discriminative model aims to distinguish between data produced by the generative model and data included in the training set.

In MRI reconstruction, an adversarial network was suggested to distinguish between fully sampled ground truth data and the de-aliased reconstruction [117]. During training, the discriminator is used as a loss function for training of the reconstruction network.

Moreover, GANs have been suggested as a prior for image reconstruction. In an iterative reconstruction, the image is confined to the range space of the generator network [126].

$$\hat{\mathbf{z}} = \underset{\mathbf{z}}{\operatorname{argmin}} \|\Omega \mathcal{F} \mathcal{C}(G(\mathbf{z})) - \mathbf{d}\|_2^2, \quad \text{s.t. } \|\mathbf{z}\| \leq \sqrt{d} \quad (3.20)$$

where G is the generative network, \mathbf{z} is the latent vector which yields the image $\mathbf{s} = G(\mathbf{z})$, and which is constrained to a hypersphere of radius \sqrt{d} .

Dealing with Limited Ground Truth Data

A particular problem in MR imaging and flow imaging in particular is the limited availability of training data. Inspired by transfer learning it has been suggested, that the initial training can be performed with non-MR image data, and then the network can be refined by training with the available MR data [127]. Moreover, smaller network architectures with a lower number of trainable parameters can be beneficial, as they tend to overfit less on the training data and generalize better.

A completely database-free approach was suggested with the RAKI [112] method, which replicates classical k-space interpolation approaches [67], [68]. In RAKI, a CNN is trained based on a fully sampled

autocalibration region and is then used to repopulate missing k-space samples. While this approach does not need a database of ground truth data, the CNN needs to be trained again for each newly acquired image.

Chapter 4 On the Limitations of Partial Fourier Acquisition in Phase-Contrast MRI of Turbulent Kinetic Energy

Published in: J. Walheim, A. Gotschy, and S. Kozerke, "On the limitations of partial Fourier acquisition in phase-contrast MRI of turbulent kinetic energy," *Magn. Reson. Med.*, vol. 81, no. 1, pp. 514–523, 2019.

4.1 Introduction

Partial Fourier (PF) [30], [31], [60] acquisition is a standard option on clinical MRI systems to reduce scan time.

While reconstruction of velocity maps from PF phase-contrast data is performed using zero-filling reconstruction on various MR systems, different options exist to reconstruct magnitude images which traditionally serve for anatomical referencing. With the developments of mapping the variance of velocity fluctuation based on magnitude images from different velocity encodes, accurate reconstruction of magnitude information has become important for the assessment of turbulent kinetic energy (TKE) [20], [128].

Assuming Hermitian symmetry in k-space, missing samples can be repopulated using various methods [31], [37], [60], [129]. To approximate the Hermitian symmetry requirement of PF reconstruction, a low-resolution phase estimate based on the central, symmetrically sampled portion of k-space is required to phase-correct the data prior to computing the conjugate signals.

It has been argued that the low-resolution phase estimate is sufficient to approximate Hermitian Symmetry in the reconstruction of magnitude images in phase-contrast MRI (PC-MRI) provided that moderate PF factors are used. Accordingly, PF has been applied in PC-MRI applications [130], [131],[54] and has been listed as an option for scan time reduction in a recent consensus statement on 4D flow MRI [52].

With the advent of k-t and compressed sensing based acceleration techniques [32], [72], combinations of undersampling with PF acquisition have been promoted [129], [132]–[134] to reduce the net undersampling factor in k-t and compressed sensing reconstructions. Such combinations have also been applied to phase-contrast flow measurements [58], [93].

Beyond reduction of the number of phase encodes for scan time reduction, Partial Echo (PE) sampling in frequency encode direction is frequently used to reduce intra-voxel phase dispersion in transient and turbulent flows. While original work proposed concatenating two PE measurements to form a full

echo at the expense of doubling scan time [135], single PE acquisition is frequently used in phase-contrast applications [26], [58], [136], [137].

In general, the phase estimate required for PF or PE reconstruction is of high importance for the performance of methods enforcing Hermitian symmetry and any inaccuracy significantly deteriorates the results [60], [64]. Previous studies have shown that in regions of rapid phase changes, methods which enforce Hermitian symmetry perform poorly and zero-filling reconstruction shows less artifacts [64].

The objective of the present work is to study PF techniques applied to phase-contrast MRI and to assess their limitations for assessing TKE, i.e. when reconstructing magnitude images from PC-MRI data acquired with PF sampling. To this end, PF data of simulated flow in a stenotic U-bend are reconstructed using homodyne reconstruction[37], projection onto convex sets [64] and zero-filling. Artifact levels in magnitude and TKE maps are compared relative to symmetrically sampled data of identical bandwidth as well as to the fully sampled reference.

4.2 Theory

Partial Fourier Reconstruction

PF reconstruction methods exploit the fact, that real-valued objects show Hermitian symmetry in the Fourier domain, i.e. $d(k) = [d(-k)]^*$. Accordingly, missing k-space samples may be repopulated from fractional k-space data by enforcing Hermitian symmetry. However, in most practical situations, objects are not real-valued and hence reconstruction requires a phase correction step. Given a phase estimate ϕ_{est} , the image phase can be corrected and Hermitian symmetry of the image $s(x)e^{-i\phi_{est}(x)}$ can be enforced:

$$\mathcal{F}\{s(x)e^{-i\phi_{est}(x)}\}(k) = [\mathcal{F}\{s(x)e^{-i\phi_{est}(x)}\}(-k)]^* \quad (4.1)$$

where \mathcal{F} is the Fourier Transform.

The phase estimate is typically obtained by symmetrically sampling the low k-space frequencies. For this reason, a typical PF acquisition acquires between 55% and 75% of k-space [138]. The ratio of acquired data to total k-space data is typically referred to as PF fraction [138].

Margosian and Homodyne reconstruction

In the Margosian method [139], the acquisition of a half-echo is modelled as a multiplication with a Heaviside function $\theta(k)$ in the spatial frequency domain. The corresponding impulse response function reads

$$H_{PF}(k) = \theta(k + (PF - 0.5)k_{max}) \xrightarrow{\mathcal{F}^{-1}} h_{PF}(x) = e^{i2\pi x * (PF - 0.5)k_{max}} 0.5 \left[\delta(x) + \frac{1}{\pi i x} \right] \quad (4.2)$$

and the image obtained from one half of k-space is written as

$$\begin{aligned} s_h(x) &= (s(x) * e^{i\phi}) \circledast \frac{1}{2} \left(\delta(x) + \frac{1}{\pi i x} \right) = \frac{1}{2} s(x) * e^{i\phi} + \left[\frac{1}{2} s(x) * e^{i\phi} \circledast \left(\frac{1}{\pi i x} \right) \right] \\ &= \frac{1}{2} s(x) * e^{i\phi} + e^{i\phi} * \left[\frac{1}{2} s(x) \circledast \left(\frac{1}{\pi i x} \right) \right] \end{aligned} \quad (4.3)$$

where $s(x)$ is the modulus of the image and ϕ the image phase. Given a phase estimate ϕ_{est} , the image can be obtained as

$$s(x) \approx 2\text{Re} \left\{ \frac{s(x)}{2} * e^{i(\phi - \phi_{est})} + \frac{i}{2} (s(x) * e^{i(\phi - \phi_{est})}) \circledast \left(\frac{1}{\pi x} \right) \right\} \quad (4.4)$$

since the second part of the equation is purely imaginary. However, to write $\left[\frac{1}{2} s(x) e^{i\phi} \circledast \left(\frac{1}{\pi i x} \right) \right] = e^{i\phi} * \left[\frac{1}{2} s(x) \circledast \left(\frac{1}{\pi i x} \right) \right]$, ϕ is required to be independent of x and hence spatially invariant.

Assuming slowly varying image phase, the term $s(x) e^{-i\phi_{est}(x)}$ is real-valued to first approximation. Thus, the image $s(x)$ can be written as a function of the acquired k-space lines $k \in [k_0; k_{max}]$ of the phase-corrected signal $\tilde{s}(k) = \mathcal{F}^{-1}\{s(x) e^{-i\phi_{est}(x)}\}$ [138]

$$\begin{aligned} s(x) &= \int_{-k_{max}}^{-k_0} \tilde{s}(k) e^{ikx} dk + \int_{-k_0}^{k_0} \tilde{s}(k) e^{ikx} dk + \int_{k_0}^{k_{max}} \tilde{s}(k) e^{ikx} dk \\ &= \int_{-k_0}^{k_0} \tilde{s}(k) e^{ikx} dk + 2\text{Re} \left[\int_{k_0}^{k_{max}} \tilde{s}(k) e^{ikx} dk \right] \end{aligned} \quad (4.5)$$

where Hermitian symmetry is exploited to obtain

$$\int_{-k_{max}}^{-k_0} \tilde{s}(k) e^{ikx} dk = \left[\int_{k_{max}}^{k_0} (\tilde{s}(k') e^{ikx'}) dk' \right]^* \quad (4.6)$$

This is the basis of the so-called Homodyne Reconstruction (HR)[37]. Since the phase-corrected signal $\tilde{s}(k)$ has to be real-valued, one considers the real part of Equation 4.5 to be the correct image and Homodyne Reconstruction reads

$$s_{HR} = \text{Re} \left[\int_{-k_0}^{k_0} \tilde{s}(k) e^{ikx} dk + 2 * \int_{k_0}^{k_{max}} \tilde{s}(k) e^{ikx} dk \right]. \quad (4.7)$$

Inconsistencies at the transition between synthesized and acquired data at k_0 lead to artifacts in the reconstructed image. To reduce these inconsistencies a linear ramp or a cosine tapered window [138] (also known as asymmetric Hanning window [140]) can be used. However smoothing the transition was shown to reduce SNR [37].

Iterative reconstruction

Alternatively, inconsistencies at k_0 can be reduced by enforcing Hermitian symmetry iteratively. The method of projections onto convex sets (POCS) [31] alternates between projections onto the set Ω_1 of images which agree with the estimated phase $\phi_{est}(x)$ and projections onto the set Ω_2 of data which match the acquired k-space data $d(k)$. Parallel POCS performs the projections simultaneously and provides better results, when the intersection between both constraints is empty [141].

$$\begin{aligned}\Omega_1 &= \{s(x) : \angle I(x) = \phi_{est}(x)\} \\ \Omega_2 &= \{s(x) : \mathcal{F}\{s(x)\}(k) = d(k); k \in [k_0; k_{max}]\} \\ s_{n+1} &= \mu * \mathcal{P}_{\Omega_1}(s_n) + (1 - \mu) * \mathcal{P}_{\Omega_2}(s_n), \mu \in (0,1)\end{aligned}\tag{4.8}$$

Zero-Filling Reconstruction

Methods based on Hermitian symmetry do not retain phase information and are therefore not suited for the reconstruction of phase images as in PC-MRI. Moreover, Hermitian symmetry allows to recover the full k-space only, if PF has been applied along a single k-space dimension, as $s(k_x, k_y, k_z) = [s(-k_x, -k_y, -k_z)]^*$. If PF is applied to more than one dimension or high resolution phase images are required, zero-filling (ZF) reconstruction remains the only option [138].

To assess the effect of ZF, the point spread function (PSF) of the sampling pattern can be inspected. The corresponding PSF becomes a sinc function with phase modulation depending on the PF fraction:

$$\begin{aligned}H(k) &= \Pi_{2k_{max}PF}(k - (1 - PF)k_{max}) \xrightarrow{\mathcal{F}^{-1}} \\ PSF(x) &= e^{i2\pi(1-PF)k_{max}x} * 2PF * k_{max} \frac{\sin(2\pi k_{max}PF * x)}{2\pi k_{max}PF * x}\end{aligned}\tag{4.9}$$

Figure 4.1a compares the magnitude and phase of the PSF for $PF = 0.75$ and a full k-space acquisition. It is readily seen that the full-width-at-half maximum (FWHM) of the PSF is increased with PF and a linear phase is introduced according to the Fourier shift theorem. Accordingly, PF acquisition is equivalent to symmetric sampling of k-space with a reduced bandwidth except for a linear phase ramp. As illustrated in Figure 4.1b, this leads to distortions, which are less smooth than the Gibbs ringing effect observed for symmetric sampling (SYM).

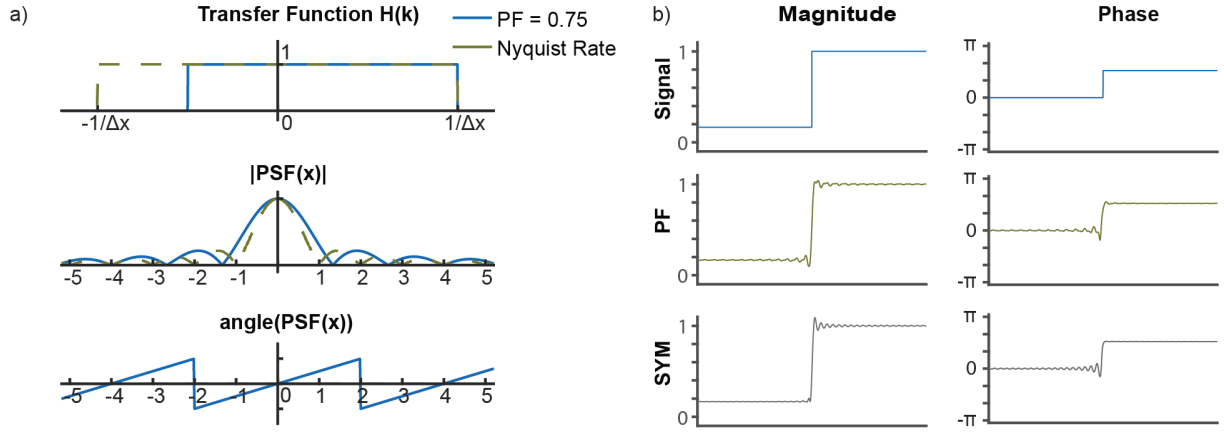


Figure 4.1: Effect of Partial Fourier (PF) sampling. a) Sampling a rectangular window in k -space corresponds to a convolution of the image with a sinc-shaped PSF function. By reducing the bandwidth in k -space, PF sampling increases the full-width-at-half maximum (FWHM) and hence reduces the spatial resolution which can be resolved by the system accordingly. In addition, the PSF is weighted with a linear phase shift according to the Fourier shift theorem. b) Example of PF sampling of a Heaviside function. Symmetric sampling of k -space (SYM) leads to Gibbs ringing artifacts. With PF, phase modulation of the PSF leads to more complex truncation artifacts

Combination with Compressed Sensing

In combination with compressed sensing (CS), PF acquisition can be modelled as a convolution of the PSF of the CS sampling pattern and the PSF of the PF acquisition as follows:

$$H(k) = H_{cs}(k) H_{pf}(k) \xrightarrow{\mathcal{F}^{-1}} PSF(x) = PSF_{cs}(x) * PSF_{PF}(x). \quad (4.10)$$

Accordingly, the net effect on the PSF of the sampling pattern can be assessed using design criteria such as the sidelobe-to-peak ratio [32].

4.3 Methods

Simulated Data

Three-dimensional 4-point phase-contrast data were simulated using Computational Fluid Dynamics (CFD) yielding data of mean and turbulent velocities of pulsatile flow in a stenotic U-bend phantom (large eddy simulation (LES) in OpenFOAM [142], pipe diameter of 25 mm, stenosis radius of 12.5 mm, kinematic viscosity $1.3 * 10^{-5} \frac{m^2}{s}$, max. flow rate 235 ml/s and Womersley number of appr. 3.5).

In order to accurately model the measurement of a continuous object and to model the discretization error accurately[143], the measurement of a continuous object was approximated by upsampling the dataset to ten times the original resolution. Thereafter the data was transformed to k -space and samples were drawn from the k -space center, leading to an acquisition matrix of 174x120. Besides

noise-free data, realistic SNR was simulated by adding normal distributed complex-valued noise to the high-resolution object to arrive at SNR values between 20 dB and 60 dB.

In-vivo Data

4D flow data was acquired in a patient with dilation of the ascending aorta and combined aortic stenosis and regurgitation due to a bicuspid aortic valve on a 3T Philips Ingenia system (Philips Healthcare, Best, the Netherlands) using a navigated Cartesian 4-point referenced [45] phase-contrast gradient-echo sequence with an encoding velocity (v_{enc}) of 150 cm/s, a spatial resolution of $2.5 \times 2.5 \times 2.5 \text{ mm}^3$, an acquisition matrix of $124 \times 112 \times 33$, bandwidth 0.88 kHz/pixel and echo time 2.50 ms. Data were acquired and reconstructed using SENSE [38] with a net acceleration factor of $R = 2$.

Concomitant field correction was applied to the signal phase according to [144] and eddy currents were corrected for with a linear model fitted to stationary tissue [145]. Written, informed consent was obtained before the experiment according to ethics approval and institutional guidelines.

Partial Fourier Reconstruction

PF acquisition of both CFD and in-vivo data was simulated by setting the lower 25% of phase-encodes in ky-direction to zero, corresponding to a PF factor of 0.75. Simulated PF data were subsequently reconstructed using HR, POCS and ZF. The phase correction required for HR and POCS was performed based on the phase estimate derived from the symmetrically sampled central k-space region. The corresponding reconstruction procedures are outlined in Figure 4.2. A unit step transition was selected for HR (see Supporting Information Figure 4.S2 for details). For parallel POCS, μ was set to 0.5 (see Equation 4.8). PF reconstructions of CFD data were compared to a 75% symmetrically undersampled k-space (SYM) as well as to the full acquisition matrix (FULL). The in-vivo data were retrospectively decimated to yield a PF fraction of 0.75, reconstructed with HR and POCS and compared to ZF and SYM.

Compressed Sensing Reconstruction

The combination of PF and CS was assessed by retrospectively undersampling the numerical dataset with a Poisson density weighed random undersampling pattern combined with PF = 0.75, yielding a net reduction factor of $R_{net} = 4$ and comparing it to standard CS sampling with $R_{net} = 4$. Data were reconstructed with spatial Wavelets as sparsifying transform using the Berkeley Advanced Reconstruction Toolbox (BART) [146]. RMSE of magnitude images and TKE maps and difference images relative to the fully sampled ground truth (GT) were compared.

Data Analysis

TKE [20] maps were calculated according to

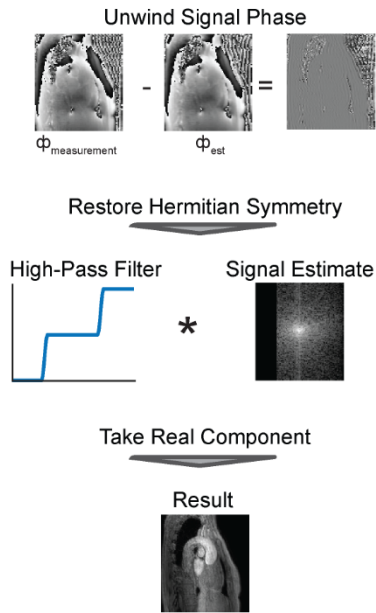
$$TKE = \frac{\rho}{2} \sum_{i=\{1,2,3\}} \sigma_i^2, \text{ with } \sigma_i^2 = \frac{2}{k_{v,i}^2} \ln \left(\frac{|s_0|}{|s_{k_{v,i}}|} \right) \quad (4.11)$$

where σ_i^2 corresponds to the intravoxel standard deviation of fluctuating velocities along dimension i and $\frac{|s_0|}{|s_{k_{v,i}}|}$ is the relative signal magnitude of reference measurement s_0 and the velocity encoded measurement $s_{k_{v,i}}$ encoded with $k_{v,i}$, and ρ is the fluid density. In order to reduce partial volume effects, the in-vivo data were sinc-interpolated to a resolution of 180x180 before calculating TKE maps. Velocity magnitude (speed) images were calculated as the sum-of-squares of the three velocity components.

Root mean square error (RMSE) values of velocity magnitude and TKE data are reported for the region-of-interest comprising the vessel of interest. The respective regions-of-interest for numerical and in-vivo data are indicated by dashed lines in Figure 4.3a and Figure 4.4a.

No ringing filter was used in reconstruction to avoid additional spatial low-pass filtering.

Homodyne Reconstruction (HR)



Projection Onto Convex Sets (POCS)

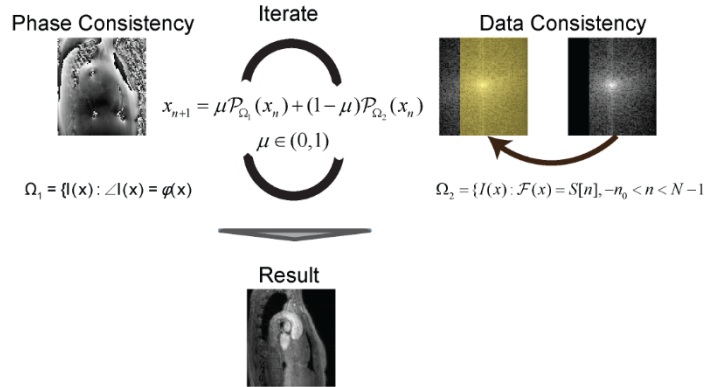


Figure 4.2: Illustration of PF reconstruction methods. Homodyne reconstruction (HR) estimates the signal phase from the symmetrically sampled low-frequency components, rotates the image values into the real plane and then restores Hermitian symmetry. POCS reconstructs an image by iteratively projecting the data onto the set of images which agree with the low-frequency phase estimate and onto the set of images which agree with the acquired k -space data.

4.4 Results

Figure 4.3 compares simulation results of ZF, HR and POCS reconstruction relative to noise-free ground truth (GT), the noisy fully sampled dataset (FULL) and the symmetrically reduced dataset (SYM). It is seen that the RMSE of TKE maps (Figure 4.3a) relative to ground truth is lowest for SYM (1.21%) followed by ZF (1.98%). POCS and HR result in largest errors (4.01% and 4.02%, respectively). The findings are consistent across the range of common SNR values (Figure 4.3b).

Spatial profiles in Figure 4.3c demonstrate the resolution loss incurred by PF and SYM acquisition relative to ground truth. Velocity magnitude images show a higher overall error for ZF than for SYM and FULL (0.28%, 0.22% and 0.13%, respectively) and difference images show the highest deviation from the ground truth data near the stenosis.

Figure 4.4 compares results of ZF, HR and POCS reconstruction relative to the fully sampled in-vivo dataset (FULL) and the symmetrically reduced dataset (SYM) of the in-vivo measurement. The RMSE of TKE maps (Figure 4.4a) relative to the fully sampled data is lowest for SYM (2.45%) followed by ZF (2.93%). POCS and HR result in largest errors (4.93% and 4.34%, respectively). Velocity magnitude images are compared in Figure 4.4b. ZF shows a higher overall RMSE than SYM (2.94% vs. 2.19%).

In Figure 4.5 the PSF resulting from a random undersampling pattern without and with PF acquisition is compared for identical net undersampling factors. PF acquisition leads to increased sidelobe-to-peak ratios as shown in Figure 4.5a. In Figure 4.5b magnitude and TKE maps reconstructed with CS and with CS+PF for $R_{\text{net}} = 4$ are compared. It is seen that the error for PF+CS is highest near sharp edges. Magnitude and TKE maps are reconstructed more accurately for CS than for CS+PF with 1.06% vs. 0.75% for magnitude images and 2.28% vs. 2.69% for TKE maps.

4.5 Discussion

The limitations of PF acquisition in PC-MRI of TKE have been studied using simulated and in-vivo data. It has been demonstrated that image reconstruction enforcing or approximating Hermitian symmetry leads to larger errors than the error incurred by a reduced image resolution at a given number of phase encodes. Moreover, it has been shown that phase images reconstructed with ZF cannot provide higher resolution than symmetric sampling of the same number of phase-encodes sampled around the k-space center.

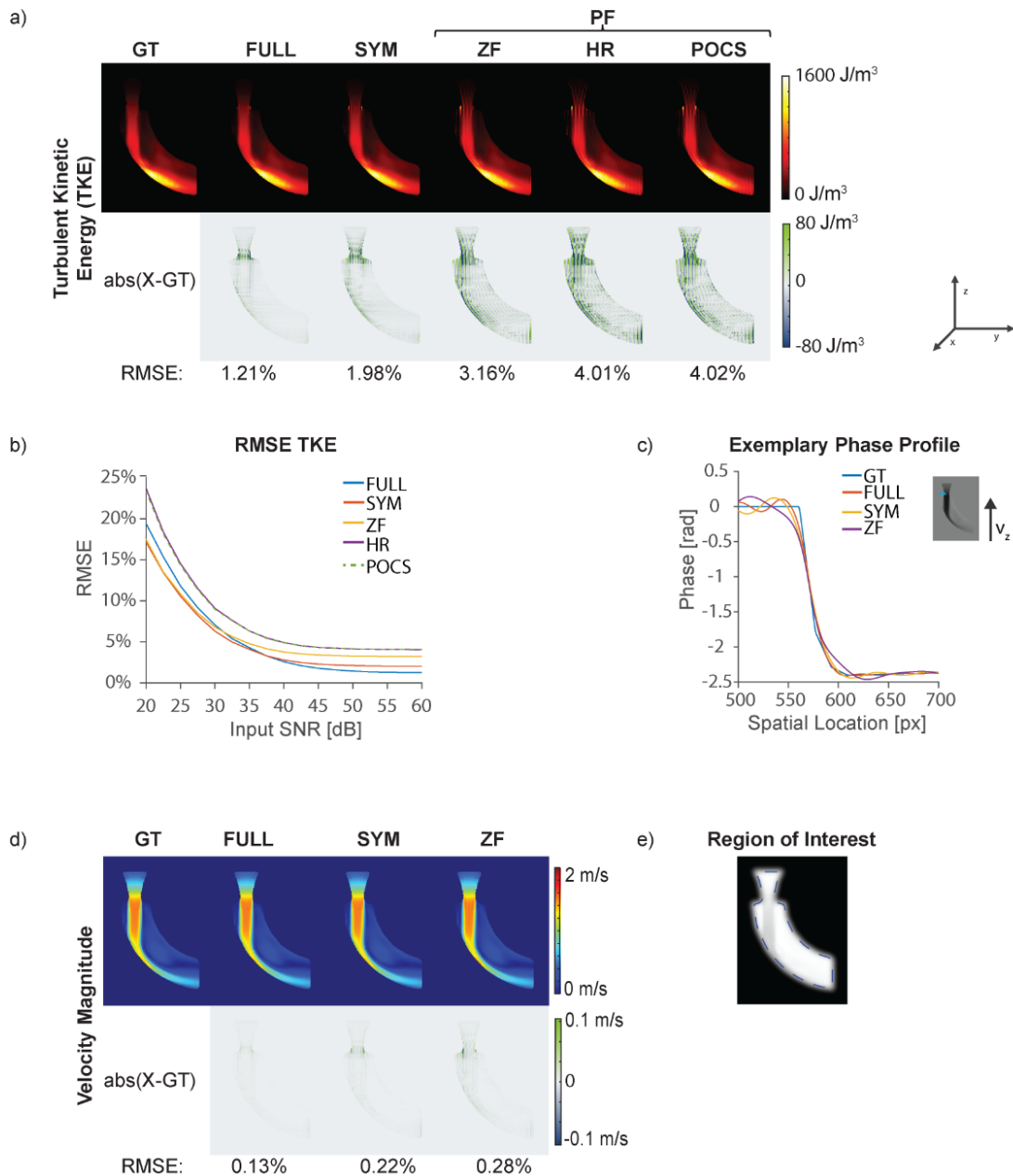


Figure 4.3: Reconstruction results for different sampling strategies applied to CFD data of stenotic flow. a) TKE maps for an exemplary slice. The error in terms of magnitude and TKE is generally higher for HR and POCS than for ZF. However, ZF has a higher RMSE than SYM for magnitude, phase, and TKE images. b) Reconstruction accuracy of magnitude and TKE for different noise levels. c) An exemplary phase profile shows that edges are depicted less accurate in phase images obtained with ZF than with SYM and FULL sampling, implying a higher loss of high-frequency components. d) Velocity magnitude images obtained with ZF show a higher error than SYM or FULL sampling. e) shows the region of interest used for quantitative assessments.

Experiments performed in this study showed, that the performance of methods which enforce Hermitian symmetry, such as HR and POCS, is inferior relative to ZF reconstruction or SYM sampling. This is related to the spatial complexity of the image phase in typical PC-MRI applications which cannot be captured by the phase estimate from low spatial frequencies used to approximate Hermitian symmetry. The finding confirms previous studies [60], [64] in which methods based on Hermitian symmetry did not provide better results compared to ZF reconstruction.

It can be readily seen from Equation 4.9 that the effect of ZF corresponds to a sinc interpolation, where the neighboring voxels are weighted with a phase shift. Consequently, ZF reduces spatial resolution corresponding to the inverse of the bandwidth sampled in k-space. Effectively, an image with lower resolution is obtained, which is modulated in phase due to the shifted sampling window in k-space.

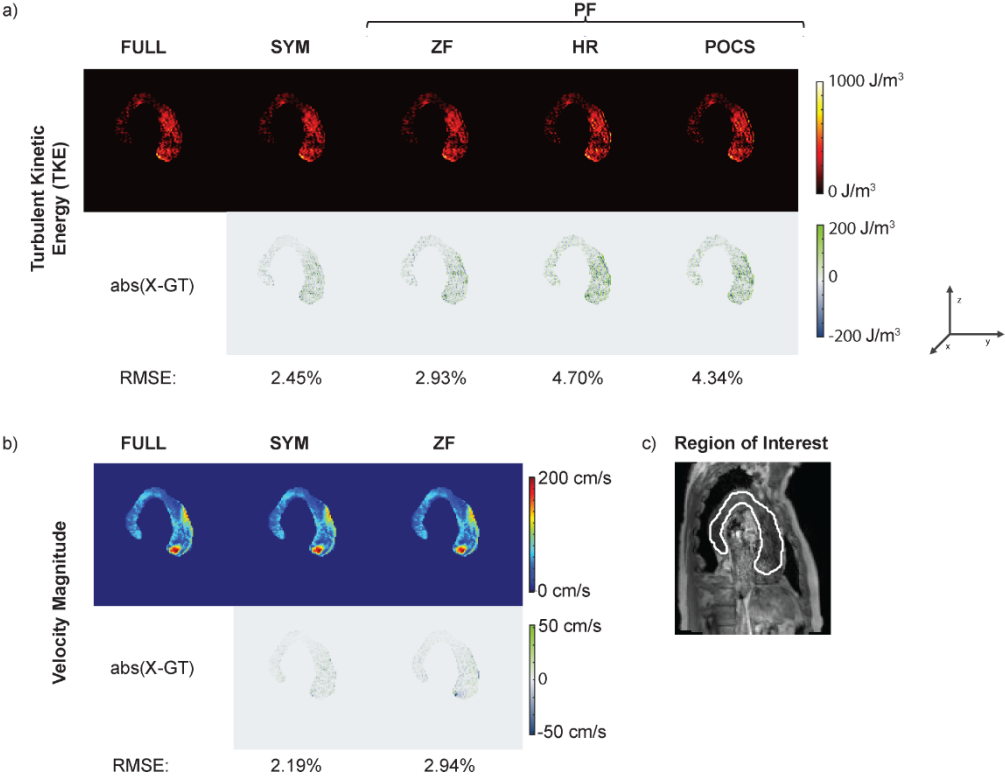


Figure 4.4: Reconstruction results of in-vivo data acquired in the ascending aorta. a) TKE maps obtained from ZF and SYM provide a lower RMSE than HR and POCS. b) Velocity magnitudes are depicted less accurately with ZF than SYM. Difference maps show the highest difference at the center of the jet. e) shows the region of interest used for quantitative assessments.

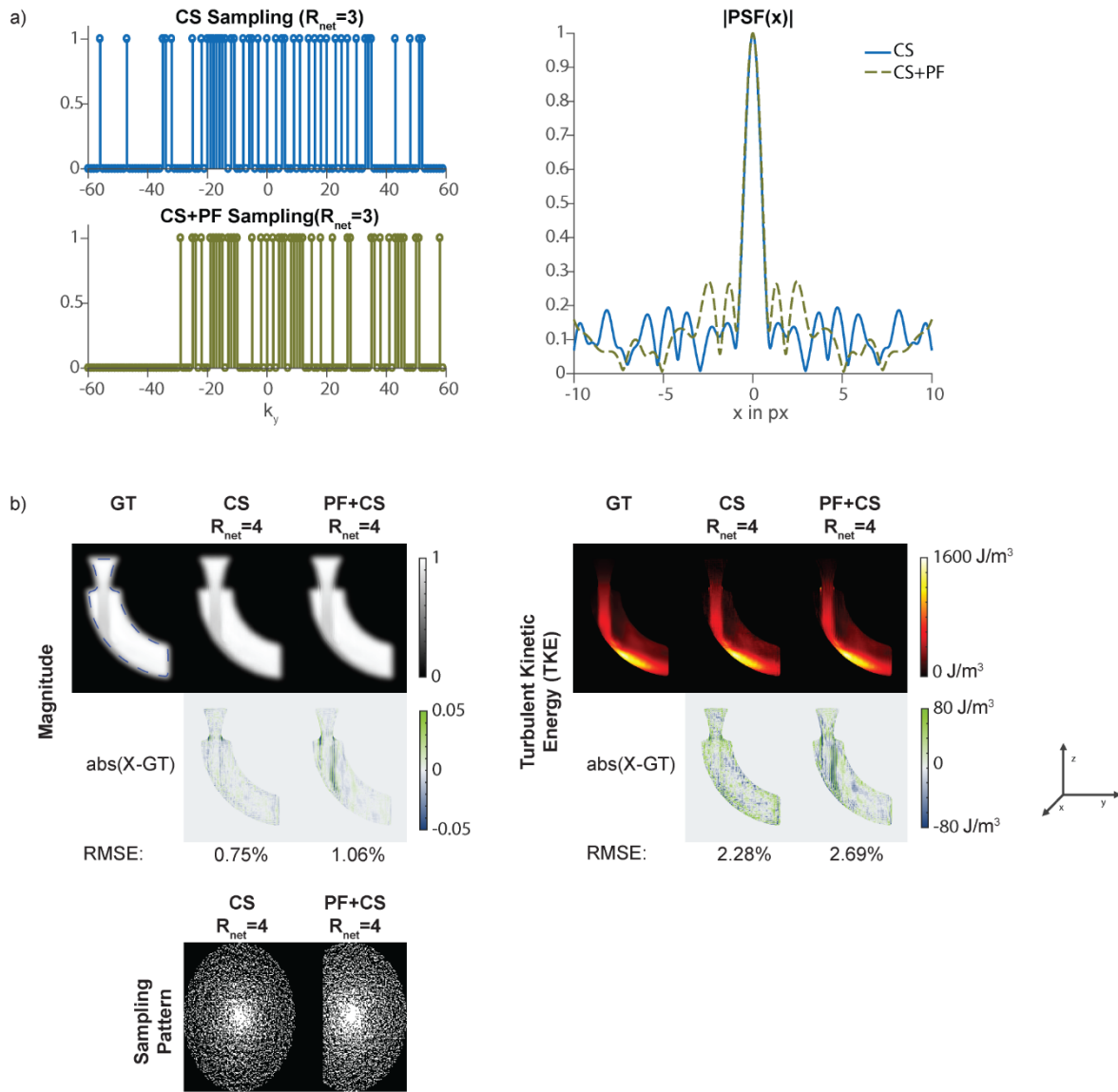


Figure 4.5: Wavelet based sparse recovery for CS and CS+PF. a) CS sampling pattern without and with PF acquisition of 75% and the corresponding point spread functions (PSF). CS shows a lower sidelobe-to-peak ratio than CS+PF. b) Reconstruction results. PF results in inaccuracies at sharp edges which cannot be corrected for by sparse recovery. CS+PF shows a higher RMSE than CS for the same acceleration factor.

Experiments showed SYM sampling to be more accurate in terms of RMSE than ZF for TKE maps and velocity images. SYM sampling leads to ringing artifacts which is a well-understood effect resulting from imaging of a continuous signal with a limited bandwidth [147]. PF, in contrast, leads to more complex truncation artifacts, as illustrated in Figure 4.1b. Truncation artifacts can be mitigated by applying a ringing filter [138] but as this corresponds to spatial low-pass filtering, it also deteriorates spatial resolution. The truncation artifacts observed for ZF lead to modulation of the image with relatively low spatial frequency, compared to ringing artifacts observed for SYM. Therefore, stronger filtering would need to be applied to ZF, thus further reducing the spatial resolution.

This study only considered PF in one phase encode dimension. However, the use of PF was also reported combined in both phase encode dimensions [54], [58]. When applying PF along both phase encode dimensions, restoring Hermitian symmetry only allows to fill missing profiles in one quadrant of k-space whereas the other two quadrants have to be treated with ZF [138], implying a loss of spatial resolution. Assuming a successful reconstruction with HR or POCS in one dimension the reconstructed image would therefore show a directionally dependent resolution.

Partial-echo acquisition is frequently applied to reduce echo time [26], [58], [136], [137]. Even though PE has not been studied in the present work, the image reconstruction approach is equivalent to PF acquisitions and therefore comparable impact on image resolution and TKE is expected. However, by reducing echo time, PE can reduce the effect of intra-voxel phase dispersion in complex and stenotic flows. Consequently, the use of PE will reduce errors due to intra-voxel dephasing at the cost of spatial resolution in case of ZF or it will cause image artifacts when using HR or POCS. O'Brien et al. showed that long echo times can lead to inaccuracies in flow quantification of jet flows[148] and can lead to underestimation of stroke volume in patients with aortic stenosis[149]. On the other hand, the accuracy of viscous and turbulent loss quantification is compromised when the spatial resolution is too low [128]. A conclusive answer on whether to use PE or not must therefore depend on the application and on the parameters assessed.

The use of CS methods to reconstruct high-resolution images from PF acquisitions has been suggested [134]. As shown in Figure 4.5, PF leads to an increased sidelobe-to-peak ratio of the PSF, thus compromising L1-based regularization. In a comparison of CS and CS+PF, standard CS sampling provided a lower RMSE than CS+PF. The increased sidelobe-to-peak ratio manifested itself at edges, where CS+PF showed a higher error. When a phase estimate is available, incorporating the Hermitian symmetry requirement in the CS cost function can improve reconstruction accuracy [129], [132]. Accordingly, an accurate estimate of the signal phase is required. However, given the spatial complexity of the object phase in PC-MRI applications, low-resolution phase maps as available from the data are expected to be not sufficient.

In recent years methods other than HR and POCS to restore Hermitian symmetry have been proposed, often formulating the PF reconstruction as a variational problem where Hermitian symmetry is implemented using a regularization term [129], [132], [150]. However, the underlying assumption that the signal phase can be well represented with a low-frequency estimate remains a limitation.

A limitation of this study is that the key findings were established using retrospectively undersampled CFD data. At the same time, however, the CFD data enabled quantitative evaluations on noise-free input hence allowing to discriminate systematic from random errors. In addition, the effect of PF was confirmed in an in-vivo TKE exam of a patient with dilatation of the ascending aorta and a bicuspid

aortic valve, either known to significantly increase TKE in the setting of aortic stenosis[22] No prospectively undersampled PF scans were used, as performing multiple TKE scans in a single cardiac exam would lead to excessively long scan times, implying a high probability of differences between the scans due to bulk patient motion.

This study focused on PC-MRI of TKE. However, methods which enforce Hermitian symmetry will lead to artifacts for any application where strong spatial phase variations occur.

In summary, Hermitian symmetry cannot be used as a prior to recover missing samples in PC-MRI of complex flow. Accordingly, efforts to reduce scan time in PC-MRI should aim to exploit correlations present in the high-dimensional datasets using iterative image reconstruction approaches[34], [63], [88], [97], [151] instead of using PF acquisitions.

4.6 Conclusion

Exploiting Hermitian symmetry in Partial Fourier reconstruction of TKE maps from phase-contrast data does not yield a benefit over zero-filling. In consequence, symmetric sampling is preferred over Partial Fourier acquisition for a given number of phase-encodes in PC-MRI.

4.7 Acknowledgements

The authors acknowledge Sebastiano Caprara for providing the CFD data.

4.8 Supplementary Information

Influence of the Window Function in Homodyne Reconstruction

In HR, inconsistencies at the transition between synthesized and acquired data at k_0 lead to artifacts in the reconstructed image. To reduce these inconsistencies, the transition can be smoothed with a linear ramp or an cosine tapered window [138] (also known as asymmetric Hanning window [140]).

To find out the best setting for the transition region, reconstruction accuracy was assessed in terms of RMSE for the cosine tapered window and the linear ramp transition with varying width of the transition region. A unit-step transition was considered by allowing for a transition region width of 0px.

For the noise-free CFD dataset (Figure S4.1a), a linear ramp performs consistently better than the cosine tapered window. The best result is obtained for a unit step transition with an RMSE of 4.0%. A local minimum with an RMSE of 4.3% can be observed for the linear ramp at a transition region width

of 8px. In an exemplary slice, similar artifacts can be observed for a unit step and the linear ramp with 8px width. Both filter profiles can be seen in Figure S4.1c.

For the in-vivo dataset (Figure S4.1b), the linear ramp transition and cosine taper transition provide similar results. Both rise rapidly with an increasing transition region size. Again the unit-step transition provides the lowest RMSE.

The best experiment results were obtained for a unit-step transition. Further reducing the spatial resolution of the low-frequency phase estimate by smoothing the transition region and attenuating the acquired data by applying a smooth transition further reduces reconstruction accuracy. For noise-free data, using a small transition region of 8px provides an RMSE which is only 0.3% higher than for a unit-step transition. In contrast, for the noisy in-vivo scan, smoothing the transition region rapidly deteriorates the RMSE. This is in agreement with the finding by Noll et al. [37] that smoothing the transition region incurs a loss in SNR.

Following this experiment, a unit step transition was selected for all HR reconstructions, as it provided the lowest RMSE.

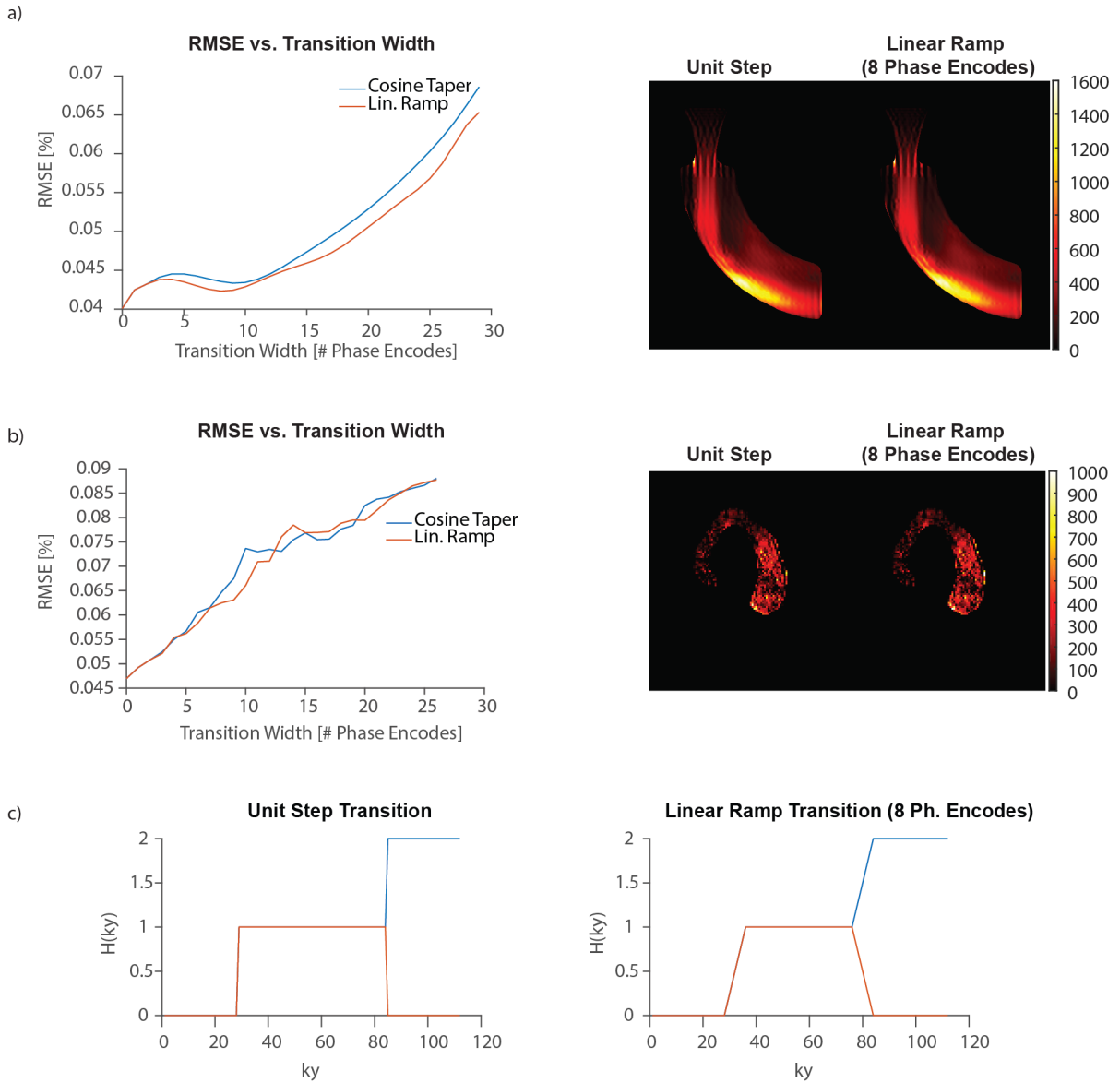


Figure S4.1: HR reconstruction results with different transition region windows and exemplary results for a unit step transition (width = 0) and a window width of 8px are shown for the phantom dataset (a) and the in-vivo dataset(b). c) shows the filter profiles.

Chapter 5 Multipoint 5D Flow Imaging - Accelerated Cardiac- and Respiratory-Motion Resolved Mapping of Mean and Turbulent Velocities

Published in: J. Walheim, H. Dillinger, and S. Kozerke, "Multipoint 5D Flow Cardiovascular Magnetic Resonance - Accelerated Cardiac- and Respiratory-Motion Resolved Mapping of Mean and Turbulent Velocities," *J. Cardiovasc. Magn. Reson.*, 2019.

5.1 Background

A key challenge of encoding mean and turbulent velocities relates to achieving appropriate measurement sensitivity to both quantities. For the expected ranges of mean and turbulent velocities in-vivo, multiple velocity encodings per spatial direction are preferably obtained and combined during image reconstruction [58]. This approach, however, requires additional data and hence data undersampling is necessary to arrive at clinically acceptable scan times.

Significant scan time reductions in 4D Flow MRI have been achieved using combinations of parallel imaging and compressed sensing [152], k-t methods [153], [154], radial [155] or spiral [156] acquisitions. Various modifications to the way data are sampled and reconstructed have been described, e.g. [34], [50], [88], [90], [97], [157]. In general, however, scans remain too long to be performed in breathholds. Moreover, data acquisition without respiratory motion compensation leads to decreased image quality [50]. Accordingly, navigator-based respiratory gating is typically employed [51]. Unfortunately, respiratory gating makes scan times unpredictable, as gating efficiencies vary among subjects and often even during a single scan. Clinically, this may lead to conflicts as scan slots have typically fixed durations.

Instead of using respiratory gating, respiratory-motion resolved imaging [36], [55], [56], [158] has been proposed to address respiratory-motion related image artifacts. To this end, data are acquired continuously throughout the respiratory motion cycle and sorted afterwards during the image

reconstruction task into discrete motion states based on a respiratory motion signal surrogate [56], [159]. Accordingly, data correlation not only along the cardiac phase dimension but also along the respiratory motion dimension can be exploited.

Data correlations lead to low-rank properties of the decoding problem to be solved in image reconstruction. Various studies have demonstrated that these low-rank characteristics are most efficiently exploited using local rather than global low-rankness using patch-based decomposition of the multi-dimensional data [33], [98].

The objective of the present work was to implement and test respiratory-motion resolved Bayesian multipoint 5D Flow MRI for mapping both mean and turbulent velocities in the aorta with a fixed scan time.

5.2 Methods

Data Acquisition and Respiratory Motion Binning

The data acquisition and motion binning process is illustrated in Figure 1. Data are sampled using a pseudo-radial Cartesian sampling pattern which maps radial spokes onto a Cartesian grid [56], [160]. Using the Golden angle principle [62], [161], spatial incoherence of temporally adjacent frames is ensured. To reduce eddy current effects and keep the acoustic noise level during the measurement to a minimum, the tiny Golden angle concept was employed to avoid large jumps in k-space [161].

Data-driven respiratory motion detection [162] was performed as illustrated in Figure 2a) using repetitive sampling of profiles through the k-space center $d(k_x, t) = d(k_x, k_y = 0, k_z = 0, t)$ as part of the pseudo-radial Cartesian sampling pattern. Upon inverse Fourier transform of $d(k_x, t)$, the projection $X(x, t)$ of the excited volume resolved along the frequency encode direction x and over time t was obtained, showing signal modulation depending on respiratory and cardiac motion. Given $TR = 3.3 \text{ ms}$ and with one in 21 readouts through the k-space center, a respiratory sampling rate of ca. 14 Hz was obtained. The signal of each coil channel was treated as a separate signal $X_i \in \mathbb{C}^{N_x \times N_t}$; $i \in \{1, 2, \dots, nCoils\}$, with N_x being the number of samples in readout dimension and N_t the number of

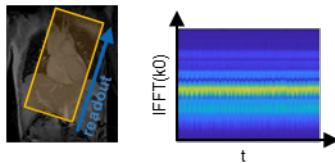
readouts through the k-space center. Only the magnitude was considered, as the main variation in signal phase was found to be related to the different velocity encodings which were alternated per heart beat (beat-interleaved) and which led to phase variations which were too large to be eliminated by lowpass filtering.

Singular value decomposition was performed and the 2nd singular vector of $\text{abs}(X^T X)$ was selected, as it provided the predominant motion for each coil channel (Figure 2b). To isolate respiratory motion, a lowpass filter was applied to limit the spectrum to frequencies below 0.6 Hz (Figure 2c). Next, coil channel clustering [160] was performed to determine the predominant dynamics among all channels which were assumed to be the respiratory motion signal (Figure 2d). Finally, the average over all these signals was calculated to provide the final respiratory motion signal surrogate (Figure 2e).

a) Golden Angle Acquisition



b) Motion Detection



c) Binning

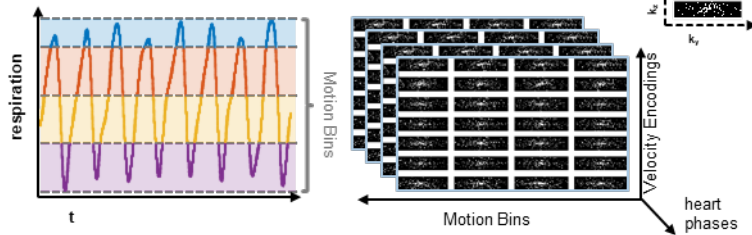


Figure 5.1: 5D Flow data acquisition. a): Data are sampled using a Cartesian pseudo-radial tiny Golden angle sampling pattern [33]. b): Respiratory motion state detection is derived from profile $d(k_x, k_y = 0, k_z = 0)$, which is repeatedly acquired and processed using a combination of principal component analysis, lowpass filtering, and coil-clustering [37]. Each spoke is composed of 21 k-space profiles, one of them always through the k-space center. With $T_r = 3.3$.ms, respiratory motion is sampled at ca. 14 Hz. c): Acquired data are sorted into four discrete respiratory motion states such that the acceleration factor for each motion state is similar.

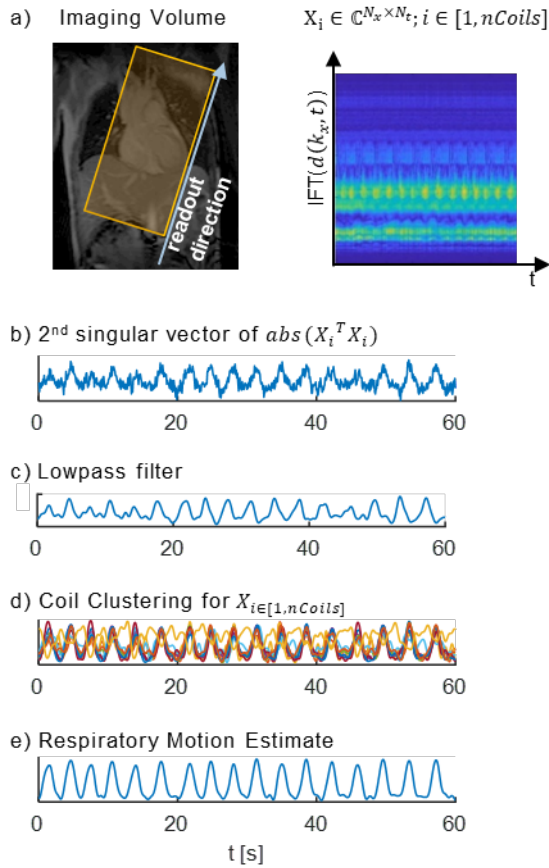


Figure 5.2: Data driven respiratory motion detection. a) Respiratory motion is extracted from the profiles through the k -space center $d(k_x, k_y = 0, k_z = 0)$. The temporal evolution of readouts through the k -space center shows a modulation with respiratory motion and cardiac motion. b) The 2nd principal component provides the main variation of the signal. c) A lowpass filter limits the spectral components to the expected frequency range of respiratory motion. d) Coil clustering is used to combine the signals from different channels and provides a final estimate of respiratory motion.

Motion-Resolved Image Reconstruction

Using the respiratory motion surrogate signal, the acquired data were distributed across discrete motion bins. A total of four motion bins was defined and the width of each motion bin was set to achieve a similar undersampling factor for each respiratory motion state and cardiac phase by setting the bin boundaries to the 0.25-, 0.5- and 0.75-quantile of the respiratory motion signal. For some combinations of respiratory motion state, heart phase and velocity encoding, this approach led to very low sampling rates. Therefore, a data sharing approach [163], [164] was used to fill up frames with acceleration factors higher than 20 with data from neighboring respiratory motion states.

Accordingly, the final data vector reads $\mathbf{d} \in \mathbb{C}^{N_x N_c N_{hp} N_{kv} N_{rs}}$, with N_x being the number of samples in the spatial frequency domain, N_c denoting the number of coils, N_{hp} heart phases, N_{kv} velocity

encodings and N_{rs} respiratory motion states. A locally low rank (LLR) [33], [98] approach was used to exploit correlations among heart phases (hp) and respiratory motion states (rs). Image-domain data for each velocity encoding $\mathbf{s}_{k_v} \in \mathbb{C}^{N_x N_{hp} N_{rs}}$ were reconstructed separately as:

$$\hat{\mathbf{s}}_{k_v} = \underset{\mathbf{i}_{k_v}}{\operatorname{argmin}} \|\Omega \mathcal{F} \mathcal{C} \mathbf{s}_{k_v} - \mathbf{d}_{k_v}\|_2^2 + \lambda \sum_{b=1}^{N_b} \|\mathcal{R}_b(\mathbf{s}_{k_v})\|_* \quad (5.1)$$

with the undersampling operator Ω , Fourier transform \mathcal{F} , coil sensitivity mapping \mathcal{C} , k-space data \mathbf{d}_{k_v} and regularization weight λ . As illustrated in Figure 3a), the operator \mathcal{R}_b selects the b -th out of N_b blocks of size $n_x \times n_y \times n_z$ in the image from all N_{hp} heart phases and N_{rs} respiratory motion states and transforms them into a Casorati matrix with dimensions $n_x n_y n_z \times N_{hp} N_{rs}$. By penalizing the nuclear norm of this local Casorati matrix, low-rankedness is enforced locally.

For comparison, respiratory-motion resolved data were also reconstructed by penalizing total variation along the respiratory motion states and heart phases (TV) [36]:

$$\hat{\mathbf{s}}_{k_v} = \underset{\mathbf{i}_{k_v}}{\operatorname{argmin}} \|\Omega \mathcal{F} \mathcal{C} \mathbf{s}_{k_v} - \mathbf{d}_{k_v}\|_2^2 + \lambda_{hp} TV_{hp}(\mathbf{s}_{k_v}) + \lambda_{rs} TV_{rs}(\mathbf{s}_{k_v}) \quad (5.2)$$

where λ_{hp} and λ_{rs} denote the regularization weights along cardiac phases and respiratory motion states, respectively.

Multipoint Velocity Encoding and Decoding

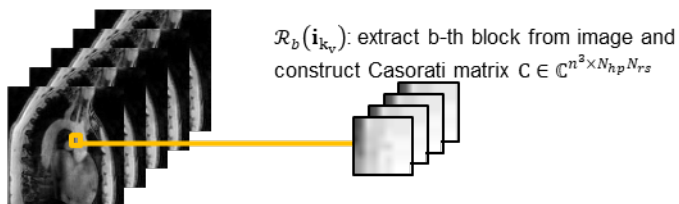
Assuming a Gaussian distribution of intra-voxel velocities, the following signal model of mean velocity \bar{v} and fluctuating component with standard deviation σ [20] was used:

$$s(\mathbf{k}_v) = s_0 e^{\frac{-\sigma^2 k_v^2}{2}} e^{-i \mathbf{k}_v \bar{v}} \quad (5.3)$$

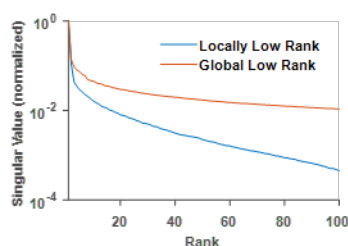
where \mathbf{k}_v is related to the first gradient moment of a bipolar velocity encoding gradient by $\mathbf{k}_v = \gamma \int_0^T t \mathbf{G}(t) dt$, with T being the time of application of gradient waveform $\mathbf{G}(t)$ and determines the encoding velocity as $v_{enc} = \frac{\pi}{k_v}$.

a) Locally Low Rank Reconstruction

$$\hat{\mathbf{i}}_{k_v} = \underset{\mathbf{i}_{k_v}}{\operatorname{argmin}} \|\Omega\mathcal{F}\mathcal{S}(\mathbf{i}_{k_v}) - \mathbf{d}\|_2^2 + \lambda \sum_b \|\mathcal{R}_b(\mathbf{i}_{k_v})\|_*$$



Singular Values for Local vs. Global Casorati Matrix



b) Multipoint Encoding and Decoding

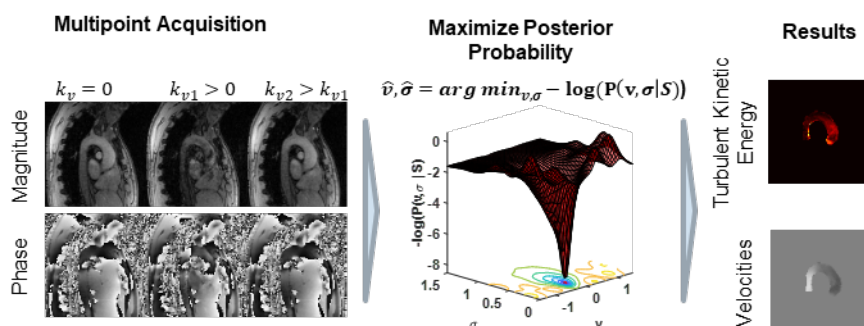


Figure 5.3: Image reconstruction using locally low rank approach followed by Bayesian multipoint unfolding. a) A locally low rank approach is employed for each velocity encoding separately. The locally low-rank model divides the image into 3-dimensional patches. Each patch is reordered into local Casorati matrices for which a low rank is enforced by penalizing the nuclear norm. Compared to a global Casorati matrix, the values of the singular values decrease more rapidly. Following reconstruction of the individual velocity encodings, for each Cartesian direction, the different velocity encodings k_v are combined using a Bayesian multipoint approach. A Bayesian probability model [4] provides posterior probabilities for mean velocity v and intra-voxel standard deviation σ given the measured signal S . v and σ are chosen such that the posterior probability is maximized, providing maps of turbulent kinetic energy (TKE) and mean velocities.

The signal model implies a trade-off between a sufficiently high encoding velocity v_{enc} to avoid phase wraps [52], and a sufficiently high encoding efficiency of the fluctuating velocity components [165] such that $v_{enc} \sim \sigma$. It has been demonstrated that this trade-off may lead to insufficient sensitivity to

fluctuating velocity components and hence a multipoint encoding scheme using two instead of one k_v encoding point per axis was implemented [58]. Using the probability map $P(\bar{v}, \sigma | D, S)$, pixel-wise estimates of mean velocity \bar{v} and intra-voxel standard deviation σ given the model S and the measured image data D were obtained [58]. Data acquired with different k_v 's were combined by choosing the values for \bar{v} and σ maximizing the posterior probability of the measured data:

$$\hat{\bar{v}}, \hat{\sigma} = \arg \max_{\bar{v}, \sigma} P(\bar{v}, \sigma | D, S). \quad (5.4)$$

An illustration of multipoint acquisition and Bayesian decoding is provided in Figure 3b).

In-vivo Study

All in-vivo work was performed upon written informed consent of the subjects and according to local ethics regulations. Data of the ascending aorta of nine volunteers (age 30 ± 11 , 6 male, 3 female) were acquired on a 3T Philips Ingenia system (Philips Healthcare, Best, the Netherlands) using the proposed 5D Flow MRI and a standard, navigator-gated 4D Flow MRI approach [52] with a spatial resolution of $2.5 \times 2.5 \times 2.5 \text{ mm}^3$, $T_E = 3.3 \text{ ms}$, $T_R = 4.9 \text{ ms}$, flip angle = 8 and 25 cardiac phases. The different velocity encodings were alternated per heart beat. The image acquisition matrix was $N_{readout} = 100 \pm 9$, $N_{phase} = 101 \pm 8$ and $N_{slice} = 20 \pm 1$ (mean \pm std). Using the proposed method, velocities were encoded with $v_{enc} = 50 \text{ cm/s}$ and 150 cm/s per axis and an additional $v_{enc} = 0 \text{ cm/s}$ measurement. Scan time was fixed to 4 minutes. After sorting the data into 4 respiratory motion states, acceleration factors were 19.0 ± 0.21 (mean \pm std). On average the view-sharing approach led to 61% of the total number of acquired samples being shared among motion bins in the study cohort.

Standard 4D Flow MRI was recorded with a single venc ($v_{enc} = 150 \text{ cm/s}$) per axis (4D Flow Ref). Two-fold acceleration using parallel imaging [38] and standard pencil-beam navigator gating on the diaphragm (5mm gating window) was employed with the 4D Flow reference protocol. Accordingly, the effective scan time depended on the breathing pattern of the subjects. All measurements were performed with retrospective cardiac gating and a 28-channel receiver coil.

Prior to image reconstruction, the 28-channel data were compressed to 8 virtual channels [166]. The LLR reconstruction (Equation 5.1) was solved using an implementation of the fast iterative shrinkage-thresholding algorithm (FISTA) [77] provided with the Berkeley advanced reconstruction toolbox (BART) [167]. A patch size of $n_x = n_y = n_z = 8$ was used for the locally low-rank constraint. The TV reconstruction (Equation 5.2) was performed with an adapted version of the code provided with [36]. The standard 4D Flow reference data were reconstructed with MRecon (GyroTools LLC, Zurich, Switzerland). Sensitivity maps were estimated from a separate scan using the ESPIRiT method [69]. The regularization hyperparameters λ in Equation 5.1 and λ_{np} and λ_{rs} in Equation 5.2 were optimized for best agreement of velocity components in systole with data of the 4D Flow reference measurement:

$$\hat{\lambda} = \underset{\lambda}{\operatorname{argmin}} \|\mathbf{v}_{recon}(\lambda) - \mathbf{v}_{ref}\|_1. \quad (5.5)$$

Equation 5.4 was minimized using the *bayesopt* function in MATLAB R2017b (The MathWorks, Natick, MA) [168]. Resulting hyperparameters were $\lambda = 0.01$ for Equation 5.1 and $\lambda_{np} = 0.04$ and $\lambda_{rs} = 0.05$ for Equation 5.2. For both optimizations, the number of iterations was set to 80.

Data Analysis

Upon image reconstruction, concomitant gradient terms were corrected [144] and third-order background phase correction was applied [145], [169]. Segmentation of the aorta was performed using ITK-SNAP. The same masks were used for 4D Flow reference data and data in expiration obtained with 5D Flow LLR and 5D Flow TV. Maximum intensity projections (MIP) of velocity magnitude and TKE maps in systole were calculated as:

$$Im_{MIP}(x, y) = \arg \max_z (Im(x, y, z)). \quad (5.6)$$

In order to avoid noise at the vessel boundaries the segmentation masks were eroded by one pixel for MIP projections.

The normalized root-mean-square error (nRMSE) of the velocity magnitude in the segmented aorta was calculated according to:

$$nRMSE = \sqrt{\frac{\sum_{ROI} (\mathbf{v} - \mathbf{v}_{ref})^2}{|ROI| * \max(\mathbf{v}_{ref}^2)}} \quad (5.7)$$

where $|ROI|$ corresponds to the number of voxels in the segmentation mask.

TKE was calculated voxel-wise as:

$$TKE = \frac{\rho}{2} (\sigma_x^2 + \sigma_y^2 + \sigma_z^2) \quad (5.8)$$

where σ_j^2 denotes the variance of velocity deviations per direction j and ρ is the fluid density (here we assumed 1060 kg/m^3 for blood).

Moreover, multi-planar reslicing along the aorta was conducted using VMTK (www.vmtk.org) and peak flow and peak through-plane velocities (i.e. the maximum velocity component in the corresponding cross-section of the aorta) were assessed for each plane. Peak through-plane velocities were determined upon application of a 3x3x3 median filter to reduce contributions from noise.

The effectiveness of respiratory-motion resolved 5D Flow MRI was assessed by comparing it to reconstructions using only data from the end-expiratory bin (EXP) and to reconstructions using no respiratory binning (NG).

To assess the performance of navigator gating in the standard 4D Flow MRI protocol, the positions measured by the navigator on the diaphragm were interpolated and each readout was attributed its corresponding navigator position. Then, mean and standard deviations of the acceptance window per heart phase were calculated. Due to the coarse temporal resolution of the navigator signal (one navigator per heart beat), linear interpolation was chosen in order to provide a lower bound on the width of the acceptance window for different cardiac phases.

Statistical Analysis

Bland-Altman analysis [170] of peak flow and peak through-plane velocities was performed to assess the agreement of velocity fields obtained with 5D Flow LLR and the 4D Flow reference.

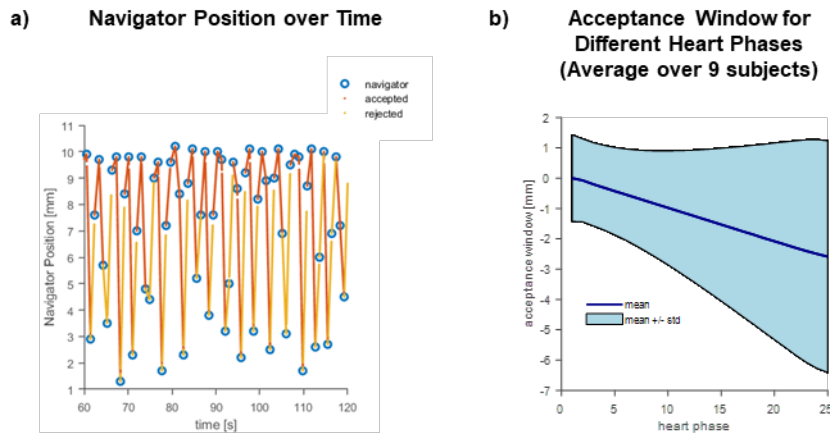


Figure 5.4: Analysis of navigator-based respiratory gating in standard 4D Flow MRI. a) For an exemplary 4D Flow scan the diaphragm position measured by the pencil beam navigator over time is shown together with accepted data (red) and rejected data (yellow). When the navigator signal is within the acceptance window, data of all cardiac phases of are accepted until the next navigator position is obtained. As a result, the effective acceptance window of the data varies as a function of heart phase and becomes wider towards diastole as shown in b).

5.3 Results

Scan durations for 4D Flow MRI were 17.8 ± 3.7 min compared to 4 minutes for the 5D Flow protocol.

Figure 4 provides an analysis of the acceptance window for respiratory gating with one pencil beam navigator per cardiac cycle as being used in the 4D Flow reference measurements. If the navigator signal was within the acceptance window, data of all cardiac phases were accepted. This results in a wider acceptance window for later cardiac phases leading to corresponding uncertainty about the actual motion states and increasing image artifacts for later cardiac phases.

Reconstructions exploiting respiratory motion states (5D Flow LLR) are compared to using only data in end-expiration (EXP LLR) and without gating (NG LLR) in Figure 5. Magnitude images and TKE maps from 5D Flow LLR reconstructions show less artifacts compared to EXP LLR and NG LLR reconstructions.

Magnitude and velocity magnitude images for the end-expiratory motion state obtained with 5D Flow LLR and 5D Flow TV are compared relative to the 4D Flow reference in Figure 6. It can be seen that

maximum intensity projections of velocity magnitudes are similar for all methods while TKE maps and magnitude images provided by 5D Flow TV show more residual aliasing when compared to 5D Flow LLR. The RMSE of the reconstructed images was lower for 5D Flow LLR compared to 5D Flow TV for both magnitude and velocity magnitude (8.7% vs. 13.5% for and 7.9% vs 9.8%, respectively). Maps of TKE for all 9 volunteers obtained with 5D Flow LLR and the 4D Flow reference are compared in Figure 8. In general, TKE maps derived from the 4D Flow reference show a higher noise level compared to 5D Flow data.

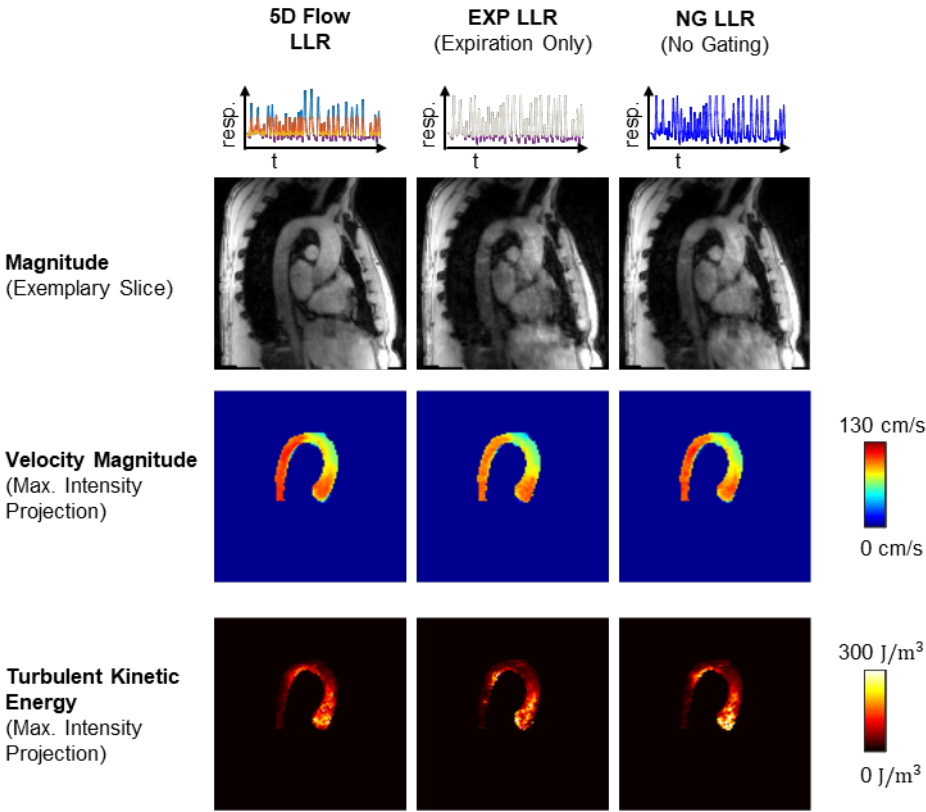


Figure 5.5: Comparison of 5D Flow LLR reconstructions in expiration relative to reconstructions using end-expiratory data only (EXP LLR) and without gating (NG LLR). 5D Flow LLR shows reduced aliasing artifacts in the magnitude, velocity and TKE maps. For both EXP LLR and NG LLR, residual motion artifacts are present in the magnitude images and increased noise is observed in the TKE maps.

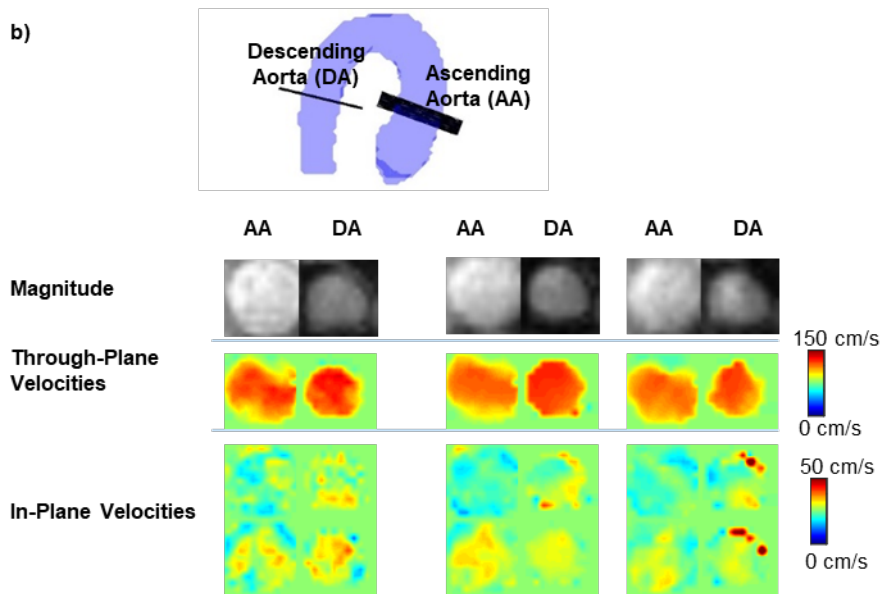
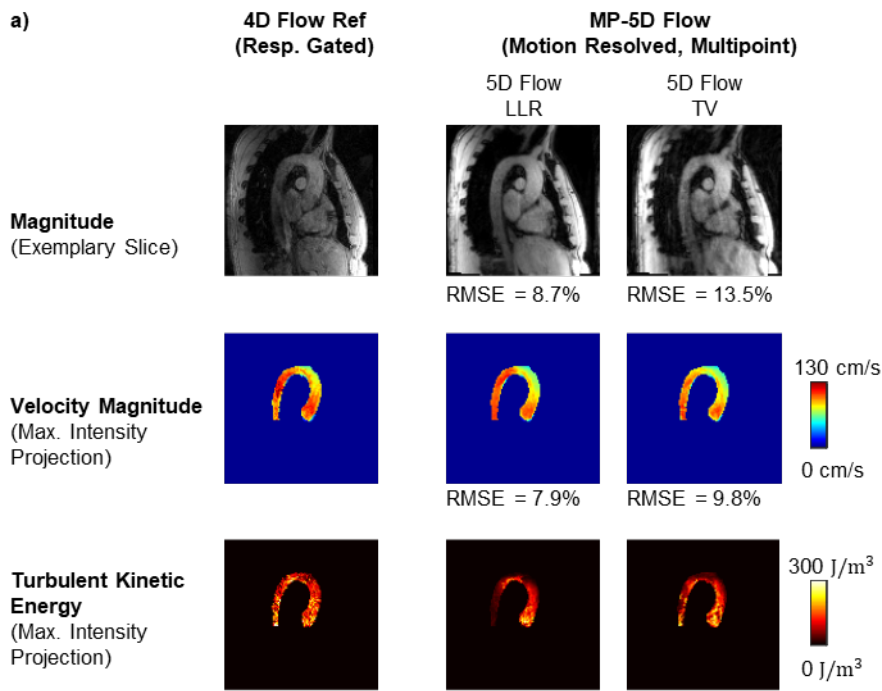


Figure 5.6: Results in systole comparing 5D Flow LLR with 5D Flow TV and standard 4D Flow. For 5D Flow TV and the 4D Flow reference residual aliasing is observed in the magnitude images. Moreover, the TKE maps obtained with 5D Flow TV and the 4D Flow reference show more noise compared to 5D Flow LLR. Exemplary slices in the ascending aorta (AA) and descending aorta (DA) show qualitatively similar results for through-plane velocities in the ascending aorta whereas in the descending aorta artifacts can be observed in the in-plane velocity components for 5D Flow TV.

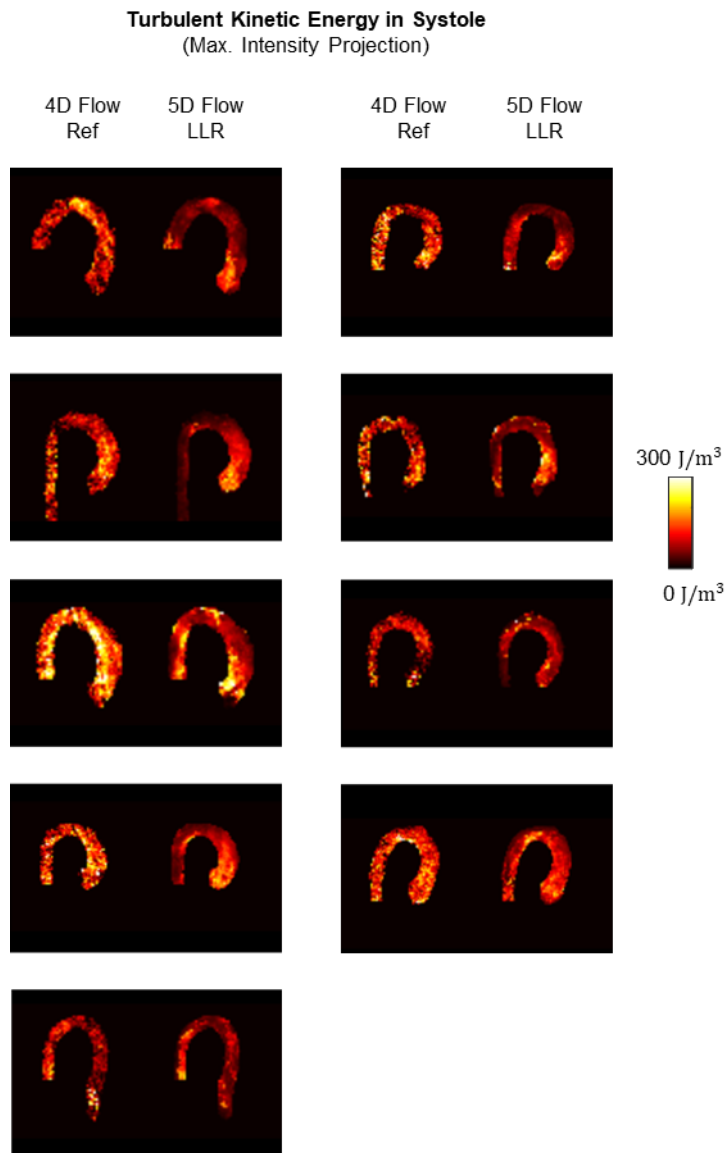


Figure 5.7: Comparison of TKE maps in systole for the 4D Flow reference versus 5D Flow LLR. In the 4D Flow reference data increased noise compared to 5D Flow LLR is seen. Moreover, TKE maps from 4D Flow show high values in the descending aorta whereas TKE values are lower in the descending aorta for most cases with 5D Flow LLR.

Exemplary slices in the ascending and descending aorta show through-plane velocity profiles to be in agreement among the 4D Flow reference and 5D Flow LLR whereas 5D Flow TV shows artifacts in the descending aorta.

Exemplary magnitude and velocity magnitude images for different respiratory bins reconstructed with 5D LLR are shown in Figure 7 along with an exemplary respiratory curve. Bins in expiration are narrower as the duration of expiration was longer compared to inspiration. The displacement of the heart and

aorta is clearly seen in both magnitude and velocity maps. While image quality is acceptable, there is degradation present from end expiration to end inspiration.

Figure 9 compares velocity fields, peak velocities and peak flow obtained for all 9 volunteers. The nRMSE between the velocity magnitudes obtained with 5D Flow LLR and the 4D Flow reference was 8.9 ± 2.1 %. On average, 5D Flow LLR shows good agreement of peak velocities and peak flow relative to the 4D Flow reference (peak velocities: 3.1 ± 4.4 %, peak flow: -2.4 ± 6.9 %).

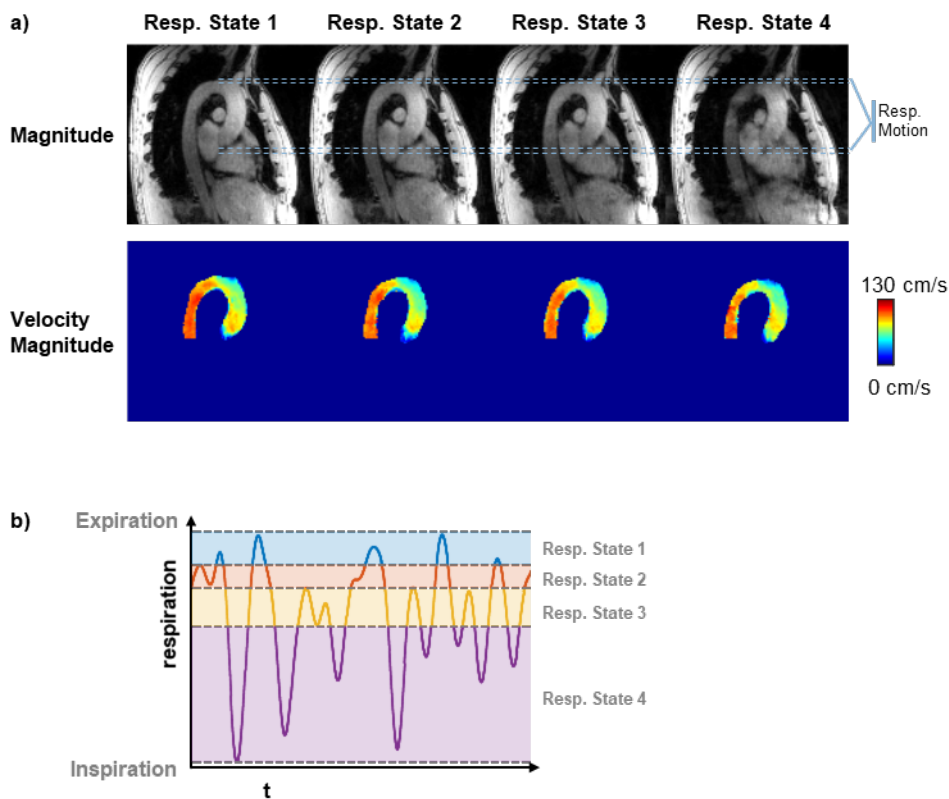


Figure 5.8: a) Exemplary magnitude and velocity magnitude images for different respiratory bins reconstructed with 5D LLR. Image quality reduces from end expiration to end inspiration and artifacts can be observed in the descending aorta in the magnitude and velocity images reconstructed in end inspiration. b) The respiratory curve shows that the expiratory bins have a narrower range of motion than inspiratory bins.

Multiplanar Reslicing
(9 datasets, 18 planes)



| Duration 4D Ref [min] (m ± std) | Duration 5D Flow LLR [min] | |
|------------------------------------|------------------------------|------------------------|
| 17.81 ± 3.66 | 4.00 | |
| nRMSE Velocity Magnitude | Peak Velocities (m ± std) | Peak Flow (m ± std) |
| 8.9% ± 2.1% | 3.1% ± 4.4% | -2.4% ± 6.9% |

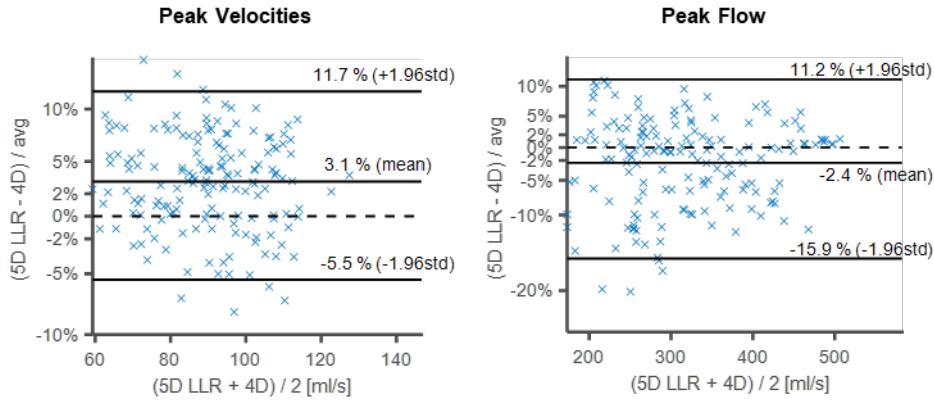


Figure 5.9: Quantitative analysis of results. Scan times, peak through-plane velocities and peak flow for 5D Flow LLR reconstructions are compared to the 4D Flow reference. Duration of the 5D Flow LLR acquisition is on average ca. 4.5 lower than for 4D Ref. Bland-Altman analysis shows a mean difference of 3.1% and -2.4% and limits of agreement of $\pm 8.6\%$ and $\pm 13.6\%$.

5.4 Discussion

In this work, a respiratory-motion resolved Bayesian multipoint 5D Flow MRI approach has been implemented based on pseudo-radial tiny Golden angle Cartesian sampling in conjunction with locally low-rank image reconstruction to map mean and turbulent velocities in the aorta in a fixed scan time of 4 minutes.

By exploiting data from all respiratory motion states, the duration of 5D Flow MRI becomes independent of the individual respiratory motion patterns of the subjects. In comparison to standard 4D Flow MRI protocols [52], 5D Flow MRI is about 4.5 times shorter on average. Whereas pencil-beam based navigator gating in standard 4D Flow MRI cannot ensure motion-free data across the entire cardiac cycle, as demonstrated in Figure 4, repetitive data-driven respiratory motion detection and continuous data acquisition of 5D Flow MRI provide motion estimates throughout the cardiac cycle.

It has been demonstrated that the LLR model allows to improve reconstruction accuracy relative to using data from end expiration only, as shown in Figure 5. Of note, low-rank models have been used to exploit correlations in dynamic MRI [35], [71], [73] and have already been proposed for reconstructing respiratory-motion resolved data. However, existing approaches confine the reconstruction to a subspace defined by basis functions along the respiratory motion dimension either by combining cardiac and respiratory motion in a Casorati matrix [55] or by means of low-rank tensor factorization [100], [101]. These approaches either require the acquisition of a separate scan to estimate a subspace or a subspace has to be estimated from undersampled k-space data, e.g. via low-rank tensor factorization [100]. The first option increases scan time and can lead to problems when there is a mismatch between both scans (e.g. bulk motion) while the second option adds complexity to the reconstruction as another hyperparameter needs to be optimized for subspace estimation prior to reconstruction of the actual image. In comparison, the LLR model proposed in the present work can be applied straight-forwardly by penalizing the nuclear norm of the data rearranged in a Casorati matrix.

When comparing the 5D Flow LLR reconstruction with the 5D Flow TV approach, both methods showed good agreement of velocity data relative to the 4D Flow reference. However, TKE maps and magnitude images exhibit less noise when using the 5D Flow LLR approach. The inferior performance of the TV approach is associated with the piecewise constant solutions favored by TV which in turn leads to smoothing of peak values. To reduce underestimation of peak velocities, hyperparameters may be determined for best agreement with reference velocities. However, this led to non-optimal results for magnitude images which therefore still showed a high degree of aliasing noise.

In-vivo, good agreement of peak velocities and peak flow values of 5D Flow LLR with data derived from standard 4D Flow MRI was found. A small bias towards higher velocities was observed for 5D Flow LLR compared to the 4D Flow reference. This can be related to previous findings that respiratory motion leads to blurring of the image [51], [171] which corresponds to spatial low-pass filtering and is therefore likely to reduce peak velocities.

A multipoint encoding scheme [58] was incorporated into the 5D Flow approach. Thereby the velocity vector field was encoded with different sensitivities to mean and fluctuating velocities to provide an accurate assessment of mean and turbulent velocities over a large dynamic range. The 7-point 5D flow LLR implementation yielded TKE maps as they can be expected for healthy, young volunteers, with moderate values of up to 300 J/m^2 and turbulence mainly occurring in the region of the flow jet in the proximal aorta. In comparison, TKE maps derived from the 4D Flow reference with 4-point encoding appeared noisy, due to only using a single encoding velocity of 150 cm/s. Moreover, the 4D Flow reference showed TKE values in the descending aorta which were as high as in the ascending aorta. This is considered unrealistic as transient/turbulent flow typically occurs in the region downstream of the aortic valve and not in the descending aorta in healthy, young volunteers.

The acquisition time for 7-point encoded 5D Flow was fixed to 4 minutes. For 10-point encoding, as it has been used when assessing stenotic valves [22], this would correspond to an acquisition time of ca. 6 minutes for 5D Flow, compared to $17.2 \pm 4.7 \text{ min}$ for accelerated 10-point 4D Flow acquisitions [22].

Image quality of data in inspiration as shown in Figure 7 was lower compared to data reconstructed in the end-expiratory motion state with 5D Flow LLR. This can be explained with inspiration taking a smaller fraction of the duration of the respiratory cycle than expiration. Moreover, the respiratory motion curve does not reach the maximum value in inspiration for every respiratory cycle, whereas it reaches an end-expiratory plateau in most cases. As respiratory motion states were defined to obtain similar acceleration factors in each motion state, this led to a wider range of motion in inspiratory states than in expiratory states.

The present work assessed mean and fluctuating velocity vector fields in healthy volunteers only. When applying the proposed 5D Flow method in patients with aortic stenosis, an extension to 10-point encoding [22] needs to be implemented for sufficient dynamic range. Adding 3 more points would lead to an increase in scan time by ca. 42% and can thus still easily be integrated into clinical workflows.

While the present study was focused on turbulence encoding, the proposed technique can be readily applied for the acquisition of standard 4D flow MRI data in the aorta and in the heart. For different

applications the scan time will change as a function of the size of the acquisition matrix, but respiratory motion is still expected to be accurately modelled as a low-rank problem. Therefore, fixing scan time independently of respiratory motion should still be feasible. Moreover, the suggested multipoint encoding approach provides improved accuracy for lower velocities, similar to other multi-VENC approaches [172], [173]. In addition, the protocol can be used to measure flow in different respiratory motion states to assess respiration dependent flow-patterns, e.g. the Fontan circulation [174], [175]. To obtain better results in inspiration, one might define bins with equal range of motion, thus leading to varying acceleration factors for different bins. In order to still obtain sufficient sampling rates in each motion state, one would therefore need to increase scan time beyond the current 4 min limit.

A limitation of the present study is the lack of a ground truth data. The 4D Flow reference data were acquired in a separate scan and consistency of flow conditions cannot be expected over the entire scan session. In addition, the 4D Flow reference data showed considerable respiratory-motion related artifacts in later cardiac phases since the pencil-beam navigator was played out right after R-wave detection and only once per cardiac cycle (acceptance rates varied between 42% and 72%). Accordingly, the quantitative comparisons with the 4D Flow data were limited to systole in order to avoid respiratory-motion corrupted cardiac phases as much as possible.

Finally, a drawback of both 5D Flow LLR and 5D Flow TV are considerably longer reconstruction times when compared to standard 4D Flow MRI (ca. 35 minutes for 5D LLR and ca. 60 min for 5D TV vs. ca. 3 min for conventional 4D Flow MRI on a workstation with two 14 Core Intel Xeon E5-2680 CPUs and 256 GB RAM). In the future, this relative disadvantage may be addressed by employing variational neural network based reconstructions and their deployment on dedicated hardware [110], [176].

5.5 Conclusion

Respiratory motion resolved multipoint 5D Flow MRI allows for breathing-pattern independent mapping of mean and turbulent velocities in 4 minutes. The reduction in scan time allows for

integration of the sequence into standard clinical workflows. Further in-vivo studies are now warranted to assess the performance of the method in relevant patient populations.

5.6 Acknowledgements

The authors thank Giuseppe Valvano for his valuable advice regarding low-rank modelling of 4D flow and Richard Droste for contributing to initial experiments.

Chapter 6 Comprehensive Turbulence Assessment with 5D flow Tensor MRI

Submitted as: J. Walheim, H. Dillinger, A. Gotschy, and S. Kozerke, “5D Flow Tensor MRI to Efficiently Map Reynolds Stresses of Aortic Blood Flow In-Vivo,” *Sci Rep*, under review

6.1 Introduction

Beyond quantifying TKE, all components of the Reynolds stress tensor (RST) may be obtained using appropriate changes of the MRI pulse sequence design [25], a concept that has been validated using simulation and simplified in-vitro experiments recently [19], [26]. Such an approach may offer improved mapping of pressure gradients across heart valves and stenotic vessel sections [19], [26], [29].

A key practical challenge to quantifying the RST in-vivo relates to the extended scan times required in order to encode velocity fluctuations along the minimum number of six non-collinear axes. In addition, the dynamic range of velocity fluctuations encountered in-vivo demands at least two measurements along each non-collinear axis [58], leading to scan times well beyond clinically acceptable limits.

The objective of the present work was to develop an approach to efficiently map the RST and hence turbulent shear stresses in-vivo within clinically acceptable scan times. Our approach is based upon recent advances in compressed sensing and sparse recovery of respiratory-motion resolved 4D Flow MRI data, which we have presented previously [177]. Here we propose a framework to efficiently quantify velocities and the RST using a highly undersampled acquisition scheme with locally low-rank image reconstruction [33], [98] and multipoint encoding per axis including Bayesian estimation of average velocity per voxel as well as intravoxel velocity standard deviations [58]. We term this approach 5D Flow Tensor MRI.

Using a total of 19 velocity encodings, 5D Flow Tensor MRI requires 10 min of scan time and hence enables data acquisition in a clinical setting. To demonstrate accuracy and precision of 5D Flow Tensor MRI, results of computer simulations based on previously collected in-vivo data and in-vitro particle tracking velocimetry of valvular flow are shown. In-vivo proof of concept of 5D Flow Tensor MRI is demonstrated on patients with a bio-prosthetic heart valve revealing elevated turbulent shear stresses and turbulent kinetic energy compared to healthy controls.

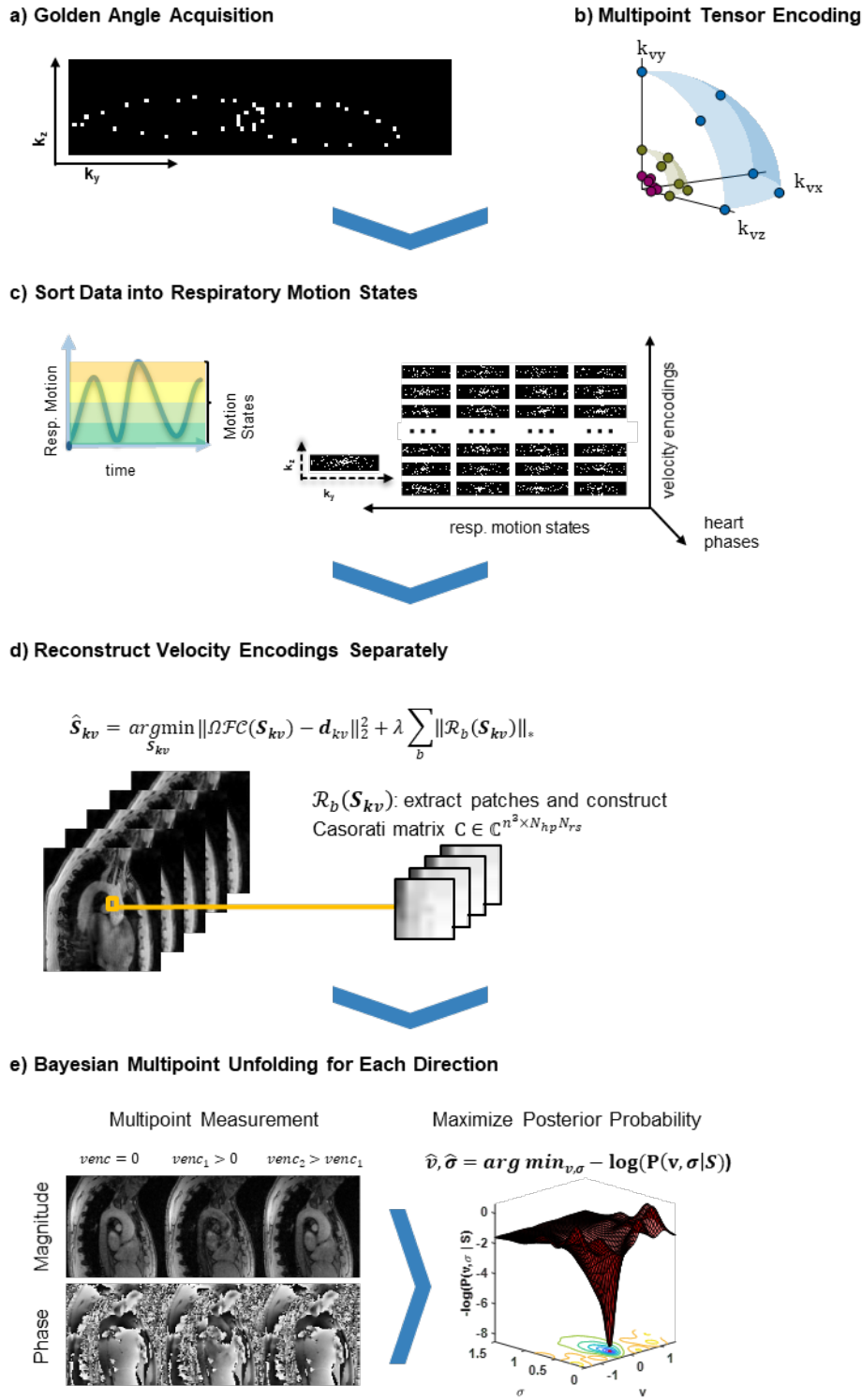


Figure 6.1: Illustration of in-vivo 5D Flow Tensor MRI: a) K-space data are continuously acquired on a Cartesian golden angle trajectory during free breathing of the subject. b) Velocities are encoded along six non-collinear directions with different velocity encodings VENC for improved accuracy of ISVD quantification over the desired range. c) Each readout is assigned to a discrete respiratory motion state and cardiac phase, leading to undersampling patterns as required by compressed sensing reconstructions. d) Images for each velocity encoding are reconstructed separately by exploiting correlations over cardiac and respiratory dimensions using a locally low-rank reconstruction. e) For each direction, the measurements with different VENCs are combined using a Bayesian approach which selects the most likely values \bar{v} and σ given the signal model S_{kv} and the measured data d_{kv} .

6.2 Results

MRI Data Acquisition and Reconstruction

Figure 6.1 illustrates the 5D Flow Tensor MRI concept including data acquisition, multipoint encoding, data reconstruction and Bayesian processing. Data are sparsely sampled using a Cartesian golden angle trajectory and retrospectively sorted into discrete respiratory motion states and cardiac phases [177]. Each velocity encoding is reconstructed separately using a locally low-rank reconstruction approach. Velocities are encoded in six non-collinear directions using three velocity encodings per axis to cover the range of turbulence intensity and mean velocities for patients and healthy controls.

Distributions of and Sensitivity to Intravoxel Standard Deviations

To make an appropriate choice of the number and strength of velocity encodings per spatial axis, the distribution of velocity intravoxel standard deviations (IVSD) [20] was compared based on retrospective 4D Flow MRI data of patients with moderate and severe aortic valve stenosis (N=28) and healthy controls (N=9) collected as part of a previous study [22]. As shown in Figure 6.2a, ISVD reaches up to 0.8 m/s in patients, while peak ISVD values of 0.3 m/s are measured in healthy controls. Since the MR signal magnitude is non-linearly related to IVSD, velocity encodings per axis need to be distributed in a non-equidistant manner. As illustrated in Figure 6.2c, a velocity encoding (VENC) of 0.5 m/s shows high sensitivity to IVSD in the healthy controls whereas a VENC of 1.50 m/s is optimal to probe IVSD in the aortic stenosis patients. Figure 6.2d illustrates the resulting uncertainty in IVSD quantification with noisy data. Using Monte-Carlo simulations, for each value of IVSD σ , 10^5 samples with additive white Gaussian noise were generated and mean and standard deviation of the IVSD estimates σ_{est} were determined. In case σ is too high or too low, σ_{est} decreases in accuracy. Moreover, values of σ for which the signal magnitude vanishes cannot be discerned and lead to a plateau in the plot. As can be seen, an encoding velocity of 0.5 m/s, which would cover the range of IVSD in healthy aortae, cannot discern elevated values in patients. To ensure an accurate estimate of IVSD over the entire observed range, a distributed encoding scheme with 0.5 m/s, 1.5 m/s and 4.5 m/s is proposed. The first two values cover the range of turbulence, whereas the latter value prevents aliasing in the mean velocity field.

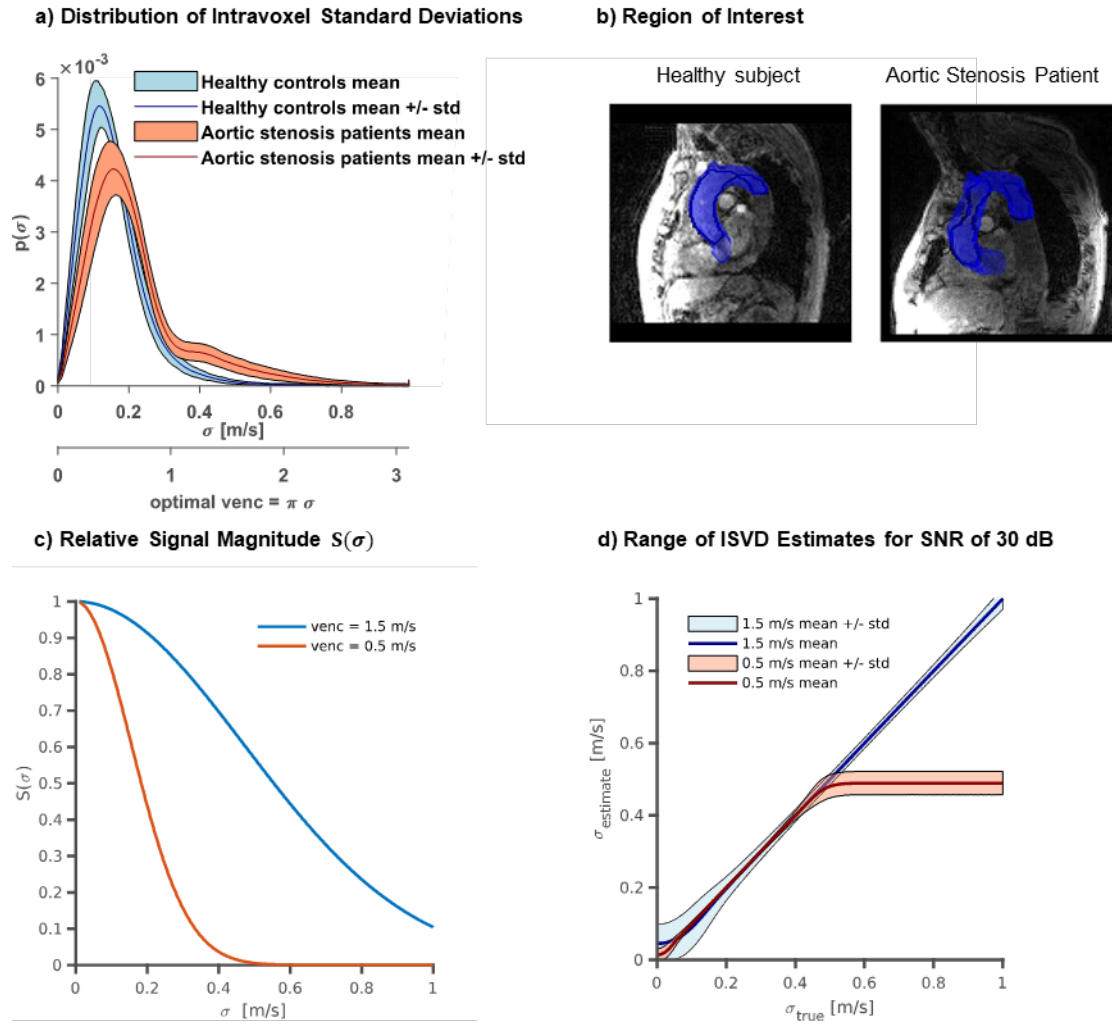


Figure 6.2: Exemplary distributions of IVSD in healthy and pathological aortae and illustration of IVSD encoding accuracy. a) For healthy volunteers, IVSD is distributed mainly between 0 m/s and 0.3 m/s. For patients, a wider distribution can be observed with values of IVSD up to 0.8 m/s. b) Examples of the region of interest for healthy controls and patients with aortic stenosis. c) IVSD leads to a reduction in signal magnitude which depends on the encoding velocity VENC. The signal shows a high sensitivity to changes in IVSD within a limited range. For low values, the magnitude changes little, whereas for high values the signal vanishes completely. d) Uncertainty of IVSD considering noisy data with an SNR of 30 dB. If IVSD is too high or too low, the IVSD estimates decrease in accuracy. Moreover, IVSDs for which the signal magnitude vanishes cannot be discerned and lead to a plateau in the plot.

Spatial Resolution and Signal-to-Noise Requirements

The effect of different signal-to-noise ratios (SNR) and the impact of image resolution on TKE and maximum principal turbulent shear stress (MPTSS) quantification was assessed using data previously acquired with particle tracking velocimetry (PTV) [165] as summarized in Figure 6.3. For low SNR, an increase in mean values is observed for MPTSS. For TKE, the average mean values remain stable for low values of SNR (1.7% increase at 20 dB) while an increase in standard deviation is observed for decreasing SNR (e.g. 6.8% increase at 20 dB). At an SNR of 30 dB, as estimated for the in-vivo scans, MPTSS is overestimated by 3.6% on average whereas TKE values show no relevant increase in mean

value (0.2%). Figure 6.3b shows the impact of different image resolutions for an SNR of 30 dB. Exemplary images show an increase of MPTSS and TKE at the jet core for increased voxel sizes. For large voxel sizes, the distribution of MPTSS values is skewed towards higher values with a corresponding increase in mean values and standard deviation. At a resolution of 2.5 mm, as used for the in vivo exams, MPTSS are overestimated by 15.9% on average. TKE distributions are also skewed towards higher values for large voxel sizes with an overestimation of 3.1% at 2.5 mm.

Accuracy and precision of TKE and MPTSS quantification were simulated in a Monte-Carlo simulation with 40 repetitions. Mean and standard deviation over the repetitions are provided in Table 1 for varying SNR at the highest resolution and Table 2 for different resolutions at an SNR of 30 dB respectively. Table 1 shows an increase in the random error for decreasing SNR. However, the random error on mean and standard deviation of the value distribution remains below 1% for all metrics. Table 2 shows the effect of increasing voxel sizes for a fixed SNR of 30 dB. For increasing voxel sizes, a systematic overestimation can be observed for all metrics. Moreover, mean and standard deviation of MPTSS and TKE distributions show a higher random error for increased voxel sizes.

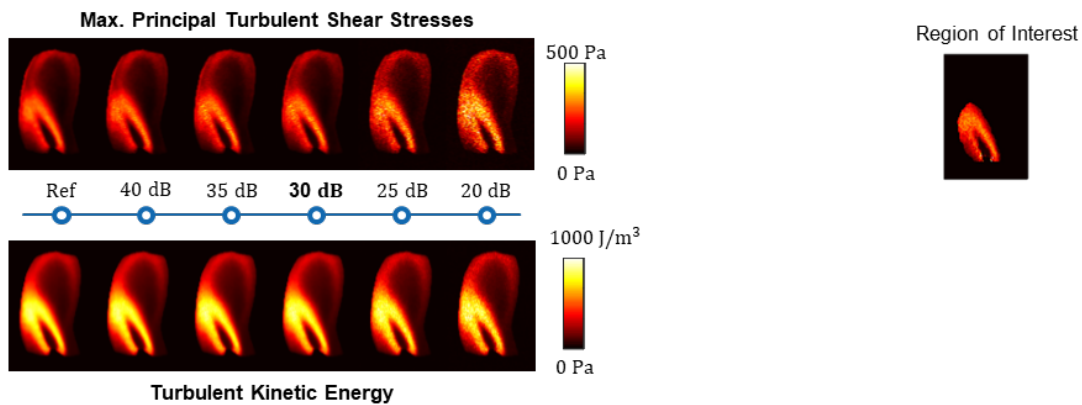
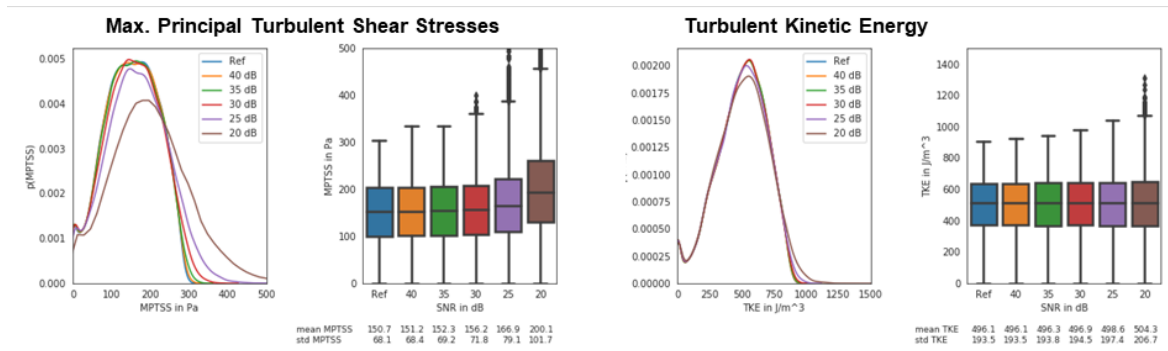
At 2.5 mm resolution and an SNR of 30 dB, TKE values show a mean of $511.8 \pm 1.4 \text{ J/m}^3$ and a standard deviation of $198.9 \pm 4.6 \text{ J/m}^3$ whereas MPTSS has a mean of $174.9 \pm 1.6 \text{ Pa}$ and a standard deviation of $110.7 \pm 10.0 \text{ Pa}$.

In-Vivo Measurements

Flow in the aorta of two patients with a bio-prosthetic aortic valve (65 yrs, female with a SJM Trifecta Aortic Valve TFGT-21A, 21 mm, and 80 years, female with an Edwards SAPIEN 3, 23 mm) and two healthy controls (26 yrs, female and 58 yrs, female) was acquired using the 5D Flow Tensor MRI approach on a clinical 1.5T MRI system (Philips Healthcare, Best, The Netherlands) and a 5-channel receive array.

Figure 6.4a shows exemplary results in a single slice for a patient and a healthy control (patient 65 yrs, female, and volunteer 26 yrs, female). The highest values of TKE and MPTSS can be seen downstream of the bio-prosthetic valve in the patient. Figure 6.4b shows value distributions of velocity magnitudes, TKE, and MPTSS in the ascending aorta during systole. Increased values of TKE and MPTSS in the patients relative to the controls were found. (For TKE, patients: $199.7 \pm 115.4 \text{ J/m}^3$ and $148.1 \pm 157.9 \text{ J/m}^3$ vs. volunteers: $47.8 \pm 32.1 \text{ J/m}^3$ and $76.0 \pm 32.8 \text{ J/m}^3$, and for MPTSS, patients: $161.3 \pm 158.3 \text{ Pa}$ and $102.1 \pm 146.0 \text{ Pa}$ vs. volunteers: $44.1 \pm 41.3 \text{ Pa}$ and $77.2 \pm 48.9 \text{ Pa}$). Mean velocities in the patients were $0.53 \pm 0.34 \text{ m/s}$ and $0.38 \pm 0.19 \text{ m/s}$ compared to $0.66 \pm 0.11 \text{ m/s}$ and $0.53 \pm 0.18 \text{ m/s}$ for the healthy controls.

a) Signal-To-Noise Ratio Dependency



b) Resolution Dependency for SNR = 30 dB

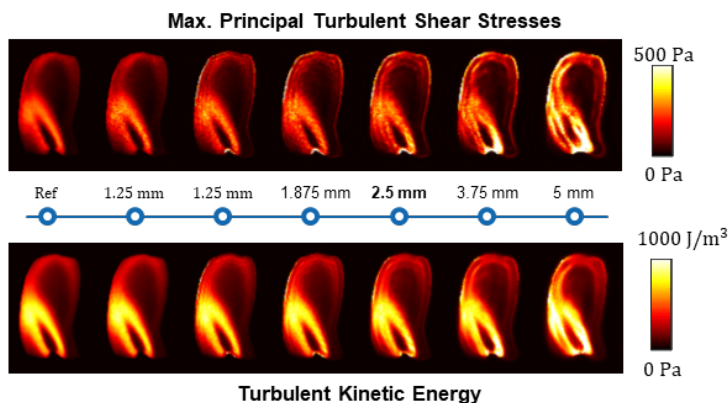
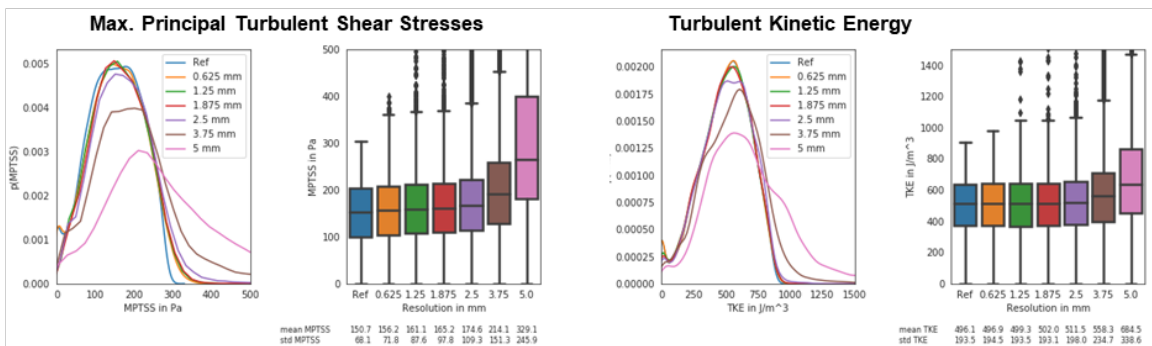


Figure 6.3: Impact of SNR and image resolution on quantification of TKE and MPTSS. a) Decreasing SNR leads to an overestimation of TKE and MPTSS. At an SNR of 30 dB, as estimated for in-vivo experiments, this overestimation is relatively low. b) Increasing voxel sizes lead to a skewed distribution of TKE and MPTSS. At a resolution of 2.5 mm, as used for in-vivo experiments, TKE is overestimated by 3.1% and MPTSS is overestimated by 15.9% on average.

Table 1: Accuracy and precision for a resolution of 0.625 mm and varying SNR obtained in a Monte Carlo type experiment with 40 repetitions. For lower SNRs a bias towards higher values is observed and accuracy deteriorates.

| SNR (Res = 0.625 mm) | TKE mean (mean ± std) | TKE std (mean ± std) | MPTSS mean (mean ± std) | MPTSS std (mean ± std) |
|---------------------------------------|---------------------------------|--------------------------------|-----------------------------------|----------------------------------|
| 40 dB | 496.2 ± 0.0 | 193.6 ± 0.0 | 151.2 ± 0.0 | 68.4 ± 0.0 |
| 35 dB | 496.4 ± 0.1 | 193.8 ± 0.1 | 152.4 ± 0.1 | 69.2 ± 0.1 |
| 30 dB | 496.9 ± 0.1 | 194.6 ± 0.1 | 156.0 ± 0.1 | 71.6 ± 0.1 |
| 25 dB | 498.6 ± 0.2 | 197.3 ± 0.2 | 167.0 ± 0.2 | 79.1 ± 0.2 |
| 20 dB | 504.1 ± 0.4 | 206.1 ± 0.3 | 199.8 ± 0.4 | 101.5 ± 0.5 |

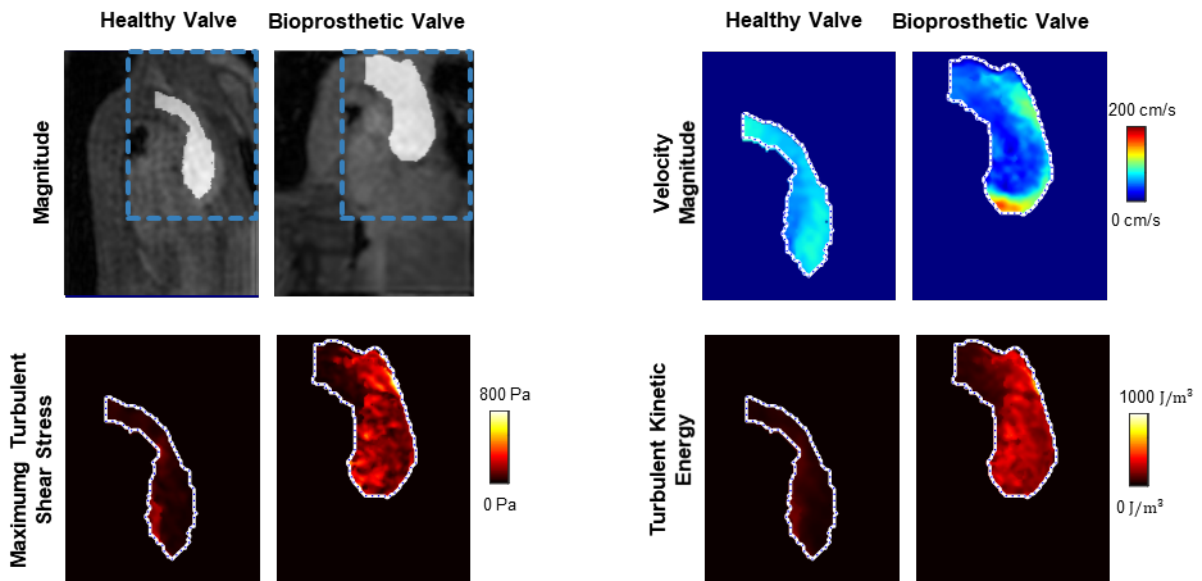
Table 2: Accuracy and precision for a SNR of 30 dB and varying resolution (voxel size) obtained in a Monte Carlo type experiment with 40 repetitions. Increasing voxel sizes lead to an overestimation of MPTSS and TKE. No clear trend can be observed for accuracy.

| Resolution (SNR = 30 dB) | TKE mean (mean ± std) | TKE std (mean ± std) | MPTSS mean (mean ± std) | MPTSS std (mean ± std) |
|---|---------------------------------|--------------------------------|-----------------------------------|----------------------------------|
| 0.625 mm | 496.9 ± 0.4 | 194.7 ± 0.1 | 156.0 ± 0.7 | 71.7 ± 0.2 |
| 1.25 mm | 499.4 ± 0.9 | 193.5 ± 2.6 | 161.2 ± 1.2 | 88.8 ± 6.6 |
| 1.875 mm | 502.3 ± 1.3 | 194.1 ± 4.4 | 165.4 ± 1.5 | 100.5 ± 9.7 |
| 2.5 mm | 511.8 ± 1.4 | 198.9 ± 4.6 | 174.9 ± 1.6 | 110.7 ± 10.0 |
| 3.75 mm | 558.7 ± 2.6 | 236.1 ± 10.3 | 214.5 ± 2.6 | 153.2 ± 16.4 |
| 5 mm | 684.6 ± 2.2 | 338.0 ± 3.6 | 328.9 ± 1.4 | 245.4 ± 3.7 |

6.3 Discussion

This study has demonstrated in-vivo turbulent flow assessment using 5D Flow Tensor MRI in clinically feasible scan times for the first time. A multi-point encoding scheme was employed to probe the mean and fluctuating velocity components using non-collinear encoding directions, similar to concepts used in diffusion tensor imaging [24]. The approach permits, besides the assessment of time-resolved mean velocity vector fields, the quantification of Reynolds stresses and hence turbulent kinetic energy and turbulent shear stresses in-vivo.

a) Exemplary Slices



b) Value Distributions in Ascending Aorta

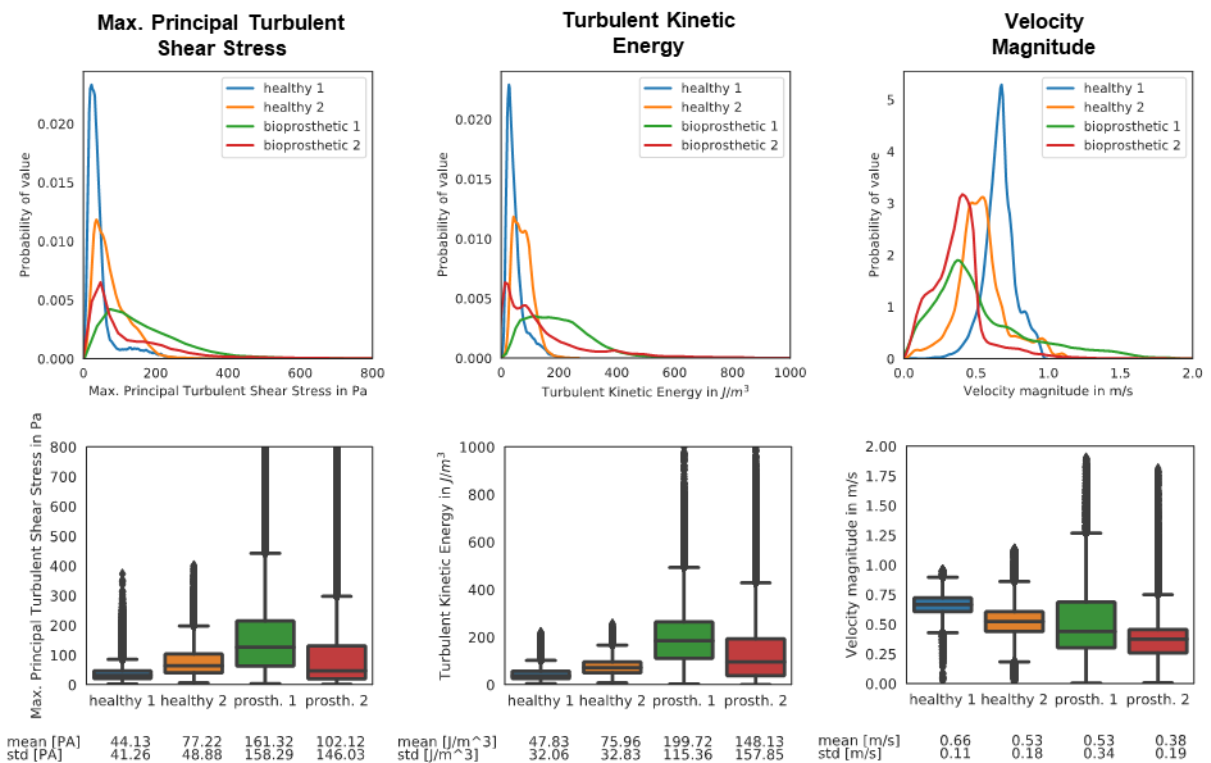


Figure 6.4: In-vivo assessment of turbulent flow through healthy and a bio-prosthetic heart valves. a) shows exemplary slices of a healthy and a bio-prosthetic heart valve. The flow field shows uniform distribution of velocity magnitudes throughout the proximal aorta for the healthy valve whereas a jet with high velocities can be observed for the bio-prosthetic valve. MPTSS and TKE are elevated downstream of the bio-prosthetic valve. Visual assessment shows highest MPTSS and TKE near the vessel wall for the healthy valve and elevated values throughout the proximal aorta for the bio-prosthetic valve. b) shows value distributions for the different metrics, with healthy 1 and bio-prosthetic 1 corresponding to the examples from a). MPTSS and TKE are elevated for the bio-prosthetic heart valves. Velocities are on average lower for the bio-prosthetic heart valve but are distributed over a larger value range

Distributions of IVSD in the aortae of healthy subjects and patients with aortic valve disease were analyzed to choose velocity encodings (Figure 6.2a,b). As illustrated in Figure 6.2c,d, the choice of velocity encoding has considerable impact on the accuracy of IVSD quantification. This makes the choice of an appropriate encoding velocity crucial, when using a single encoding velocity per axis as in conventional 4D Flow MRI. To probe IVSD with an increased dynamic range, encoding of the RST was combined with a multipoint scheme[58]. In the present study, encoding velocities of 0.5 m/s, 1.5 m/s and 4.5 m/s were selected. As indicated in Figure 6.2a, encoding velocities of 0.5 m/s and 1.5 m/s cover the expected range of IVSD. The additional velocity encoding at 4.5 m/s was used to avoid phase wraps in the reconstructed mean velocity fields. Of note, the particular choice of encoding velocities was made with respects to the range of observed IVSD, to prevent aliasing artifacts in the mean velocity fields, and to make echo times not too long. However, the encoding scheme yields further potential for optimization. In particular, the use of advanced phase unwrapping methods [178] might allow to leave out the highest VENC.

Simulation of the MRI acquisition and encoding process revealed an overestimation of TKE and MPTSS for large voxel sizes. The overestimation amounted to about 3.1% for TKE and to approximately 15.9% for MPTSS at the given acquisition resolution of 2.5 mm and at an estimated SNR of 30 dB. The impact of image resolution can be related to the assumption of Gaussian intra-voxel velocity distributions in the derivation of turbulence, which is not fulfilled for coarse image resolutions as shown in previous studies [128].

The impact of SNR on quantification of TKE and MPTSS was found to be relatively low compared to the impact of resolution. Starting at low SNR values below 25 dB, an overestimation of MPTSS was observed whereas TKE estimates were robust even at lower SNR values. SNR was estimated at ca. 30 dB in this study. In this range, noise played only a minor role in the assessment of TKE and MPTSS.

As shown in the Monte-Carlo simulation, the error in real-world experimental conditions is mostly due to a loss in accuracy for reduced image resolutions, whereas the random fluctuations for repeated experiments is comparatively low. However, increasing image resolution would lead to a decrease in SNR and noise would start to compromise the assessment of turbulent quantities. Therefore, rather than increasing acquisition resolution, efforts to mitigate the effect of large voxel sizes by e.g. data assimilation approaches [179] are considered potential future options.

The feasibility of 5D Flow Tensor MRI to quantify distributions of MPTSS and TKE in patients with a bio-prosthetic valve relative to healthy controls has successfully been demonstrated. Distributions of TKE and MPTSS revealed distinct differences, while differences in mean velocity magnitudes were partly overlapping (Figure 6.4b). In the healthy controls, the highest values of TKE and MPTSS were found near the vessel walls, which can be attributed to partial volume effects (there were also some

differences between the two volunteers which can be related to the difference in age [180]). In contrast, flow downstream of the prosthetic valves showed highest values of MPTSS and TKE in the proximal aorta, reaching values of up to 500 Pa and 600 J/m^3 , respectively. MPTSS values were found to be below the threshold of elevated risk of red blood cell damage which was estimated between ca. 600 Pa [181] and 800 Pa [182]. While mechanical heart valves have been associated with blood cell damage [183], modern bio-prosthetic valves typically do not lead to complications [184]. An increase in shear stresses without reaching a critical level was therefore expected. It should, however, be noted the implantation of bio-prosthetic valves is primarily indicated in the elderly population, while mechanical heart valves are preferred in younger patients. Accordingly, future work using 5D Flow Tensor MRI should include patients with mechanical heart valves to assess and compare TKE and MPTSS levels.

Of note, the fixed scan time of 10 minutes which was set for the in-vivo study was sufficient for all subjects examined in this study. However, in cases where patient geometry requires a much larger field of view, an increase in scan time might be required.

A limitation of the present study is that no ground truth data was available to assess the accuracy of the in-vivo scans. Accordingly, computer simulations were used to provide estimates of accuracy and precision. However, the simulations were based on PTV measurements with a resolution of 0.625 mm. Thus, the reference data were already subject to some discretization error and availability of higher resolution ground truth data might show an even higher overestimation of turbulence. Another practical drawback relates to the long data reconstruction times (ca. 1.5h to 2h on a workstation with two 14 Core Intel Xeon E5-2680 CPUs and 256 GB RAM) which implies that data evaluation can only be performed after the scan session. Currently ongoing work is addressing this inconvenience by using variational neural networks [110] which have already been shown to perform compressed sensing reconstruction of standard 4D Flow MRI data in less than a minute [185].

In conclusion, 5D Flow Tensor MRI provides comprehensive quantification of turbulent flow in clinically feasible scan times. Its ability to assess elevated TKE and MPTSS in-vivo has successfully been demonstrated. Efficient in-vivo turbulence quantification will contribute also to methods aiming at quantifying irreversible pressure loss downstream of heart valves and stenotic sections.

6.4 Methods

Measurement of Reynolds Stress Tensor

In general, flow velocity vectors can be decomposed into a time-averaged mean vector $\bar{\boldsymbol{v}}$ and fluctuating components \boldsymbol{v}' [186]:

$$\mathbf{v} = \bar{\mathbf{v}} + \mathbf{v}'. \quad (6.1)$$

In the one-dimensional case, assuming a Gaussian intra-voxel velocity distribution (IVSD) of variance σ^2 , the MR signal $S(k_v)$ reads [20]:

$$s(k_v) = s_0 e^{\frac{-\sigma^2 k_v^2}{2}} e^{-ik_v \bar{v}}. \quad (6.2)$$

where $k_v = \gamma \int_0^T tG(t)dt = \frac{\pi}{VENC}$ denotes the first gradient moment of bipolar velocity encoding gradient G applied during time T .

The relationship described in Equation 6.2 is non-linear and requires adjustment of the encoding strength according to the expected range of IVSD. By setting $\frac{\delta^2 s(k_v)}{\delta \sigma^2} = 0$, the optimal encoding strength for a given IVSD σ can be determined as $k_v = 1/\sigma$ or $VENC = \pi * \sigma$.

The three-dimensional statistical description of velocity fluctuations \mathbf{v}' includes variances and covariances as described by the RST (RST):

$$\mathbf{R} = \rho \begin{bmatrix} \overline{v'_x v'_x} & \overline{v'_x v'_y} & \overline{v'_x v'_z} \\ \overline{v'_y v'_x} & \overline{v'_y v'_y} & \overline{v'_y v'_z} \\ \overline{v'_z v'_x} & \overline{v'_z v'_y} & \overline{v'_z v'_z} \end{bmatrix} \quad (6.3)$$

with variances $\overline{v'_i v'_i}$, covariances $\overline{v'_i v'_j}$ and fluid density ρ . The magnitude of the complex-valued MR signal can be written as [25]:

$$|s(\mathbf{k}_v)| = |s_0| e^{-\frac{1}{2\rho} \mathbf{k}_v^T \mathbf{R} \mathbf{k}_v} \quad (6.4)$$

with $\mathbf{k}_v = [k_{vx}, k_{vy}, k_{vz}]^T$.

Analogous to diffusion tensor imaging [24], the RST can be determined by encoding along six non-collinear directions and solving a system of linear equations. For six measurements along six different velocity encodings and $\sigma_{k_{v,i}}^2 = \frac{2}{|k_{v,i}|^2} \ln \frac{|s(\mathbf{k}_v=0)|}{|s(\mathbf{k}_{v,i})|}$, the following set of equations is obtained:

$$\begin{aligned}
\begin{pmatrix} \sigma_{k_{v,1}}^2 \\ \vdots \\ \sigma_{k_{v,6}}^2 \end{pmatrix} &= \begin{pmatrix} (k_{vx,1}^2 & k_{vy,1}^2 & k_{vz,1}^2 & 2k_{vx,1}k_{vy,1} & 2k_{vx,1}k_{vz,1} & 2k_{vy,1}k_{vz,1}) \\ & & & |\mathbf{k}_{v,1}|^2 & & \\ & & & \dots & & \\ & & & \dots & & \\ & & & \dots & & \\ (k_{vx,6}^2 & k_{vy,6}^2 & k_{vz,6}^2 & 2k_{vx,6}k_{vy,6} & 2k_{vx,6}k_{vz,6} & 2k_{vy,6}k_{vz,6}) \\ & & & |\mathbf{k}_{v,6}|^2 & & \end{pmatrix} \begin{pmatrix} \overline{v'_x v'_x} \\ \overline{v'_y v'_y} \\ \overline{v'_z v'_z} \\ \overline{v'_x v'_y} \\ \overline{v'_x v'_z} \\ \overline{v'_y v'_z} \end{pmatrix} \\
&= \mathbf{H} \begin{pmatrix} \overline{v'_x v'_x} \\ \overline{v'_y v'_y} \\ \overline{v'_z v'_z} \\ \overline{v'_x v'_y} \\ \overline{v'_x v'_z} \\ \overline{v'_y v'_z} \end{pmatrix}.
\end{aligned} \tag{6.5}$$

Accordingly, the elements of the RST can be calculated voxel-wise using the pseudoinverse:

$$\begin{pmatrix} \overline{v'_x v'_x} \\ \overline{v'_y v'_y} \\ \overline{v'_z v'_z} \\ \overline{v'_x v'_y} \\ \overline{v'_x v'_z} \\ \overline{v'_y v'_z} \end{pmatrix} = (\mathbf{H}^T \mathbf{H})^{-1} \mathbf{H} \begin{pmatrix} \sigma_{k_{v,1}}^2 \\ \vdots \\ \sigma_{k_{v,6}}^2 \end{pmatrix}. \tag{6.6}$$

In this study, matrix \mathbf{H} was designed according to:

$$\mathbf{H} = \begin{pmatrix} 1 & 0 & 0 \\ 0 & 1 & 0 \\ 0 & 0 & 1 \\ 1/\sqrt{2} & 1/\sqrt{2} & 0 \\ 1/\sqrt{2} & 0 & 1/\sqrt{2} \\ 0 & 1/\sqrt{2} & 1/\sqrt{2} \end{pmatrix}. \tag{6.7}$$

To mitigate the effect of non-linear encoding of the ISVD, a multipoint approach [58] was used to probe the velocity field at different encoding strengths. Figure 6.1b illustrates the velocity encoding which encodes velocities in three orthogonal directions and their combinations along the diagonals with different encoding strengths. For each direction the different encoding velocities were combined with Bayesian multipoint unfolding [58] as illustrated in Figure 6.1e.

Measurement of Mean Velocities

Redundant encoding schemes provide additional information for estimation of mean velocities [47]. Denoting the velocities encoded in n different directions by $\tilde{\mathbf{V}} = (\mathbf{v}_1, \dots, \mathbf{v}_n)^T$ with corresponding velocity encodings $\{\mathbf{k}_{v,1}, \dots, \mathbf{k}_{v,n}\}$, the velocities in the Cartesian coordinate system $\mathbf{V}_{cart} = \text{diag}(v_x, v_y, v_z)$ can be written as:

$$\tilde{\mathbf{V}} = \begin{pmatrix} \mathbf{k}_{v1}/|\mathbf{k}_{v1}| \\ \dots \\ \mathbf{k}_{vn}/|\mathbf{k}_{vn}| \end{pmatrix} \mathbf{V}_{cart} = \mathbf{A} \mathbf{V}_{cart} \quad (6.8)$$

A solution to this overdetermined system of linear equations is provided by the pseudo-inverse:

$$\begin{pmatrix} v_x & 0 & 0 \\ 0 & v_y & 0 \\ 0 & 0 & v_z \end{pmatrix} = \mathbf{V}_{cart} = (\mathbf{A}^T \mathbf{A})^{-1} \mathbf{A}^T \tilde{\mathbf{V}}. \quad (6.9)$$

Value Range of Intravoxel Standard Deviations

Datasets previously obtained in 9 healthy volunteers and 28 patients with aortic valve stenosis [22] were retrospectively analyzed to determine the range of IVSD occurring in the ascending aorta (Figure 6.2b shows exemplary slices with the corresponding region of interest). The data were acquired and reconstructed with multipoint acquisition and Bayesian reconstruction [58]. Values of VENC were 4.50, 1.50, and 0.50 m/s for patients and 2.00, 0.67, and 0.40 m/s for the healthy control group.

The ascending aorta was segmented manually. To assess the distribution of the ISVD for the two groups, the relative probability $p(\sigma)$ of different values of IVSD in the segmented region was calculated for each subject and the mean and standard deviation of $p(\sigma)$ were determined over the patient cohort and the healthy control group respectively.

Spatial Resolution and Signal-to-Noise Requirements

MRI acquisitions with varying SNR and image resolution were simulated based on flow through a 64% stenosis measured with particle tracking velocimetry (PTV). Details on acquisition and processing of the PTV data can be found in [128], [187]. The dynamic and kinematic viscosity were 5.82×10^{-3} Pa and 4.85×10^{-6} m²/s, respectively, and the fluid density 1200 kg/m³. The velocity-to-noise ratio was determined to be larger than 10³. The PTV data were mapped onto a voxel size of 0.625×0.625×0.625 mm³.

Based on the PTV data, the MRI signal was calculated according to Equation 6.4. Encoding velocities were 0.5, 1.5, and 4.5 m/s. To limit the effect of artifacts in the numerical study a median filter of size 3 was applied to the components of the RST.

To assess acquisition with different voxel sizes, the signal was transformed to k-space and sampled using a window function with a bandwidth inversely proportional to the desired downsampling rate. Complex-valued white Gaussian noise of different strength was added to the data. For quantitative evaluations the ascending aorta was manually segmented using ITK-SNAP [188].

Complex-valued white Gaussian noise of different strength was added to the data to obtain the desired SNR

$$\text{SNR} = 20 \log \left(\frac{\text{Signal}}{\text{SD}(\text{Noise})} \right) \quad (6.10)$$

which was calculated over all velocity encodings.

In-Vivo Measurements

In-vivo assessment of the RST was performed in a patient with a bio-prosthetic aortic valve and a healthy control on 1.5T MR system (Philips Healthcare, Best, The Netherlands). The study was approved by the Ethics Committee of the Canton of Zurich, Switzerland, and all subjects provided written informed consent.

Data were acquired using a cardiac- and respiratory-motion resolved Cartesian tiny golden angle acquisition scheme [63], [161] including the necessary velocity encodings for RST measurements. Acquisition and reconstruction of the data is illustrated in Figure 6.1. During image reconstruction, data were sorted into four discrete respiratory motion bins. View sharing [163], [164] among respiratory motion states was used to ensure a minimum acceleration factor of 35 for each frame. Scan parameters were: voxel size of 2.5 mm x 2.5 mm x 2.5 mm, 25 cardiac phases, multipoint flow tensor encoding with VENCs of 0.5 m/s, 1.5 m/s, and 4.5 m/s, TE/TR = 3.9 ms/ 6.0 ms and scan duration of 10 minutes compared to 71 minutes for a fully sampled scan (which could increase by a factor of ca. 2 when using respiratory navigator gating).

Prior to reconstruction, noise pre-whitening was performed based on noise statistics from a separate scan acquired without radio-frequency excitation. Data for each velocity encoding strength and direction were reconstructed separately with BART [167], enforcing a locally low-rank model [33], [98] along cardiac phases and respiratory motion states [177]. The signal estimate $\hat{\mathbf{S}}_{kv}$ is thus obtained by iterative minimization of the cost term

$$\hat{\mathbf{s}}_{kv} = \underset{\mathbf{s}_{kv}}{\text{argmin}} \|\Omega \mathcal{F} \mathcal{C}(\mathbf{s}_{kv}) - \mathbf{d}_{kv}\|_2^2 + \lambda \sum_b \|\mathcal{R}_b(\mathbf{s}_{kv})\|_* \quad (6.11)$$

with the undersampling operator Ω , Fourier transform \mathcal{F} , coil sensitivity mapping \mathcal{C} and k-space data \mathbf{d}_{kv} . The operator \mathcal{R}_b selects the b -th out of N_b blocks of size of size $n_x \times n_y \times n_z = 22 \times 22 \times 22$ in the image from all N_{hp} heart phases and N_{rs} respiratory motion states and transforms them into a Casorati matrix with dimensions $n_x n_y n_z \times N_{hp} N_{rs}$. The reconstruction favors solutions for which this local Casorati matrix is low-ranked by penalizing its nuclear norm. The regularization weight λ was set to $\lambda = 0.005$. Both, block size and regularization weight were tuned for best agreement of magnitude images of the healthy control with a fully sampled reference measurement.

Following image reconstruction, only data in the expiratory motion state were considered for further processing. SNR in the measured data was determined using the pseudo-replica method[189] with 40 repetitions averaged over the ascending aorta and over the velocity encodings. Of note, approximate linearity is assumed with locally low-rank reconstructions. Accordingly, using Gaussian distribution of noise, the pseudo-replica method was considered the best approximation for SNR assessment.

Data Analysis

Turbulent Kinetic Energy (TKE) in $[J/m^3]$ was calculated from the main diagonal of the RST as:

$$TKE = \frac{\rho}{2} (\overline{v'_x v'_x} + \overline{v'_y v'_y} + \overline{v'_z v'_z}). \quad (6.12)$$

Principal stress analysis was performed and the maximum principal turbulent shear stress (MPTSS) was calculated from the eigenvalues $\delta_1 > \delta_2 > \delta_3$ of the RST as:

$$\tau_{max} = 0.5(\delta_1 - \delta_3) \quad (6.13)$$

assuming a density of blood of $\rho = 1060 \text{ kg}/m^3$.

For quantitative evaluations of in-vivo data the ascending aorta was manually segmented using ITK-SNAP[188] and for the simulated data, the flow jet in was masked.

Statistical analysis

Value-distributions of TKE, MPTSS, and velocity magnitude were investigated using a Gaussian kernel density estimate[190], [191]. Moreover, mean and standard deviations of the distributions were assessed.

Accuracy and precision of TKE and MPTSS quantification were assessed in a Monte-Carlo simulation with 40 repetitions and mean and standard deviation over the experiment repetitions were determined.

6.5 Acknowledgements

The authors thank Dr. Christian Stoeck for his support in conducting the patient scan, Dr. Gérard Crelier from Gyrotools LLC for his support in developing the 5D Flow Tensor pulse sequence, and Dr. Christian Binter for providing the PTV data used for simulations.

Chapter 7 A Deep Variational Network for Rapid 4D Flow MRI Reconstruction

Submitted as: V. Vishnevskiy, J. Walheim, and S. Kozerke, “Deep Variational Network for Rapid 4D Flow MRI Reconstruction,” *Nature Machine Intelligence*, 2019.

7.1 Introduction

Many efforts have been dedicated to accelerate flow acquisition by exploiting redundancies in the data. Partial Fourier imaging [30] has been used for moderate acceleration [130], but the underlying assumption of a slowly varying phase has been shown to be incorrect for 4D flow MRI [192]. Parallel imaging (PI) [38], which exploits the spatially varying sensitivity of receiver elements in the coil array has become a standard for accelerated imaging, but undersampling rates are limited by SNR amplification [70]. The advent of compressed sensing (CS) [32] has enabled very high acceleration in 4D flow MRI by acquiring only a subset of k-space data and exploiting prior information about data regularities during reconstruction [34], [97], [177], [180], [193], [194], with typical acceleration rates ranging from 5 [50] up to 27 [194]. In particular, the locally low rank (LLR) regularized reconstruction [33] has been a successful technique, which iteratively balances the data fidelity cost and the singular norm of a patch matrix stacked over cardiac phases (see Methods for details). However, iterative reconstruction methods used in CS increase reconstruction times considerably, implying that evaluation of 4D flow MRI data will typically happen when the subject has already been moved out of the scanner.

In recent years, deep neural networks have gained increasing popularity in MR image reconstruction. In the training stage, the neural network learns abstract features from a set of scans. After training, newly acquired data are reconstructed with very little computational effort by inference with the learned weights. This reduction in reconstruction times can facilitate the use of accelerated imaging methods in clinical practice. Moreover, reconstruction results can be superior to traditional CS methods [110], [111]. Some approaches discard concepts of iterative image reconstruction altogether, e.g. by learning end-to-end mappings from k-space to image space [114]. As a downside, such networks usually require abundant amounts of high quality training data which is not available for high-dimensional flow MRI. Model-based neural reconstruction networks can also be designed to replicate the behaviour of an iterative reconstruction by interlacing nonlinear convolutional filters with an operation that enforces closeness of the current image estimate to the acquired data [110], [111], [119], [195] similar to the data fidelity step in an iterative shrinkage-thresholding algorithm [77]. A recent study [118] showed that neural network architectures which incorporate such an operation

generalize better to different undersampling rates. In contrast, generic architectures which are solely based on convolutional layers can even deteriorate when the undersampling rate is reduced, although one would expect the reconstruction result to improve when more information is available.

In this work, an approach based on the idea of deep variational neural networks [110] is implemented for rapid 4D flow reconstruction. In this study we refer to the original variational network (VN) from [110] as HamVN. The network architecture replicates 10 steps of an iterative image reconstruction, while allowing for learnable spatio-temporal filter kernels, activation functions, and regularization weights at each iteration. In short, the proposed FlowVN improves HamVN in the following ways: (i) filtering is conducted on 4D data in an efficient way, (ii) the network is conditioned on the sampling rate, (iii) exponential weighting of intermediate layers is used as the regularization, (iv) real and imaginary parts of the signal filtered by shared weights, (v) momentum is considered during gradient descent unrolling, (vi) the data term allows nonlinear activation. The network is trained for a wide range of acceleration rates by allowing acceleration dependent weighting of data consistency and filtering steps. It is demonstrated that based on training performed with retrospectively undersampled data of healthy subjects, the network can accurately reconstruct pathological flow in a stenotic aorta in approximately 20 seconds. Moreover, an imaging study with 7 healthy subjects demonstrates good agreement of reconstructions from prospective undersampling with a reference measurement based on PI.

As illustrated in Figure 7.1a for each velocity encoding direction, the k-space data is acquired using a Cartesian golden angle sampling strategy, yielding variable density undersampling patterns in k-space. The signal from acquisition coils is compressed into 5 virtual coils via clustering [196]. The samples are then sorted into respiratory bins and data in the end-expiratory bin is used for reconstruction.

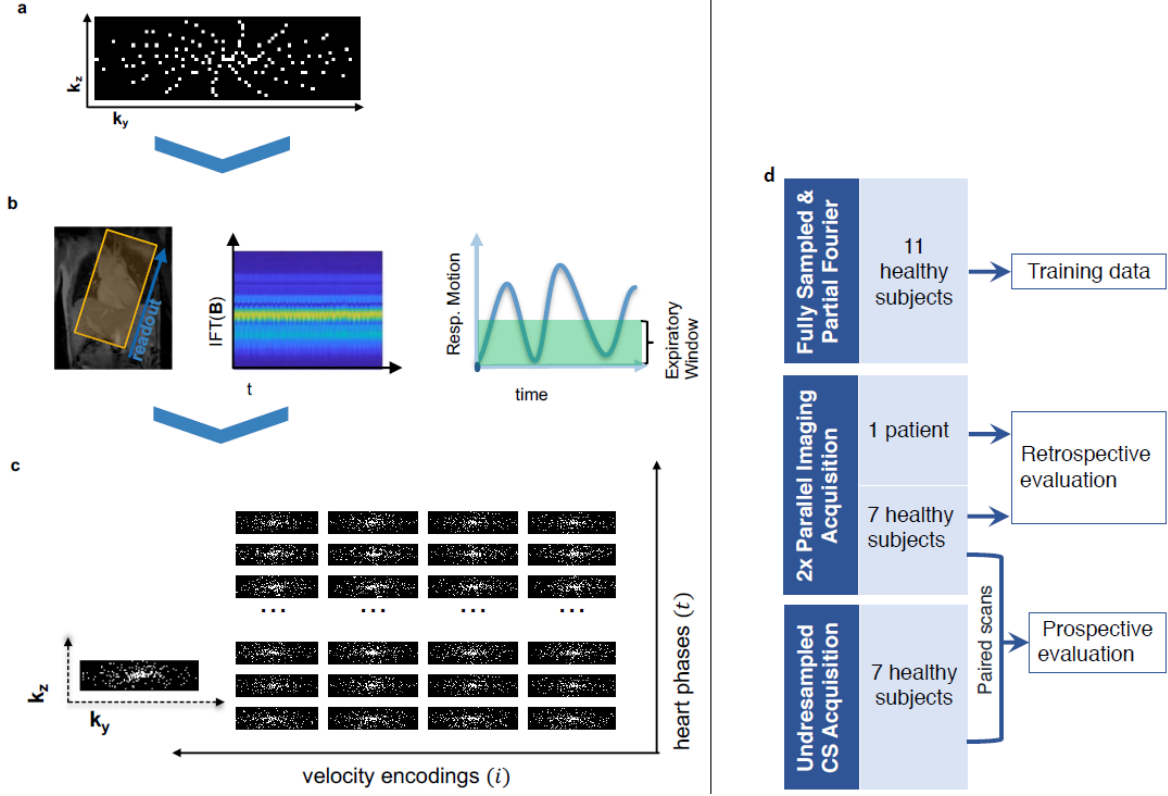


Figure 7.1: Breathing resolved 4D flow data acquisition. *a)* Data are sampled using a Cartesian pseudo-radial tiny Golden angle sampling pattern. *b)* Respiratory motion is binned to end expiration using a combination of principal component analysis, low-pass filtering, and coil-clustering. *c)* Acquired data are sorted according to heart phase and velocity encoding. *d)* Datasets used during training and evaluation.

7.2 FlowVN

A deep variational network can be seen as a differentiable sequence of an unrolled numerical optimization scheme. To enable learning, such a sequence is then relaxed by allowing tunable filter weights and activation functions. As described in Methods, we unroll $K = 10$ steps of a gradient descent with momentum governed by a scalar $\alpha(k)$:

$$\mathbf{u}^{(k+1)} \leftarrow \alpha^{(k+1)} \mathbf{u}^{(k)} + \mathbf{g}^{(k)} \quad (7.1)$$

$$\mathbf{s}^{(k+1)} \leftarrow \mathbf{s}^{(k)} - \mathbf{u}^{(k+1)} \quad (7.2)$$

At each k -th layer $\mathbf{s}^{(k)}$ represents the current complex-valued spatiotemporal image estimate, while $\mathbf{u}^{(k)}$ contains a running average of update steps. The update step $\mathbf{g}^{(k)}$ consists of data consistency and regularization terms (see Methods and Supplementary Algorithm S7.1 for details), that are weighted according to the sampling rate via tunable activation functions $\varphi_{ud}^{(k)}$ and $\varphi_{ur}^{(k)}$, respectively. The data consistency term modulates the k-space data residual via an activation function and maps it back to

the image space via a conjugate imaging operator. The regularization term at each layer contains 3D filters grouped into 4 banks, where each bank performs convolutions in 3 dedicated dimensions, namely xyz , xyt , xzt and yzt , therefore avoiding costly 4D convolutions. To avoid overfitting, we assume shared filters and activation functions that operate on real and imaginary components of the image. Note that both data and regularization terms do not assume correlations between real and imaginary parts of the signal, as highlighted in Figure 7.2b.

The image estimate $\mathbf{s}^{(k)}(\mathbf{d}, \boldsymbol{\theta})$ of the final layer can be then seen as a function of the k-space samples \mathbf{d} and network parameters $\boldsymbol{\theta}$. To tune the network parameters $\boldsymbol{\theta}$ we minimize the layer-wise exponentially weighted l_1 image reconstruction loss:

$$\underset{\boldsymbol{\theta}}{\operatorname{argmin}} \mathbb{E}_{\{\mathbf{d}, \mathbf{s}^*\} \sim \mathcal{T}} \sum_{k=1}^K e^{-\tau(K-k)} \|\mathbf{s}^{(k)}(\mathbf{d}; \boldsymbol{\theta}) - \mathbf{s}^*\| \quad (7.3)$$

over the retrospectively undersampled training dataset \mathcal{T} , where \mathbf{s}^* is the ground truth image. Layer weighting is controlled by parameter $\tau \geq 0$: when $\tau \approx 0$ the reconstruction error is penalized equally across layers, therefore gradients of network parameters have lower variance during stochastic optimization, yielding faster convergence. On the contrary, when $\tau \rightarrow +\infty$, only the reconstruction error at the final layer $\mathbf{s}^{(K)}$ is minimized, which improves fitting accuracy on the training data. It is worth mentioning that τ controls the trade-off between training reconstruction residual and network regularity. Similarly to Landweber iterations [110], [197] and deep supervision [198], such implicit regularization penalizes irregular representations at intermediate layers and favors networks that can provide a reconstruction as soon as possible. We propose to initialize τ with zero and then gradually increase it according to the training schedule (see Methods).

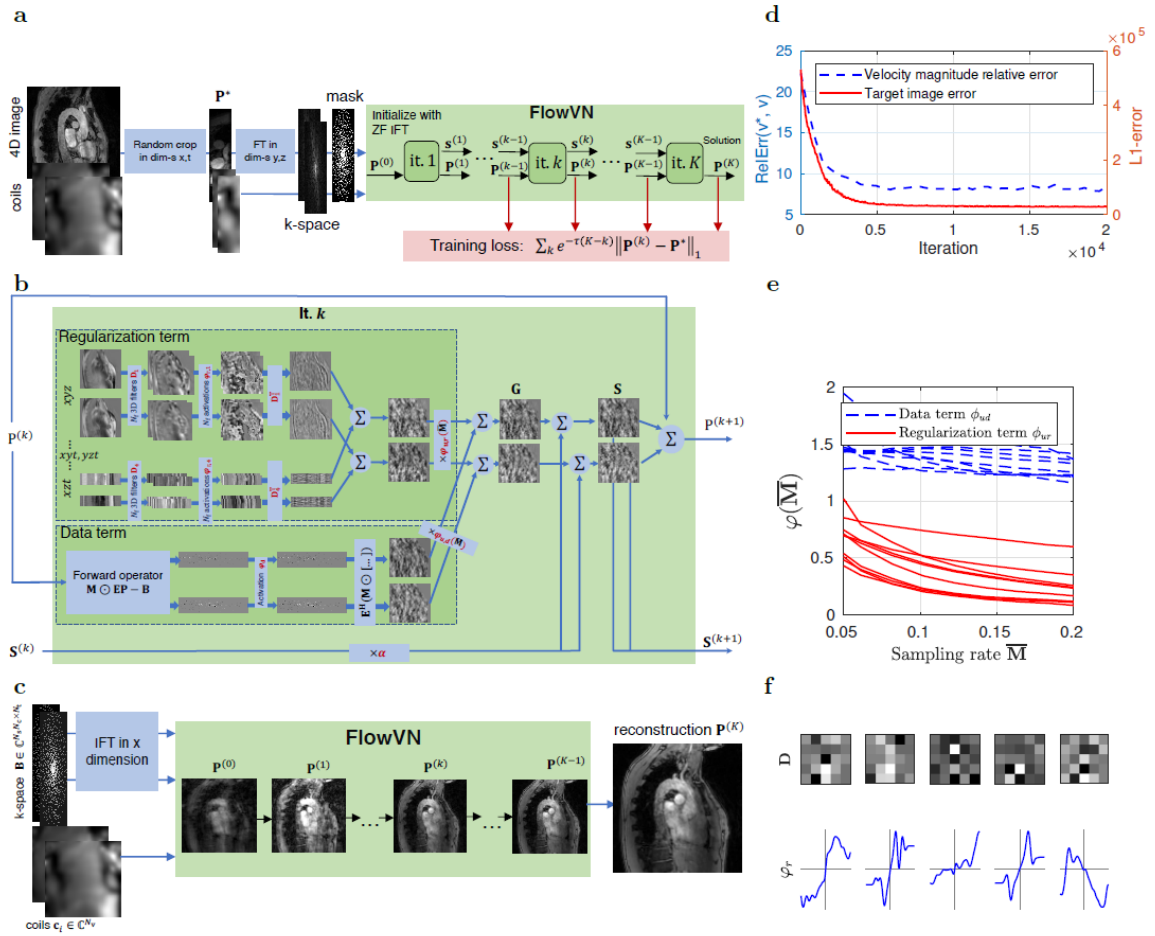


Figure 7.2: FlowVN architecture and training. a) Structure of FlowVN and its training strategy on reduced field-of-view. b) Single unrolled iteration block. c) FlowVN at inference time yields 4D image reconstruction. d) Target training image error and velocity magnitude error in aorta. e) Data and gradient term weighting functions shown for each of 10 layers. f) Exemplary slices of 3D xyz filters and their corresponding activation functions at layer 5.

7.3 Results

FlowVN Training

To demonstrate validity of our approach, we notice that the extracted velocity magnitude error in the aorta decreases simultaneously with the target reconstruction error, as shown in Figure 7.2d, therefore indicating that the FlowVN does not overfit to the training objective. It can be seen from Figure 7.2e that the regularization term is suppressed for lower acceleration rates R (higher sampling rate \bar{M}). A subset of learned FlowVN parameters θ is shown in Figure 7.2f, illustrating that learned convolutions perform direction-dependent filtering.

Retrospective Undersampling

Figure 7.3 illustrates reconstructed image magnitudes (for a single velocity encoding component), estimated velocity magnitudes and their errors on a healthy volunteer for acceleration factor $R = 14$. Compared to CS-LLR and HamVN, the proposed FlowVN provides better reconstruction accuracy in terms of image magnitude and velocities. Scatter plot and correlation analysis further suggest that the velocity magnitude image estimated via FlowVN is in better agreement with the ground truth. As shown in Supplementary Table S7.1 these observations extend to other acceleration factors $R \in \{6, \dots, 22\}$ as tested on 7 healthy volunteers.

Figure 7.4 indicates that FlowVN can accurately reconstruct the jet at the inlet section of the aorta for a patient with a pathological aortic valve.

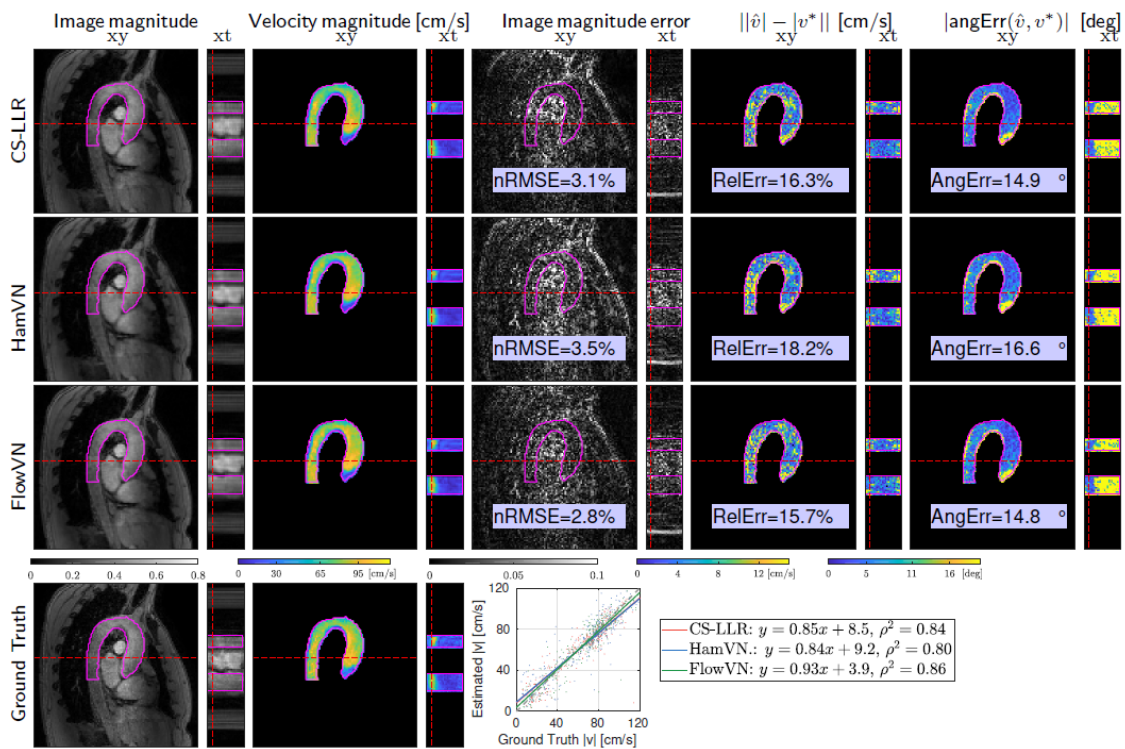


Figure 7.3: Reconstruction results on retrospectively undersampled data. Image magnitudes and estimated 4D velocity magnitude maps on retrospectively 14 \times undersampled data from a healthy volunteer. Corresponding slice locations are illustrated with red dashed lines, indicating cross-section of aorta and systolic peak. Scatter plot of velocity magnitude over manually segmented aorta (contour shown in magenta) is given together with correlation analysis ($y = ax + b$).

| Method | Recon. Time | # of Param |
|--------|-------------|------------|
| CS-LLR | 10 min 24 s | 2 |
| FlowVN | 21 s | 63'583 |

Table 7.1: Model complexities and typical reconstruction time for 4D flow reconstruction. Typical reconstruction time for 4-point velocity encoded data compressed to 5 virtual coils and reconstructed on a 113 \times 113 \times 25 grid. CS-LLR was executed on a 6-core Intel CPU, FlowVN was implemented in Tensorflow and evaluated on NVIDIA Titan RTX.

Prospective Undersampling

As shown in Figure 7.5a,b, peak velocities and peak flow estimated using CS-LLR and FlowVN are in good agreement with PI reconstruction, while HamVN systematically underestimates velocity magnitudes. Moreover, correlation analysis in Figure 7.5d shows high correlation between CS-LLR and FlowVN velocity estimates. In contrast, HamVN shows systematic velocity underestimation, compared to LLR.

The exemplary reconstruction time for typical 4-point velocity encoded images reported in Table 7.1 shows that the proposed FlowVN is 30 times faster than CS-LLR reconstruction.

7.4 Discussion

Practical learning-based image reconstruction can be traced back to dictionary learning methods [106], [108], where prior information is learned from image patches and then used as a sparsity-inducing regularizer for iterative reconstruction. Such an approach yields orders of magnitude longer reconstruction times, compared to modern deep learning approaches [110]. Early deep networks attempted to learn reconstruction as a regression from k-space [114] or zero-filled reconstructions [199] directly into the image space. Although tempting, such an approach might be unjustified, because the k-space and zero-filling artefacts have global dependence on image intensities. The advent of effective automatic differentiation systems [200], [201] revitalized the idea of unrolling [202] and relaxing numerical schemes that can solve the original reconstruction problem. Following this approach, a number of deep neural network architectures were proposed [110], [115], [119], [203] that disentangle image acquisition and image prior models. Unrolling gradient descent reconstruction with tunable filters and activation functions yields the HamVN architecture proposed by Hammernik et al. [110]. One advantage of a VN is that, compared to other deep architectures, it employs a relatively limited number of free parameters to tune, therefore it is less susceptible to overfitting.

In this work we further develop the VN architecture [110], [176], [204] to accommodate high performance undersampled 4D flow reconstruction with limited training. Namely, we avoid exponential model complexity growth by avoiding 4D convolutions and by using separable 3D convolutions that are shared for real and imaginary parts of the image. Furthermore, in contrast to the original HamVN [110], we train our FlowVN for a wide range of undersampling rates by allowing the regularization term to depend on it. As illustrated in Figure 7.2e, regularization scaled by φ_{ud} decreases as more samples are available, while the data term φ_{ud} stays constant for most of the layers. Such conditioning allows network training on a larger variety of artifacts. This is necessary in practice,

since for a given fixed acquisition time, the precise value of the undersampling rate is not known a priori and depends on breathing and cardiac motion patterns. We hypothesize that the wide range of acceleration factors that were used simultaneously to train the FlowVN provided a diverse collection of aliasing artefacts and enabled robust learning on a remarkably limited training set of 11 subjects. The exponential weighting of layer-wise reconstruction loss (Equation 7.3) further regularized FlowVN parameters by penalizing the nonlinear behavior presented in HamVN reconstructions.

The proposed FlowVN is a learning-based approach for undersampled 4D flow MRI reconstruction in under a minute. For fixed reconstruction accuracy FlowVN enables higher acceleration factors (30% improvement compared to CS-LLR image nRMSE at $R = 12$) and does not introduce significant bias to the peak flow estimates. The proposed reconstruction is 30 times faster than state-of-the art CS-LLR. It is worth noting that the FlowVN demonstrates high generalization ability, being able to preserve patient pathologies that were not present in the training data.

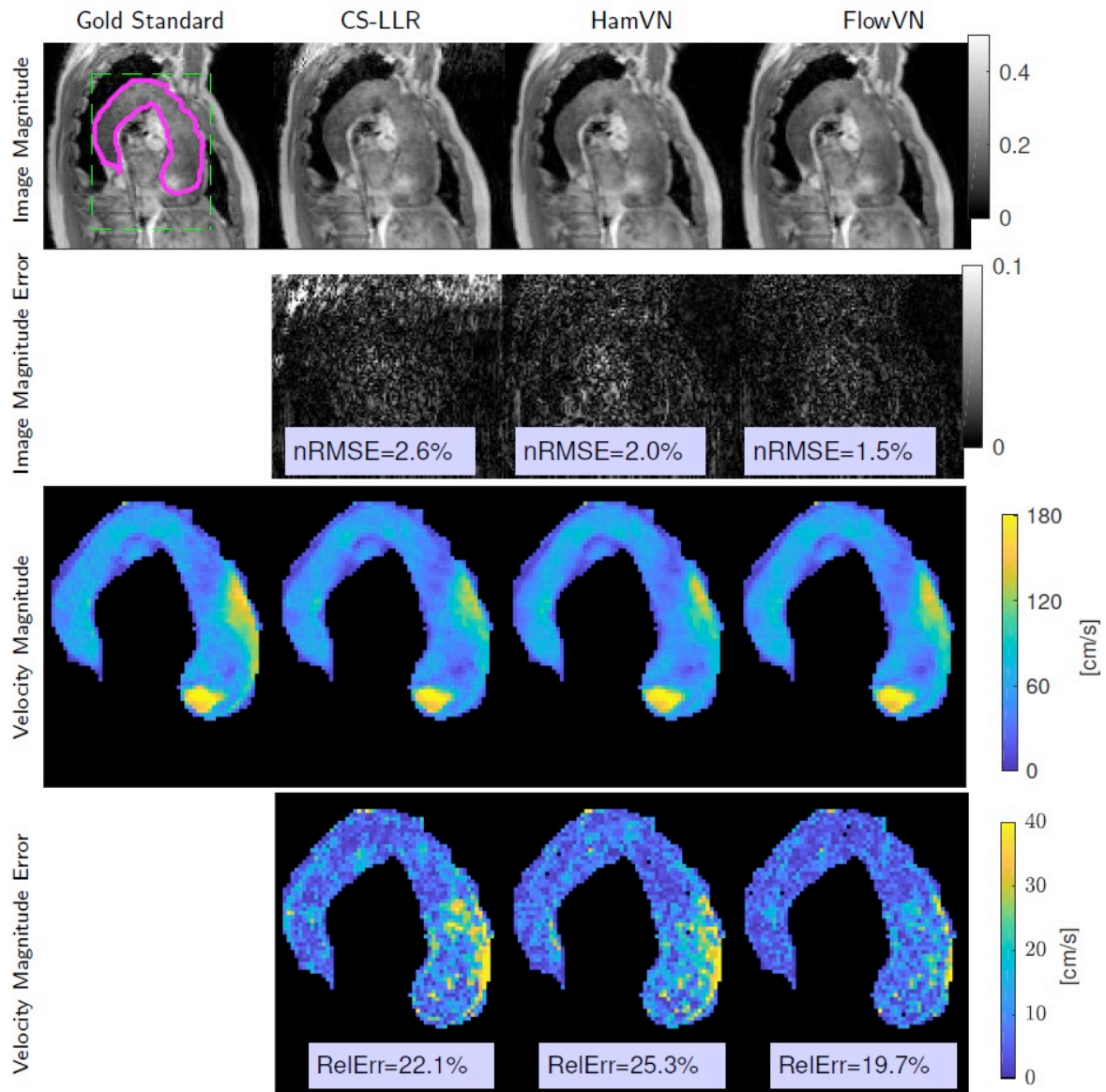


Figure 7.4: Retrospective reconstruction of the data from patient with abnormal flow pattern. Reconstruction results of 10× retrospectively undersampled patient dataset shown at systolic peak. Manual aorta segmentation and field of view are shown with magenta and green lines respectively.

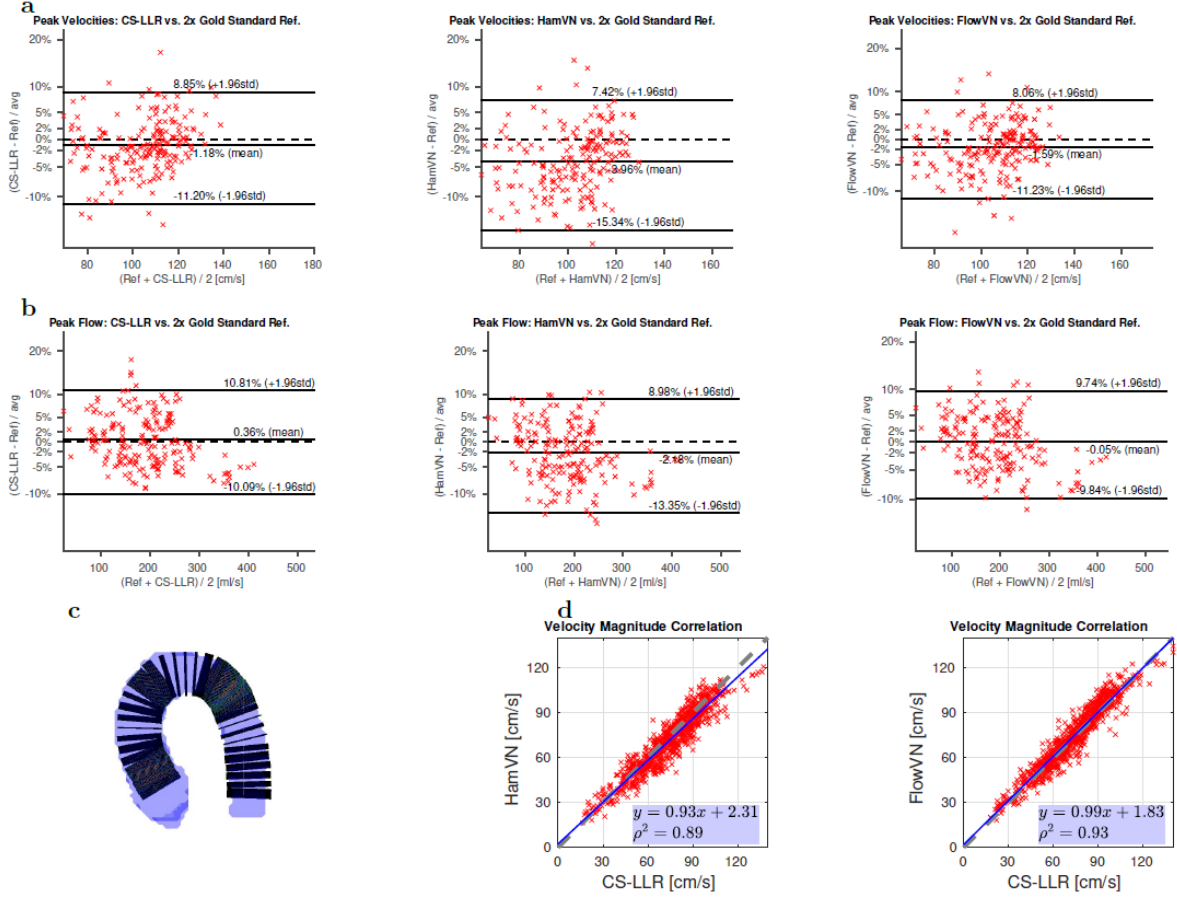


Figure 7.5: Quantitative flow evaluation of reconstruction methods on the prospectively undersampled data ($12.4 \leq R \leq 13.8$). a,b) Bland-Altman analysis of peak velocities and peak flow assessed over manually segmented aorta slices as illustrated in c). d) Correlation analysis of aortic velocity magnitude estimates by learned VN architectures and LLR reconstruction.

7.5 Methods

Compressed Sensing 4D Flow Reconstruction

PC MRI encodes flow velocity $\mathbf{v}(\mathbf{r}, t) \in \mathbb{R}^3$ at a spatial location \mathbf{r} during cardiac phase $t (1 \leq t \leq N_t)$ according to the following equation:

$$s_i(\mathbf{r}, t) = s_0(\mathbf{r}, t) \exp\left(i\pi \frac{(\Phi \mathbf{v}(\mathbf{r}, t))_i}{VENC}\right) \quad (7.4)$$

where $VENC$ is the velocity corresponding to a phase of $\pm\pi$, $y_i, i = 0, \dots, 3$ are the encoded velocity vector components, and the four-point velocity encoding matrix is given as

$$\Phi = \begin{bmatrix} 0 & 0 & 0 \\ 1 & 0 & 0 \\ 0 & 1 & 0 \\ 0 & 0 & 1 \end{bmatrix}. \quad (7.5)$$

Therefore, the flow velocity \mathbf{v} can be calculated from the phase difference of reconstructed PC images \mathbf{s}_i .

Let $\mathbf{s}_{it} \in \mathbb{C}^{N_v}$ be a discretized image on a $N_x \times N_y \times N_z = N_v$ grid corresponding to a cardiac phase t and velocity encoding i . Assuming Cartesian sampling on a regular $N_1 \times N_2 \times N_3 = N_s$ grid, the Fourier transform $\mathcal{F} \in \mathbb{C}^{N_s \times N_v}$, and N_c coil sensitivity maps $W_k = \text{diag}(\mathbf{c}_k) \in \mathbb{C}^{N_v \times N_v}$ define the spatial encoding operator $\mathbf{E} \in \mathbb{C}^{N_s N_c \times N_v}$:

$$\mathbf{E}\mathbf{s} = \left[(FW_1\mathbf{s})^T, \dots, (FW_{N_c}\mathbf{s})^T \right]^T \in \mathbb{C}^{N_s N_c}. \quad (7.6)$$

Considering a single velocity-encoded image sequence, let $\mathbf{S} \in \mathbb{C}^{N_v \times N_t}$ and $\mathbf{D} \in \mathbb{C}^{N_s N_c \times N_t}$ be stacked column-vectors of signals \mathbf{s} and zero-filled k-space samples \mathbf{d} respectively, while $\mathbf{\Omega} \in \{0,1\}^{N_s N_c \times N_t}$ defines the undersampling masks. Iterative image reconstruction methods seek for a maximum a posteriori (MAP) solution defined by the following optimization problem:

$$\hat{\mathbf{s}} = \underset{\mathbf{s}}{\text{argmin}} \frac{1}{2} \|\mathbf{M} \odot (\mathbf{E}\mathbf{P} - \mathbf{D})\|_{\text{F}}^2 + R(\mathbf{P}), \quad (7.7)$$

where the regularization term $R(\mathbf{P})$ enforces prior assumptions about image regularities. Herein we consider the local low-rank (LLR) regularization [33] to leverage image correlations among cardiac phases:

$$R_{LLR}(\mathbf{P}) = \lambda_{LLR} \sum_{i \leq N_{ptch}} \|\mathbf{T}_i \mathbf{S}\|_*, \quad (7.8)$$

where $\mathbf{T}_i \in \{0,1\}^{p^3 \times N_v}$ is the corresponding $p \times p \times p$ patch extraction operator, yielding N_{ptch} overlapping patches, and $\|\cdot\|_*$ is the nuclear norm. For LLR regularization the optimization problem from Equation 7.7 is convex and can be efficiently solved using operator splitting techniques such as the fast iterative shrinkage-thresholding algorithm (FISTA) [77].

FlowVN Training

We employ a $K = 10$ layer VN and perform $5 * 10^4$ iterations of the ADAM algorithm (learning rate 10^{-3} , $\beta_1 = 0.85$, $\beta_2 = 0.98$, batch size of 3) for training, during which we continually adjust $\tau = i_{opt} * 10^{-3}$ with i_{opt} being the iteration number. On every layer, each 3D filter bank contains $N_f = 8$ filters of size $n_c = 5$ voxels. Activation functions $\varphi\{\cdot\}$ are parametrized by $N_{knts} = 71$ control knots with spacing $\omega = 0.17$:

$$\varphi\{h\} = \left(1 - \frac{h}{w} + \left\lfloor \frac{h}{w} \right\rfloor\right) \phi_{\left\lfloor \frac{h}{w} \right\rfloor} + \left(\frac{h}{w} - \left\lfloor \frac{h}{w} \right\rfloor\right) \phi_{\left\lfloor \frac{h}{w} \right\rfloor + 1}, \quad (7.9)$$

with gradients provided by the following formulas:

$$\frac{\delta\varphi}{\delta\phi_i}\{h\} = 1_{i \leq h \leq i+1} * (1 - h + \lfloor h \rfloor) + 1_{i-1 \leq h \leq i} * (h - \lfloor h \rfloor), \quad (7.10)$$

$$\frac{\delta\varphi}{\delta h}\{h\} = \phi_{\lfloor h \rfloor + 1} - \phi_h. \quad (7.11)$$

The acquired zero-filled k-space \mathbf{d} with undersampling mask $\mathbf{\Omega}$ was normalized by $\frac{\|\mathbf{\Omega}\|_1}{\|\mathbf{d}\|_F}$.

To enable the backpropagation to be carried out with limited GPU memory, we employ spatiotemporal equivariance of the convolution and exploit the fact that k-space is fully sampled in the readout dimension k_x for Cartesian acquisitions. Therefore, to draw a training sample, we perform a random cropping of width w_x and w_t in dimensions x and t respectively and simulate Fourier encoding in dimensions k_y, k_z as illustrated in Figure 7.2a. The network was implemented using the Tensorflow framework [200]. Fully-sampled and partial Fourier acquisition data from 11 healthy volunteers was used during training.

In Vivo Data Acquisition

As illustrated in Figure 7.1, we used 11 subject for network training, and 7 healthy subjects and 1 patient for evaluation. All in-vivo work was performed upon written informed consent of the subjects and according to local ethics regulations.

Training datasets comprised 4D flow data measured in the aorta of 11 healthy subjects, 9 of them fully sampled and 2 acquired with partial Fourier [31] (factor 0.75×0.75).

For evaluation, data in the ascending aorta of 7 healthy subjects was acquired on a 3T Philips Ingenia system (Philips Healthcare, Best, the Netherlands) using a Cartesian 4-point referenced phase-contrast gradient-echo sequence with an encoding velocity $venc = 150 \frac{cm}{s}$, a spatial resolution of $2.5 \times 2.5 \times 2.5 \text{ mm}^3$, $TE = 3.3 \text{ ms}$, $TR = 4.9 \text{ ms}$, 25 cardiac phases and flip angle = 8° . Exams for each of the 7 healthy subjects comprised a standard navigator-gated 2-fold accelerated parallel imaging [38] exam for reference, and a compressed sensing acquisition with an acceleration factor of 12.4 – 13.8, using Cartesian pseudo-radial golden angle sampling pattern [62] and data driven-respiratory motion detection, as in [177]. Only data in expiration were kept for reconstruction as shown in Figure 7.1.

To evaluate reconstruction accuracy on pathological anatomy, 4D flow data was acquired in a single patient with dilation of the ascending aorta and combined aortic stenosis and regurgitation due to a bicuspid aortic valve on a 3T Philips Ingenia system (Philips Healthcare, Best, the Netherlands) using a navigator-gated 2-fold accelerated parallel imaging [38] scan.

A receiver coil with 28 channels was used for acquisition which were reduced to 5 channels using coil compression [196]. Coil sensitivity maps were estimated with ESPIRiT [69]. Concomitant field

correction was applied to the signal phase according to Bernstein et al. [144] and eddy currents were corrected for with a third-order polynomial model fitted to stationary tissue [145], [169].

Evaluation

We compared the proposed FlowVN to the state-of-the-art compressed sensing LLR-regularized (Equation 7.8) reconstruction [33] and the variational network by Hammernik et al. [110] which we refer to as HamVN. LLR implementation from the Berkeley advanced reconstruction toolbox (BART) [167] was used with patch size $p = 8$ and maximum number of optimization iterations of 120. The optimal value of regularization parameter $\lambda_{LLR} = 2.06 * 10^{-2}$ was chosen via grid search to minimize the reconstructed flow field residual $\|\hat{\mathbf{v}} - \mathbf{v}^*\|_2$ averaged over the manually segmented aorta on the retrospectively 12-fold undersampled acquisition. To overcome memory limitations, we adapted HamVN from [110] in the following ways: (i) 3D filters were grouped into 4 banks as in 1, (ii) activation functions were parameterized by linear interpolation as in Equation 9 instead of memory demanding radial basis functions. The number of network layers, filters and control knots were the same as in FlowVN.

Retrospective Study

For simulated retrospective undersampling experiments, we used 2x PI data and simulated pseudo-radial golden angle sampling pattern [62] with acceleration factors of 6 to 22.

For each undersampling rate we evaluated the normalized root mean square error (nRMSE) of image magnitude, the relative error (RelErr) of velocity magnitudes inside the aorta and the angular error (AngErr) of the estimated velocity vectors:

$$nRMSE(\mathbf{a}, \mathbf{a}^*) = \sqrt{\sum_i^N \frac{(a_i - a_i^*)^2}{N * \max_j(a_j^*)^2}} \quad (7.12)$$

$$RelErr(\mathbf{a}, \mathbf{a}^*) = \frac{\|\mathbf{a} - \mathbf{a}^*\|_2}{\|\mathbf{a}^*\|_2}, \quad (7.13)$$

$$AngErr(\mathbf{u}, \mathbf{v}) = \arccos\left(\frac{\langle \mathbf{u}, \mathbf{v} \rangle}{\|\mathbf{u}\|_2 \|\mathbf{v}\|_2}\right). \quad (7.14)$$

Prospective Study

Using manual aorta segmentations we compute flow over cross sections of the aorta by integrating velocity components projected onto the cross section normal. The peak flow is then defined as the maximal flow over cardiac phases for a given cross section. Moreover, we calculate the peak through-

plane velocity defined as maximum velocity projection across cross sections of the aorta over cardiac phases.

To quantify agreement with the reference 2× PI reconstruction, we performed Bland-Altman analysis [170] of peak flow and peak through-plane velocities.

7.6 Supplementary Materials

Algorithm S7.1: Proposed variational reconstruction network model FlowVN.

Input: $\mathbf{B} \in \mathbb{C}^{N_s \times N_t}$ — zero-filled k-space samples, $\mathbf{M} \in \{0, 1\}^{N_s \times N_t}$ — undersampling mask
Parameters: $\Theta = \{\phi_{\text{ud}}^{(k)}, \phi_{\text{ur}}^{(k)}, \phi_{\text{d}}^{(k)}, \phi_{\text{r,in}}^{(k)}, \mathbf{D}_{\text{in}}^{(k)}, \alpha^{(k)}, \alpha^{(0)}\}_{i=1, \dots, N_f, k=1, \dots, K, n=1, \dots, 4}$
 $\overline{\mathbf{M}} \leftarrow \frac{1}{N_s N_t} \sum_{i \leq N_s, j \leq N_t} M_{ij}$
 $\mathbf{P}^{(0)} \leftarrow \alpha^{(0)} \mathbf{E}^H \mathbf{B}$, $\mathbf{S}^{(0)} \leftarrow \mathbf{0}$
for $k := 0$ to $K - 1$

$$\mathbf{G}^{(k)} \leftarrow \overbrace{\varphi_{\text{ud}}^{(k)} \{\overline{\mathbf{M}}\} \mathbf{E}^H \left(\mathbf{M} \odot \varphi_{\text{d}}^{(k)} \left\{ \mathbf{M} \odot \left(\mathbf{E} \mathbf{P}^{(k)} - \mathbf{B} \right) \right\} \right)}^{\text{data consistency term}} + \overbrace{\varphi_{\text{ur}}^{(k)} \{\overline{\mathbf{M}}\} \sum_{i \leq N_t, n \leq 4} \left(\mathbf{D}_{\text{in}}^{(k)} \right)^T \varphi_{\text{r,in}}^{(k)} \left\{ \mathbf{D}_{\text{in}}^{(k)} \text{vec} \left(\mathbf{P}^{(k)} \right) \right\}}^{\text{regularization term}}$$

$$\mathbf{S}^{(k+1)} \leftarrow \alpha^{(k+1)} \mathbf{S}^{(k)} + \mathbf{G}^{(k)}$$

$$\mathbf{P}^{(k+1)} \leftarrow \mathbf{P}^{(k)} - \mathbf{S}^{(k+1)}$$

Output: reconstructed image $\mathcal{V}(\mathbf{B}, \mathbf{M}; \Theta) \stackrel{\text{def}}{=} \mathbf{P}^{(K)}$

Table S7.1: Comparison of reconstruction errors (\pm standard deviation) of 7 retrospectively undersampled acquisitions of healthy subjects for different acceleration factors R . For each row the best performing method is highlighted in bold.

| | Image Magnitude nRMSE [%] | | | Velocity Magnitude RelErr [%] | | | Mean Flow AngErr [deg] | | |
|--------|---------------------------|---------------|----------------------|-------------------------------|----------------|-----------------------|------------------------|----------------|-----------------------|
| | LLR | HamVN | FlowVN | LLR | HamVN | FlowVN | LLR | HamVN | FlowVN |
| $R=6$ | 2.0 \pm 0.2 | 2.3 \pm 0.3 | 1.9 \pm 0.4 | 9.7 \pm 3.2 | 11.9 \pm 3.6 | 9.6 \pm 3.7 | 7.3 \pm 3.2 | 9.1 \pm 3.7 | 7.4 \pm 3.5 |
| $R=8$ | 2.2 \pm 0.4 | 2.6 \pm 0.4 | 2.1 \pm 0.4 | 11.3 \pm 4.0 | 13.3 \pm 3.9 | 10.8 \pm 3.9 | 8.4 \pm 4.0 | 10.1 \pm 4.3 | 8.5 \pm 4.0 |
| $R=10$ | 2.5 \pm 0.5 | 2.9 \pm 0.5 | 2.4 \pm 0.5 | 13.0 \pm 4.2 | 14.9 \pm 4.5 | 12.1 \pm 4.3 | 9.5 \pm 4.3 | 11.0 \pm 4.5 | 9.5 \pm 4.3 |
| $R=12$ | 3.0 \pm 0.8 | 3.2 \pm 0.6 | 2.7 \pm 0.5 | 15.9 \pm 5.8 | 16.7 \pm 5.4 | 14.0 \pm 5.3 | 10.9 \pm 5.4 | 12.2 \pm 5.3 | 10.7 \pm 5.0 |
| $R=14$ | 3.3 \pm 0.8 | 3.5 \pm 0.6 | 2.9 \pm 0.5 | 16.9 \pm 5.0 | 18.1 \pm 4.5 | 14.8 \pm 4.9 | 11.6 \pm 5.5 | 12.8 \pm 5.4 | 11.3 \pm 5.1 |
| $R=16$ | 4.0 \pm 1.0 | 3.7 \pm 0.7 | 3.1 \pm 0.6 | 20.5 \pm 6.2 | 20.5 \pm 5.0 | 16.5 \pm 5.1 | 13.0 \pm 6.0 | 13.5 \pm 5.4 | 12.2 \pm 5.1 |
| $R=18$ | 4.3 \pm 1.1 | 4.0 \pm 0.8 | 3.4 \pm 0.7 | 22.3 \pm 7.6 | 22.0 \pm 5.5 | 18.2 \pm 6.5 | 13.9 \pm 6.1 | 13.9 \pm 5.5 | 12.8 \pm 5.4 |
| $R=20$ | 4.6 \pm 1.2 | 4.2 \pm 0.8 | 3.5 \pm 0.7 | 23.5 \pm 6.9 | 23.3 \pm 5.4 | 19.5 \pm 6.1 | 14.4 \pm 6.1 | 14.6 \pm 6.0 | 13.5 \pm 5.7 |
| $R=22$ | 4.9 \pm 1.3 | 4.4 \pm 0.9 | 3.7 \pm 0.7 | 24.7 \pm 6.4 | 24.4 \pm 6.2 | 20.4 \pm 7.3 | 14.6 \pm 6.4 | 14.7 \pm 6.1 | 13.8 \pm 5.9 |

Chapter 8 Summary

Phase-contrast encoding in the presence of turbulent flows has measurable effects on signal phase and magnitude which can be used to derive mean and fluctuating velocity components. This allows for non-invasive in vivo assessment of transient and turbulent flows. However, the large amount of data to be acquired, and hence long scan times, hamper in vivo applications and clinical use. The aim of this work was to provide turbulence assessment with MRI within a fixed and short duration, and to use reductions in scan time to enable in vivo assessment of the Reynolds stress tensor (RST).

To this end, we have investigated respiratory motion resolved imaging to make the acquisition more efficient. Moreover, reconstruction methods based on low-rankedness and deep neural networks have been proposed and implemented to exploit redundancies in the data and reconstruct images from subsets of k-space. Improvements in scan efficiency allowed to extend the sequence with additional velocity encodings resulting in multipoint flow tensor encoding enabling the first successful in vivo assessments of the RST.

8.1 Discussion

Scan acceleration of 4D Flow MRI based on partial Fourier (PF) acquisition has been critically reviewed. It has been shown that the underlying assumption, that spatial phase variations are limited to low spatial frequencies does not hold for 4D Flow MRI. Enforcing this model assumption in the image reconstruction leads to artifacts. Moreover, no benefit in reconstruction accuracy is achieved relative to performing the acquisition at a lower resolution. While experiments were limited to 4D Flow MRI and the analysis of mean velocities and TKE, the relevance of our findings extends to other imaging applications where the signal shows rapid spatial phase variations, e.g. in cardiac perfusion MRI [205]. A 5D Flow MRI framework for resolving flow over cardiac and respiratory motion states was implemented. K-space acquisition was performed with a pseudo-radial Cartesian Golden angle sampling trajectory. Data driven motion detection was used to attribute k-space samples to different respiratory motion states. In image reconstruction, a locally low rank model was employed to exploit correlations over respiratory motion states and cardiac phases. Thus, scan time for the in vivo assessment of TKE was reduced to 4 minutes independent of the subject's respiratory motion pattern. Validation against conventional parallel imaging-based acceleration showed consistent results while scan time was reduced by a factor of approximately 4.5 on average. Beyond flow imaging applications, respiratory motion resolved imaging is also promising to decouple respiratory motion and scan time

for other applications provided that suitable respiratory motion detection methods are available in case the readout direction is not aligned with axes of respiratory motion, e.g. [206], [207].

We have proposed and implemented the concept of 5D Flow Tensor MRI, a method to efficiently quantify velocities and Reynolds stresses in the aorta. The combination of the 5D Flow MRI sequence with a 19-point flow tensor encoding scheme has enabled the in vivo assessment of the entire Reynolds stress tensor. Numerical experiments have demonstrated high precision of the method but an overestimation of turbulent flow components which can be attributed to limitations in the acquisition voxel size. However, decreasing the acquisition voxel size would lead to a considerable increase in scan time. Therefore, this systematic error must be taken into account when using the data as input for simulations or when performing quantitative assessments. A first in vivo study showed distinct qualitative differences in turbulent shear stresses and TKE between patients with a bio-prosthetic heart valve and healthy controls. Further clinical experiments are, however, warranted to further assess the distributions of turbulent flow components downstream of healthy and diseased aortic valves in view of clinical translation of the method.

The feasibility of rapid image reconstruction of undersampled 4D Flow MRI acquisitions with variational neural networks has been demonstrated. Our study showed that training on 11 retrospectively undersampled datasets of healthy subjects was sufficient to accurately reconstruct pathological flow in the aorta of a patient and to provide accurate results in a prospectively undersampled imaging study. The finding, that training based on retrospectively undersampled healthy flow data is sufficient for reconstruction of pathological flow, makes variational neural networks promising for many other applications in MRI and beyond where little training data are available. The method can also be extended to the reconstruction of 5D Flow MRI. As our previous results show [177], the respiratory motion dimension is highly correlated. Thus, learning correlations also along the respiratory motion dimension promises accurate reconstructions from acquisitions with even higher undersampling rates. However, as no ground truth data are available, one would need to rely on simulated data, or consider the results of CS reconstructions as training data, which might put an upper limit on the achievable reconstruction accuracy.

8.2 Outlook

Besides using the proposed framework for clinical studies, further investigations are warranted to increase accuracy of the assessment and further reduce scan and reconstruction times.

Direct Reconstruction of Mean and Turbulent Velocity Components

To provide accurate assessment of the RST, 6-directional velocity encoding was combined with a multipoint encoding scheme. Following reconstruction, Bayesian multipoint unfolding was applied separately for each voxel and each encoding direction to determine the most likely mean velocity and intra-voxel standard deviation and covariances. With this approach, spatiotemporal relationships or correlations among encoding directions were not considered when combining the multipoint measurements.

Instead of having separate steps for image reconstruction, multipoint unfolding, and estimation of mean velocities and the RST, incorporation of all steps into a single image reconstruction algorithm would be desirable for simplification and to exploit data redundancies throughout the processing pipeline. To this end, variational neural network approaches may be considered to directly learn spatiotemporal correlations as well as relationships between different velocity encoded measurements to provide a direct reconstruction of the desired quantities.

Inaccuracies and Limitations of the Signal Model

Further investigations into inaccuracies of the signal model as assumed in generalized PC-MRI [20] are considered important. In this work it has been shown, that due to limitations in acquisition resolution, turbulent velocity fluctuations are overestimated. An additional source of inaccuracy might be a non-uniform sensitivity to different parts of the turbulence spectrum. As the measurement corresponds to a convolution of the spectra of the velocity autocorrelation and the velocity encoding gradient waveforms [208], [209], the assessment has a varying sensitivity over the frequency range of turbulent velocity fluctuations. This effect still has to be investigated in detail for turbulent flow encoding, but might require consideration of different kinds of velocity encoding gradient waveforms.

Data assimilation [179] approaches might be an option to mitigate the effect of coarse acquisition resolution on turbulent velocity components. Moreover, optimal experimental design, incorporating the full pipeline from acquisition to post-processing, should be aimed for.

High Dimensional Flow Imaging

In this work, flow imaging has been extended to incorporate the respiratory motion dimension and to include additional velocity encodings for turbulence encoding. With the increasing capabilities to store and process large datasets, even more signal dimensions shall be encoded into a single scan and subsequently exploited in data reconstruction and processing. For example, flow imaging has already been combined with dynamic contrast enhancement [56] and low-resolution real time data were reconstructed from a multidimensional flow acquisition [207]. Moreover, for imaging of turbulent flow, combination with a multi-echo gradient-echo sequence [210] appears a promising option, which would also yield T_2^* -maps and might make acquisition of a reference segment obsolete.

Clinical Potential of Turbulence Assessment

The ability of robust in vivo assessment of Reynolds stresses enables new methods for the assessment of cardiac hemodynamics. By providing the full RST, the method can be used to identify elevated turbulent shear stresses which have been associated with flow-induced damage to red blood cells [181], [211]. Elevated turbulent shear stresses have also been observed for certain aortic heart valve prostheses in in-vitro experiments [183]. Thus, in vivo turbulence assessment with MRI may provide further insights into the occurrence of shear stresses for different prosthetic valves.

For the assessment of cardiac valve insufficiencies, new metrics such as total turbulence production [26] or TKE [22] can be assessed more easily. The latter was already demonstrated to have value in patients with aortic stenosis [22]. However, a remaining problem when comparing these metrics in in vivo studies is posed by the lack of ground truth, as catheterization is not performed in every patient and assessment by Doppler echocardiography, the primary technique used in clinical practice, tends to underestimate stenosis severity, as pressure recovery is neglected [212].

The availability of the RST allows for direct calculation of relative pressure fields using the Reynolds averaged Navier-Stokes equation [19]. In vivo RST measurements can also provide valuable input data for numerical models of the in vivo heart and patient-specific simulations of the heart.

Ideally, for a longitudinal study, image segmentation should not happen manually anymore in order to reduce intra- and inter-observer variability and to introduce objective quantitative criteria. Recently, advances in fully automated segmentation of the aorta have been demonstrated by using the U-Net architecture [213], a special type of convolutional neural networks [214]. However, adaptation of machine learning based routines for the segmentation of 4D Flow MRI data is still hampered by the limited availability of labelled data and the lack of ground truth data.

Public Availability of Code

With the framework developed in this thesis work, rapid in vivo assessment of turbulence can be easily integrated into clinical exams of patients, allowing for in vivo studies with a larger number of subjects. To further facilitate clinical adaptation, code for locally low rank reconstruction and Bayesian multipoint unfolding is provided as a platform independent Docker image which can be run in data handling platforms such as Agora (GyrotTools LLC, Winterthur, Switzerland). Moreover, evaluation scripts for Reynolds stresses as well as variational network-based reconstruction have been made publicly available on GitHub (<https://github.com/j-walheim>).

Chapter 9 References

- [1] M. Markl, A. Frydrychowicz, S. Kozerke, M. Hope, and O. Wieben, "4D flow MRI," *Journal of Magnetic Resonance Imaging*, vol. 36, no. 5, pp. 1015–1036, 2012.
- [2] J. Garcia *et al.*, "Assessment of altered three-dimensional blood characteristics in aortic disease by velocity distribution analysis," *Magn. Reson. Med.*, vol. 74, no. 3, pp. 817–825, 2015.
- [3] J. Garcia *et al.*, "Four-dimensional flow magnetic resonance imaging-based characterization of aortic morphometry and haemodynamics: impact of age, aortic diameter, and valve morphology," *Eur. Hear. Journal-Cardiovascular Imaging*, vol. 17, no. 8, pp. 877–884, 2015.
- [4] M. Sigovan, M. D. Hope, P. Dyverfeldt, and D. Saloner, "Comparison of four-dimensional flow parameters for quantification of flow eccentricity in the ascending aorta," *J. Magn. Reson. Imaging*, vol. 34, no. 5, pp. 1226–1230, 2011.
- [5] J. von Spiczak, G. Crelier, D. Giese, S. Kozerke, D. Maintz, and A. C. Bunck, "Quantitative analysis of vortical blood flow in the thoracic aorta using 4D phase contrast MRI," *PLoS One*, vol. 10, no. 9, p. e0139025, 2015.
- [6] M. D. Hope *et al.*, "Evaluation of bicuspid aortic valve and aortic coarctation with 4D flow magnetic resonance imaging," *Circulation*, vol. 117, no. 21, pp. 2818–2819, 2008.
- [7] W. V Potters, P. van Ooij, H. Marquering, E. vanBavel, and A. J. Nederveen, "Volumetric arterial wall shear stress calculation based on cine phase contrast MRI," *J. Magn. Reson. Imaging*, vol. 41, no. 2, pp. 505–516, 2015.
- [8] A. F. Stalder, M. F. Russe, A. Frydrychowicz, J. Bock, J. Hennig, and M. Markl, "Quantitative 2D and 3D phase contrast MRI: optimized analysis of blood flow and vessel wall parameters," *Magn. Reson. Med. An Off. J. Int. Soc. Magn. Reson. Med.*, vol. 60, no. 5, pp. 1218–1231, 2008.
- [9] E. T. Biegging *et al.*, "In vivo three-dimensional MR wall shear stress estimation in ascending aortic dilatation," *J. Magn. Reson. Imaging*, vol. 33, no. 3, pp. 589–597, 2011.
- [10] T. Ebberts, L. Wigstrom, A. F. Bolger, B. Wranne, and M. Karlsson, "Noninvasive measurement of time-varying three-dimensional relative pressure fields within the human heart," *J. Biomech. Eng.*, vol. 124, no. 3, pp. 288–293, 2002.
- [11] G.-Z. Yang, P. J. Kilner, N. B. Wood, S. R. Underwood, and D. N. Firmin, "Computation of flow pressure fields from magnetic resonance velocity mapping," *Magn. Reson. Med.*, vol. 36, no. 4, pp. 520–526, 1996.
- [12] J. M. Tyszka, D. H. Laidlaw, J. W. Asa, and J. M. Silverman, "Three-dimensional, time-resolved

- (4D) relative pressure mapping using magnetic resonance imaging," *J. Magn. Reson. Imaging*, vol. 12, no. 2, pp. 321–329, 2000.
- [13] M. Markl, W. Wallis, S. Brendecke, J. Simon, A. Frydrychowicz, and A. Harloff, "Estimation of global aortic pulse wave velocity by flow-sensitive 4D MRI," *Magn. Reson. Med.*, vol. 63, no. 6, pp. 1575–1582, 2010.
- [14] P. Dyverfeldt, T. Ebberts, and T. Länne, "Pulse wave velocity with 4D flow MRI: systematic differences and age-related regional vascular stiffness," *Magn. Reson. Imaging*, vol. 32, no. 10, pp. 1266–1271, 2014.
- [15] J. Westenberg *et al.*, "Age-related and regional changes of aortic stiffness in the Marfan syndrome: assessment with velocity-encoded MRI," *J. Magn. Reson. Imaging*, vol. 34, no. 3, pp. 526–531, 2011.
- [16] A. J. Barker *et al.*, "Viscous energy loss in the presence of abnormal aortic flow," *Magn. Reson. Med.*, vol. 72, no. 3, pp. 620–628, 2014.
- [17] P. D. Stein and H. N. Sabbah, "Turbulent blood flow in the ascending aorta of humans with normal and diseased aortic valves," *Circ. Res.*, vol. 39, no. 1, pp. 58–65, 1976.
- [18] C. W. Akins, B. Travis, and A. P. Yoganathan, "Energy loss for evaluating heart valve performance," *J. Thorac. Cardiovasc. Surg.*, vol. 136, no. 4, pp. 820–833, 2008.
- [19] H. Haraldsson *et al.*, "Assessment of Reynolds stress components and turbulent pressure loss using 4D flow MRI with extended motion encoding," *Magn. Reson. Med.*, vol. 79, no. 4, pp. 1962–1971, 2018.
- [20] P. Dyverfeldt, A. Sigfridsson, J. P. E. Kvitting, and T. Ebberts, "Quantification of intravoxel velocity standard deviation and turbulence intensity by generalizing phase-contrast MRI," *Magn. Reson. Med.*, vol. 56, no. 4, pp. 850–858, 2006.
- [21] P. Dyverfeldt, M. D. Hope, E. E. Tseng, and D. Saloner, "Magnetic resonance measurement of turbulent kinetic energy for the estimation of irreversible pressure loss in aortic stenosis," *JACC Cardiovasc. Imaging*, vol. 6, no. 1, pp. 64–71, 2013.
- [22] C. Binter, A. Gotschy, R. Manka, and S. Kozerke, "Turbulent Kinetic Energy Assessed by Multipoint 4D Flow MRI Provides Additional Information Relative to Echocardiography for the Determination of Aortic Stenosis Severity," *Circ. Cardiovasc. Imaging*, 2017.
- [23] J. Zajac, J. Eriksson, P. Dyverfeldt, A. F. Bolger, T. Ebberts, and C.-J. Carlhäll, "Turbulent kinetic energy in normal and myopathic left ventricles," *J. Magn. Reson. Imaging*, vol. 41, no. 4, pp. 1021–1029, 2015.
- [24] K. M. Hasan, D. L. Parker, and A. L. Alexander, "Comparison of gradient encoding schemes for

- diffusion-tensor MRI," *J. Magn. Reson. Imaging*, vol. 13, no. 5, pp. 769–780, 2001.
- [25] C. Binter, V. Knobloch, A. Sigfridsson, and S. Kozerke, "Direct quantification of turbulent shear stresses by multi-point phase-contrast MRI," in *Proceedings of the 20th Annual Meeting of ISMRM*, 2012, p. 199.
- [26] H. Ha *et al.*, "Estimating the irreversible pressure drop across a stenosis by quantifying turbulence production using 4D Flow MRI," *Nat. Publ. Gr.*, vol. 7, no. November 2016, pp. 1–14, 2017.
- [27] H. Ha, J. Lantz, H. Haraldsson, B. Casas, and M. Ziegler, "Assessment of turbulent viscous stress using ICOSA 4D Flow MRI for prediction of hemodynamic blood damage," *ISMRM Flow Motion Work. 2016*, p. 2000, 2016.
- [28] C. J. Elkins, M. T. Alley, L. SaeTRAN, and J. K. Eaton, "Three-dimensional magnetic resonance velocimetry measurements of turbulence quantities in complex flow," *Exp. Fluids*, vol. 46, no. 2, pp. 285–296, 2009.
- [29] H. Ha, J. P. E. Kvitting, P. Dyverfeldt, and T. Ebbers, "Validation of pressure drop assessment using 4D flow MRI-based turbulence production in various shapes of aortic stenoses," *Magn. Reson. Med.*, no. February, pp. 893–906, 2018.
- [30] D. A. Feinberg, J. D. Hale, J. C. Watts, L. Kaufman, and A. Mark, "Halving MR imaging time by conjugation: demonstration at 3.5 kG.," *Radiology*, vol. 161, no. 2, pp. 527–531, 1986.
- [31] J. Cuppen and A. van Est, "Reducing MR imaging time by one-sided reconstruction," *Magn. Reson. Imaging*, vol. 5, no. 6, pp. 526–527, 1987.
- [32] M. Lustig, D. Donoho, and J. M. Pauly, "Sparse MRI: The application of compressed sensing for rapid MR imaging," *Magn. Reson. Med.*, vol. 58, no. 6, pp. 1182–1195, 2007.
- [33] T. Zhang, J. M. Pauly, and I. R. Levesque, "Accelerating parameter mapping with a locally low rank constraint," *Magn. Reson. Med.*, vol. 73, no. 2, pp. 655–661, 2015.
- [34] G. Valvano *et al.*, "Accelerating 4D flow MRI by exploiting low-rank matrix structure and hadamard sparsity," *Magn. Reson. Med.*, vol. 78, no. 4, pp. 1330–1341, 2017.
- [35] R. Otazo, E. Candès, and D. K. Sodickson, "Low-rank plus sparse matrix decomposition for accelerated dynamic MRI with separation of background and dynamic components," *Magn. Reson. Med.*, vol. 73, no. 3, pp. 1125–1136, 2015.
- [36] L. Feng, L. Axel, H. Chandarana, K. T. Block, D. K. Sodickson, and R. Otazo, "XD-GRASP: Golden-angle radial MRI with reconstruction of extra motion-state dimensions using compressed sensing," *Magn. Reson. Med.*, vol. 75, no. 2, pp. 775–788, 2016.
- [37] D. C. Noll, D. G. Nishimura, and A. Macovski, "Homodyne detection in magnetic resonance

- imaging," *IEEE Trans. Med. Imaging*, vol. 10, no. 2, pp. 154–163, 1991.
- [38] K. P. Pruessmann, M. Weiger, M. B. Scheidegger, and P. Boesiger, "SENSE: Sensitivity encoding for fast MRI," *Magn. Reson. Med.*, vol. 42, no. 5, pp. 952–962, 1999.
- [39] Y. LeCun, Y. Bengio, and G. Hinton, "Deep learning," *Nature*, vol. 521, p. 436, May 2015.
- [40] M. Kouwenhoven, M. B. M. Hofman, and M. Sprenger, "Motion induced phase shifts in MR: acceleration effects in quantitative flow measurements—a reconsideration," *Magn. Reson. Med.*, vol. 33, no. 6, pp. 766–777, 1995.
- [41] S. A. E. D. R. Pelc Norbert J. Herfkens Robert J., "Phase contrast cine magnetic resonance imaging.," *Magn. Reson. Q.*, 1991.
- [42] A. T. Lee, G. Bruce Pike, and N. J. Pelc, "Three-Point Phase-Contrast Velocity Measurements with Increased Velocity-to-Noise Ratio," *Magn. Reson. Med.*, vol. 33, no. 1, pp. 122–126, 1995.
- [43] P. Chai and R. Mohiaddin, "How we perform cardiovascular magnetic resonance flow assessment using phase-contrast velocity mapping," *J. Cardiovasc. Magn. Reson.*, vol. 7, no. 4, pp. 705–716, 2005.
- [44] E. Bollache, P. van Ooij, A. Powell, J. Carr, M. Markl, and A. J. Barker, "Comparison of 4D flow and 2D velocity-encoded phase contrast MRI sequences for the evaluation of aortic hemodynamics," *Int. J. Cardiovasc. Imaging*, vol. 32, no. 10, 2016.
- [45] N. J. Pelc, M. A. Bernstein, A. Shimakawa, and G. H. Glover, "Encoding strategies for three-direction phase-contrast MR imaging of flow.," *J. Magn. Reson. Imaging*, vol. 1, no. 4, pp. 405–413, Jan. 1991.
- [46] K. M. Johnson and M. Markl, "Improved SNR in phase contrast velocimetry with five-point balanced flow encoding," *Magn. Reson. Med.*, vol. 63, no. 2, pp. 349–355, 2010.
- [47] N. R. Zwart and J. G. Pipe, "Multidirectional high-moment encoding in phase contrast MRI," *Magn. Reson. Med.*, vol. 69, no. 6, pp. 1553–1564, 2013.
- [48] A. A. Joseph *et al.*, "Real-time phase-contrast MRI of cardiovascular blood flow using undersampled radial fast low-angle shot and nonlinear inverse reconstruction," *NMR Biomed.*, vol. 25, no. 7, pp. 917–924, 2012.
- [49] M. Fasshauer *et al.*, "Real-time phase-contrast flow MRI of haemodynamic changes in the ascending aorta and superior vena cava during Mueller manoeuvre," *Clin. Radiol.*, vol. 69, no. 10, pp. 1066–1071, 2014.
- [50] E. Bollache *et al.*, "k-t accelerated aortic 4D flow MRI in under two minutes: feasibility and impact of resolution, k-space sampling patterns, and respiratory navigator gating on hemodynamic measurements," *Magn. Reson. Med.*, vol. 79, no. 1, pp. 195–207, 2018.

- [51] P. Dyverfeldt and T. Ebbers, "Comparison of respiratory motion suppression techniques for 4D flow MRI," *Magn. Reson. Med.*, vol. 78, no. 5, pp. 1877–1882, 2017.
- [52] P. Dyverfeldt *et al.*, "4D flow cardiovascular magnetic resonance consensus statement," *J. Cardiovasc. Magn. Reson.*, vol. 17, no. 1, p. 1, 2015.
- [53] C. Santelli *et al.*, "Respiratory bellows revisited for motion compensation: preliminary experience for cardiovascular MR.," *Magn. Reson. Med.*, vol. 65, no. 4, pp. 1097–1102, 2011.
- [54] S. Uribe, P. Beerbaum, T. S. Sørensen, A. Rasmusson, R. Razavi, and T. Schaeffter, "Four-dimensional (4D) flow of the whole heart and great vessels using real-time respiratory self-gating," *Magn. Reson. Med.*, vol. 62, no. 4, pp. 984–992, 2009.
- [55] A. Sigfridsson, L. Wigström, J. P. E. Kvitting, and H. Knutsson, "k-t2 BLAST: Exploiting spatiotemporal structure in simultaneously cardiac and respiratory time-resolved volumetric imaging," *Magn. Reson. Med.*, vol. 58, no. 5, pp. 922–930, 2007.
- [56] J. Y. Cheng *et al.*, "Comprehensive Multi-Dimensional MRI for the Simultaneous Assessment of Cardiopulmonary Anatomy and Physiology," *Sci. Rep.*, vol. 7, no. 1, pp. 6–9, 2017.
- [57] S. B. Pope, "Turbulent flows." IOP Publishing, 2001.
- [58] C. Binter, V. Knobloch, R. Manka, A. Sigfridsson, and S. Kozerke, "Bayesian multipoint velocity encoding for concurrent flow and turbulence mapping," *Magn. Reson. Med.*, vol. 69, no. 5, pp. 1337–1345, 2013.
- [59] D. G. Taylor and M. C. Bushell, "The spatial mapping of translational diffusion coefficients by the NMR imaging technique," *Phys. Med. Biol.*, vol. 30, no. 4, p. 345, 1985.
- [60] G. McGibney, M. R. Smith, S. T. Nichols, and A. Crawley, "Quantitative evaluation of several partial Fourier reconstruction algorithms used in MRI," *Magn. Reson. Med.*, vol. 30, no. 1, pp. 51–59, 1993.
- [61] Klaas P. Pruessmann, "Advances in Sensitivity Encoding With Arbitrary k-Space Trajectories," vol. 651, pp. 638–651, 2001.
- [62] S. Winkelmann, T. Schaeffter, T. Koehler, H. Eggers, and O. Doessel, "An optimal radial profile order based on the golden ratio for time-resolved MRI," *IEEE Trans. Med. Imaging*, vol. 26, no. 1, pp. 68–76, 2007.
- [63] J. Y. Cheng *et al.*, "Comprehensive motion-compensated highly accelerated 4D flow MRI with ferumoxytol enhancement for pediatric congenital heart disease," *J. Magn. Reson. Imaging*, vol. 43, no. 6, pp. 1355–1368, 2016.
- [64] E. M. Haacke, E. D. Lindsogj, and W. Lin, "A fast, iterative, partial-fourier technique capable of local phase recovery," *J. Magn. Reson.*, vol. 92, no. 1, pp. 126–145, 1991.

- [65] P. B. Roemer, W. A. Edelstein, C. E. Hayes, S. P. Souza, and O. M. Mueller, "The NMR phased array," *Magn. Reson. Med.*, vol. 16, no. 2, pp. 192–225, 1990.
- [66] A. N. Tikhonov and V. Y. Arsenin, "Solution of incorrectly formulated problems and the regularization method," *Sov. Math. Dokl.*, vol. 4, 1963.
- [67] M. A. Griswold *et al.*, "Generalized Autocalibrating Partially Parallel Acquisitions (GRAPPA)," *Magn. Reson. Med.*, vol. 47, no. 6, pp. 1202–1210, 2002.
- [68] M. Lustig and J. M. Pauly, "SPIRiT: Iterative self-consistent parallel imaging reconstruction from arbitrary k-space," *Magn. Reson. Med.*, vol. 64, no. 2, pp. 457–471, 2010.
- [69] M. Uecker *et al.*, "ESPIRiT—an eigenvalue approach to autocalibrating parallel MRI: where SENSE meets GRAPPA," *Magn. Reson. Med.*, vol. 71, no. 3, pp. 990–1001, 2014.
- [70] F. Wiesinger, P. Boesiger, and K. P. Pruessmann, "Electrodynamics and ultimate SNR in parallel MR imaging," *Magn. Reson. Med. An Off. J. Int. Soc. Magn. Reson. Med.*, vol. 52, no. 2, pp. 376–390, 2004.
- [71] Z.-P. Liang and Z.-P. Liang, "Spatiotemporal Imaging with Partially Separable Functions," *IEEE Int. Symp. Biomed. Imaging*, vol. 2, pp. 988–991, 2007.
- [72] J. Tsao, P. Boesiger, K. P. Pruessmann, T. J1, B. P, and P. KP., "k-t BLAST and k-t SENSE: Dynamic MRI with high frame rate exploiting spatiotemporal correlations," *Magn. Reson. Med.*, vol. 50, no. 5, pp. 1031–1042, 2003.
- [73] H. Pedersen, S. Kozerke, S. Ringgaard, K. Nehrke, W. Kim, and Y. K. Won, "K-t PCA: Temporally constrained k-t BLAST reconstruction using principal component analysis," *Magn. Reson. Med.*, vol. 62, no. 3, pp. 706–716, 2009.
- [74] H. Rauhut, "Sparse Approximation," in *Encyclopedia of applied and computational mathematics*, B. Engquist, Ed. Springer Berlin Heidelberg, 2015, pp. 1344–1349.
- [75] D. L. Donoho, "For most large underdetermined systems of linear equations the minimal l_1 -norm solution is also the sparsest solution," *Comm. Pure Appl. Math.*, vol. 59, no. 6, pp. 797–829, 2006.
- [76] N. Parikh and S. Boyd, "Proximal Algorithms," *Found. Trends Optim.*, vol. 1, no. 3, pp. 127–239, 2014.
- [77] A. Beck and M. Teboulle, "A fast iterative shrinkage-thresholding algorithm," *Soc. Ind. Appl. Math. J. Imaging Sci.*, vol. 2, no. 1, pp. 183–202, 2009.
- [78] S. Boyd *et al.*, "Distributed Optimization and Statistical Learning via the Alternating Direction Method of Multipliers," *Found. Trends Mach. Learn.*, vol. 3, no. 1, pp. 1–122, 2011.

- [79] K. T. Block, M. Uecker, and J. Frahm, "Undersampled radial MRI with multiple coils. Iterative image reconstruction using a total variation constraint," *Magn. Reson. Med. An Off. J. Int. Soc. Magn. Reson. Med.*, vol. 57, no. 6, pp. 1086–1098, 2007.
- [80] J. C. Ye, S. Tak, Y. Han, and H. W. Park, "Projection reconstruction MR imaging using FOCUSS," *Magn. Reson. Med. An Off. J. Int. Soc. Magn. Reson. Med.*, vol. 57, no. 4, pp. 764–775, 2007.
- [81] J. M. Santos *et al.*, "Single breath-hold whole-heart MRA using variable-density spirals at 3T," *Magn. Reson. Med. An Off. J. Int. Soc. Magn. Reson. Med.*, vol. 55, no. 2, pp. 371–379, 2006.
- [82] D. L. Donoho and others, "Compressed sensing," *IEEE Trans. Inf. theory*, vol. 52, no. 4, pp. 1289–1306, 2006.
- [83] E. Candes, J. Romberg, and T. Tao, "Robust uncertainty principles: Exact signal reconstruction from highly incomplete frequency information," *arXiv Prepr. math/0409186*, 2004.
- [84] M. Seeger, H. Nickisch, R. Pohmann, and B. Schölkopf, "Optimization of k-space trajectories for compressed sensing by Bayesian experimental design," *Magn. Reson. Med. An Off. J. Int. Soc. Magn. Reson. Med.*, vol. 63, no. 1, pp. 116–126, 2010.
- [85] T. Wech *et al.*, "Resolution evaluation of MR images reconstructed by iterative thresholding algorithms for compressed sensing," *Med. Phys.*, vol. 39, no. 7Part1, pp. 4328–4338, 2012.
- [86] R. Ahmad, H. Xue, S. Giri, Y. Ding, J. Craft, and O. P. Simonetti, "Variable density incoherent spatiotemporal acquisition (VISTA) for highly accelerated cardiac MRI," *Magn. Reson. Med.*, vol. 74, no. 5, pp. 1266–1278, 2015.
- [87] J. Y. Cheng, T. Zhang, M. T. Alley, M. Lustig, S. S. Vasanawala, and J. M. Pauly, "Variable Density Radial View- Ordering and Sampling for Time-Optimized 3D Cartesian Imaging," *Proc. ISMRM Work. Data Sampl. Image Reconstr.*, p. 3, 2013.
- [88] A. Rich, L. C. Potter, N. Jin, J. Ash, O. P. Simonetti, and R. Ahmad, "A Bayesian model for highly accelerated phase-contrast MRI," *Magn. Reson. Med.*, vol. 76, no. 2, pp. 689–701, 2016.
- [89] M. Lustig, J. M. Santos, D. L. Donoho, and J. M. Pauly, "kt SPARSE: High frame rate dynamic MRI exploiting spatio-temporal sparsity," in *Proceedings of the 13th Annual Meeting of ISMRM, Seattle*, 2006, vol. 2420.
- [90] C. Santelli, M. Loecher, J. Busch, O. Wieben, T. Schaeffter, and S. Kozerke, "Accelerating 4D flow MRI by exploiting vector field divergence regularization," *Magn. Reson. Med.*, vol. 75, no. 1, pp. 115–125, 2016.
- [91] F. Ong *et al.*, "Robust 4D flow denoising using divergence-free wavelet transform," *Magn. Reson. Med.*, vol. 73, no. 2, pp. 828–842, 2015.
- [92] P. D. Tafti, R. Delgado-Gonzalo, A. F. Stalder, and M. Unser, "Variational enhancement and

- denoising of flow field images,” in *2011 IEEE International Symposium on Biomedical Imaging: From Nano to Macro*, 2011, pp. 1061–1064.
- [93] F. Ong, J. Cheng, and M. Lustig, “General phase regularized reconstruction with phase cycling,” *arXiv Prepr. arXiv1709.05374*, vol. 224, no. 3, pp. 12–14, 2017.
- [94] and V. S. L. D. Kim, H. A. Dyvorne, R. Otazo, L. Feng, D. K. Sodickson, “Accelerated Phase-Contrast Cine MRI Using k-t SPARSE-SENSE,” *Magn. Reson. Med.*, vol. 67, no. 4, pp. 1054–1064, 2009.
- [95] J. V. Velikina and A. A. Samsonov, “Reconstruction of dynamic image series from undersampled MRI data using data-driven model consistency condition (MOCCO),” *Magn. Reson. Med.*, vol. 74, no. 5, pp. 1279–1290, 2015.
- [96] J.-F. Cai, E. J. Candès, and Z. Shen, “A singular value thresholding algorithm for matrix completion,” *SIAM J. Optim.*, vol. 20, no. 4, pp. 1956–1982, 2010.
- [97] D. Kim, H. A. Dyvorne, R. Otazo, L. Feng, D. K. Sodickson, and V. S. Lee, “Accelerated phase-contrast cine MRI using k-t SPARSE-SENSE,” *Magn. Reson. Med.*, vol. 67, no. 4, pp. 1054–1064, Apr. 2012.
- [98] J. Trzasko, A. Manduca, and E. Borisch, “Local versus global low-rank promotion in dynamic MRI series reconstruction,” in *Proceedings of the 19th Annual Meeting of ISMRM*, 2011, p. 4371.
- [99] D. Giese, T. Schaeffter, and S. Kozerke, “Highly undersampled phase-contrast flow measurements using compartment-based k-t principal component analysis,” *Magn. Reson. Med.*, 2013.
- [100] J. He, Q. Liu, A. Christodoulou, C. Ma, F. Lam, and Z.-P. Liang, “Accelerated High-Dimensional MR Imaging With Sparse Sampling Using Low-Rank Tensors,” *IEEE Trans. Med. Imaging*, vol. 0062, no. c, pp. 1–1, 2016.
- [101] A. G. Christodoulou *et al.*, “Magnetic resonance multitasking for motion-resolved quantitative cardiovascular imaging,” *Nat. Biomed. Eng.*, vol. 2, no. 4, pp. 215–226, Apr. 2018.
- [102] L. R. Tucker, “Some mathematical notes on three-mode factor analysis,” *Psychometrika*, vol. 31, no. 3, pp. 279–311, 1966.
- [103] B. A. Runderkamp *et al.*, “Accelerated 4D flow MRI using a Low-Rank Tensor reconstruction,” in *Proc. Intl. Soc. Mag. Reson. Med. 27 (2019)*, 2019, p. 1958.
- [104] E. J. Candès, X. Li, Y. Ma, and J. Wright, “Robust principal component analysis?,” *J. ACM*, vol. 58, no. 3, p. 11, 2011.
- [105] B. Tremoulheac, N. Dikaios, D. Atkinson, and S. R. Arridge, “Dynamic MR image reconstruction-separation from undersampled (k,t)-Space via low-rank plus sparse prior,” *IEEE Trans. Med.*

- Imaging*, vol. 33, no. 8, pp. 1689–1701, 2014.
- [106] J. Caballero, A. N. Price, D. Rueckert, and J. V. Hajnal, “Dictionary learning and time sparsity for dynamic MR data reconstruction,” *IEEE Trans. Med. Imaging*, vol. 33, no. 4, pp. 979–994, 2014.
- [107] S. G. Lingala and M. Jacob, “Blind compressive sensing dynamic MRI,” *IEEE Trans. Med. Imaging*, vol. 32, no. 6, pp. 1132–1145, 2013.
- [108] S. Ravishankar and Y. Bresler, “MR image reconstruction from highly undersampled k-space data by dictionary learning,” *IEEE Trans. Med. Imaging*, vol. 30, no. 5, pp. 1028–1041, 2011.
- [109] J. F. M. Schmidt and S. Kozerke, “Dynamic Cardiac MR Image Reconstruction Models Using Machine Learning on Large Training Data Sets,” in *Proceedings of the 25th Annual Meeting of ISMRM, Honolulu, Hawaii, USA, 2017*, p. 3991.
- [110] K. Hammernik *et al.*, “Learning a variational network for reconstruction of accelerated MRI data,” *Magn. Reson. Med.*, vol. 79, no. 6, pp. 3055–3071, 2018.
- [111] M. Mardani *et al.*, “Deep generative adversarial neural networks for compressive sensing MRI,” *IEEE Trans. Med. Imaging*, vol. 38, no. 1, pp. 167–179, 2018.
- [112] M. Akçakaya, S. Moeller, S. Weingärtner, and K. Uğurbil, “Scan-specific robust artificial-neural-networks for k-space interpolation (RAKI) reconstruction: Database-free deep learning for fast imaging,” *Magn. Reson. Med.*, vol. 81, no. 1, pp. 439–453, 2019.
- [113] I. Goodfellow, Y. Bengio, and A. Courville, *Deep learning*. MIT press, 2016.
- [114] B. Zhu, J. Z. Liu, S. F. Cauley, B. R. Rosen, and M. S. Rosen, “Image reconstruction by domain-transform manifold learning,” *Nature*, vol. 555, no. 7697, p. 487, 2018.
- [115] K. H. Jin, M. T. McCann, E. Froustey, and M. Unser, “Deep convolutional neural network for inverse problems in imaging,” *IEEE Trans. Image Process.*, vol. 26, no. 9, pp. 4509–4522, 2017.
- [116] A. Hauptmann, S. Arridge, F. Lucka, V. Muthurangu, and J. A. Steeden, “Real-time cardiovascular MR with spatio-temporal artifact suppression using deep learning--proof of concept in congenital heart disease,” *Magn. Reson. Med.*, vol. 81, no. 2, pp. 1143–1156, 2019.
- [117] G. Yang *et al.*, “DAGAN: deep de-aliasing generative adversarial networks for fast compressed sensing MRI reconstruction,” *IEEE Trans. Med. Imaging*, vol. 37, no. 6, pp. 1310–1321, 2017.
- [118] V. Antun, F. Renna, C. Poon, B. Adcock, and A. C. Hansen, “On instabilities of deep learning in image reconstruction-Does AI come at a cost?,” *arXiv Prepr. arXiv1902.05300*, 2019.
- [119] J. Schlemper, J. Caballero, J. V. Hajnal, A. N. Price, and D. Rueckert, “A Deep Cascade of Convolutional Neural Networks for Dynamic MR Image Reconstruction,” *IEEE Trans. Med. Imaging*, vol. 37, no. 2, pp. 491–503, 2018.

- [120] M. Mardani, Q. Sun, S. Vasawanala, and V. Pappas, "Neural Proximal Gradient Descent for Compressive Imaging," no. Nips, pp. 1–11, 2018.
- [121] J. Y. Cheng, F. Chen, C. Sandino, M. Mardani, J. M. Pauly, and S. S. Vasanawala, "Compressed Sensing: From Research to Clinical Practice with Data-Driven Learning," pp. 1–18, 2019.
- [122] H. K. Aggarwal, M. P. Mani, and M. Jacob, "MoDL: Model-Based Deep Learning Architecture for Inverse Problems," *IEEE Trans. Med. Imaging*, vol. 38, no. 2, pp. 394–405, 2019.
- [123] K. Gregor and Y. LeCun, "Learning fast approximations of sparse coding," in *Proceedings of the 27th International Conference on International Conference on Machine Learning*, 2010, pp. 399–406.
- [124] S. Roth and M. J. Black, "Fields of experts," *Int. J. Comput. Vis.*, vol. 82, no. 2, p. 205, 2009.
- [125] I. Goodfellow *et al.*, "Generative adversarial nets," in *Advances in neural information processing systems*, 2014, pp. 2672–2680.
- [126] D. Narnhofer, K. Hammernik, F. Knoll, and T. Pock, "Inverse GANs for accelerated MRI reconstruction," in *Wavelets and Sparsity XVIII*, 2019, vol. 11138, p. 111381A.
- [127] F. Knoll, K. Hammernik, E. Kobler, T. Pock, M. P. Recht, and D. K. Sodickson, "Assessment of the generalization of learned image reconstruction and the potential for transfer learning," *Magn. Reson. Med.*, May 2018.
- [128] C. Binter, U. Gülan, M. Holzner, and S. Kozerke, "On the accuracy of viscous and turbulent loss quantification in stenotic aortic flow using phase-contrast MRI," *Magn. Reson. Med.*, vol. 76, no. 1, pp. 191–196, 2016.
- [129] T. Küstner *et al.*, "MR image reconstruction using a combination of compressed sensing and partial Fourier acquisition: ESPReSSo," *IEEE Trans. Med. Imaging*, vol. 35, no. 11, pp. 2447–2458, 2016.
- [130] G. Szarf *et al.*, "Zero filled partial Fourier phase contrast MR imaging: In vitro and in vivo assessment," *J. Magn. Reson. Imaging*, vol. 23, no. 1, pp. 42–49, 2006.
- [131] T. K. F. Foo, "Producing a phase contrast MR image from a partial Fourier data acquisition. US Patent 6,393,313 B1. August 23, 2000," US6393313 B1, 2002.
- [132] G. Li *et al.*, "An L1-norm phase constraint for half-Fourier compressed sensing in 3D MR imaging," *Magn. Reson. Mater. Physics, Biol. Med.*, vol. 28, no. 5, pp. 459–472, 2015.
- [133] M. Doneva, P. Börnert, H. Eggers, and A. Mertins, "Partial Fourier compressed sensing," *Proc. Int. Soc. Magn. Reson. Med.*, vol. 18, p. 4851, 2010.
- [134] S. Ma, W. Yin, Y. Zhang, and A. Chakraborty, "An efficient algorithm for compressed MR imaging

- using total variation and wavelets,” in *IEEE International Conference on Computer Vision and Pattern Recognition (CVPR) 2008*, 2008, pp. 1–8.
- [135] M. B. Scheidegger, S. E. Maier, and P. Boesiger, “FID-Acquired-Echos (FAcE): A short echo time imaging method for flow artefact suppression,” *Magn. Reson. Imaging*, vol. 9, no. 4, pp. 517–524, 1991.
- [136] J. C. Gatenby and J. C. Gore, “Mapping of turbulent intensity by magnetic resonance imaging,” *Journal of Magnetic Resonance, Series B*, vol. 104, no. 2, pp. 119–126, 1994.
- [137] K. S. Nayak *et al.*, “Cardiovascular magnetic resonance phase contrast imaging,” *J. Cardiovasc. Magn. Reson.*, vol. 17, no. 1, p. 71, Jan. 2015.
- [138] M. A. Bernstein, K. F. King, and X. J. Zhou, *Handbook of MRI pulse sequences*. Elsevier, 2004.
- [139] P. Margosian and F. Schmitt, “Faster MR imaging: imaging with half the data,” *Heal. Care Instrum.*, vol. 1, no. 6, pp. 195–197, 1986.
- [140] Z. Liang, F. E. Boda, R. T. Constable, E. M. Haacke, P. C. Lauterbur, and M. R. Smith, “Constrained reconstruction methods in MR imaging,” *Rev. Magn. Reson. Med.*, vol. 4, no. 217, pp. 67–185, 1992.
- [141] A. A. Samsonov, E. G. Kholmovski, D. L. Parker, and C. R. Johnson, “POCSense: POCS-based reconstruction for sensitivity encoded magnetic resonance imaging,” *Magn. Reson. Med.*, vol. 52, no. 6, pp. 1397–1406, 2004.
- [142] H. Jasak, A. Jemcov, Z. Tukovic, and others, “OpenFOAM: A C++ library for complex physics simulations,” in *International workshop on coupled methods in numerical dynamics*, 2007, vol. 1000, pp. 1–20.
- [143] M. Guerquin-Kern, L. Lejeune, K. P. Pruessmann, and M. Unser, “Realistic analytical phantoms for parallel magnetic resonance imaging,” *IEEE Trans. Med. Imaging*, vol. 31, no. 3, pp. 626–636, 2012.
- [144] M. A. Bernstein *et al.*, “Concomitant gradient terms in phase contrast MR: Analysis and correction,” *Magn. Reson. Med.*, vol. 39, no. 2, pp. 300–308, 1998.
- [145] P. G. Walker, G. B. Cranney, M. B. Scheidegger, G. Waseleski, G. M. Pohost, and A. P. Yoganathan, “Semiautomated method for noise reduction and background phase error correction in MR phase velocity data,” *J. Magn. Reson. Imaging*, vol. 3, no. 3, pp. 521–530, 1993.
- [146] F. Ong *et al.*, “Berkeley advanced reconstruction toolbox,” *Magn. Reson. Med.*, vol. 73, no. 2, pp. 828–842, 2015.
- [147] P. Liang, Zhi-pei; Lauterbur, “Chapter 8 Image Resolution, Noise, and Artifacts,” *Princ. Magn. Reson. Imaging A Signal Process. Perspect.*, pp. 233–290.

- [148] K. R. O'Brien, B. R. Cowan, M. Jain, R. A. H. Stewart, A. J. Kerr, and A. A. Young, "MRI phase contrast velocity and flow errors in turbulent stenotic jets," *J. Magn. Reson. Imaging*, vol. 28, no. 1, pp. 210–218, 2008.
- [149] K. R. O'Brien, R. S. Gabriel, A. Greiser, B. R. Cowan, A. A. Young, and A. J. Kerr, "Aortic valve stenotic area calculation from phase contrast cardiovascular magnetic resonance: The importance of short echo time," *J. Cardiovasc. Magn. Reson.*, vol. 11, no. 1, pp. 1–12, 2009.
- [150] M. Bydder and M. D. Robson, "Partial fourier partially parallel imaging," *Magn. Reson. Med.*, vol. 53, no. 6, pp. 1393–1401, 2005.
- [151] V. Knobloch, P. Boesiger, and S. Kozerke, "Sparsity transform k-t principal component analysis for accelerating cine three-dimensional flow measurements," *Magn. Reson. Med.*, vol. 70, no. 1, pp. 53–63, 2013.
- [152] U. Tariq, A. Hsiao, M. Alley, T. Zhang, M. Lustig, and S. S. Vasanawala, "Venous and arterial flow quantification are equally accurate and precise with parallel imaging compressed sensing 4D phase contrast MRI," *J. Magn. Reson. Imaging*, vol. 37, no. 6, pp. 1419–1426, 2013.
- [153] D. Giese, J. Wong, G. F. Greil, M. Buehrer, T. Schaeffter, and S. Kozerke, "Towards highly accelerated Cartesian time-resolved 3D flow cardiovascular magnetic resonance in the clinical setting," *J. Cardiovasc. Magn. Reson.*, vol. 16, no. 1, p. 42, 2014.
- [154] S. Schnell *et al.*, "k-t GRAPPA accelerated four-dimensional flow MRI in the aorta: effect on scan time, image quality, and quantification of flow and wall shear stress," *Magn. Reson. Med.*, vol. 72, no. 2, pp. 522–533, 2014.
- [155] T. Gu *et al.*, "PC VIPR: a high-speed 3D phase-contrast method for flow quantification and high-resolution angiography," *Am. J. Neuroradiol.*, vol. 26, no. 4, pp. 743–749, Apr. 2005.
- [156] A. Sigfridsson, S. Petersson, C.-J. Carlhäll, and T. Ebbers, "Four-dimensional flow MRI using spiral acquisition," *Magn. Reson. Med.*, vol. 68, no. 4, pp. 1065–1073, 2012.
- [157] Y. Kwak *et al.*, "Accelerated aortic flow assessment with compressed sensing with and without use of the sparsity of the complex difference image," *Magn. Reson. Med.*, vol. 70, no. 3, pp. 851–858, 2013.
- [158] L. Feng *et al.*, "5D whole-heart sparse MRI," *Magn. Reson. Med.*, vol. 79, no. 2, pp. 826–838, Feb. 2018.
- [159] R. Bastkowski, K. Weiss, D. Maintz, and D. Giese, "Self-Gated Golden-Angle Spiral 4D Flow MRI," in *Proceedings of the 26th Annual Meeting of ISMRM. Presented at the ISMRM.*, 2018, vol. 80, no. 3, p. 3443.
- [160] T. Zhang, J. Y. Cheng, Y. Chen, D. G. Nishimura, J. M. Pauly, and S. S. Vasanawala, "Robust self-

- navigated body MRI using dense coil arrays," *Magn. Reson. Med.*, vol. 76, no. 1, pp. 197–205, 2016.
- [161] S. Wundrak, J. Paul, J. Ulrici, E. Hell, and V. Rasche, "A small surrogate for the golden angle in time-resolved radial MRI based on generalized fibonacci sequences," *IEEE Trans. Med. Imaging*, vol. 34, no. 6, pp. 1262–1269, 2015.
- [162] A. C. Larson *et al.*, "Preliminary investigation of respiratory self-gating for free-breathing segmented cine MRI," *Magn. Reson. Med.*, vol. 53, no. 1, pp. 159–168, 2005.
- [163] V. Rasche, R. W. De Boer, D. Holz, and R. Proksa, "Continuous radial data acquisition for dynamic MRI," *Magn. Reson. Med.*, vol. 34, no. 5, pp. 754–761, 1995.
- [164] S. Zhang, K. T. Block, and J. Frahm, "Magnetic resonance imaging in real time: Advances using radial FLASH," *J. Magn. Reson. Imaging*, vol. 31, no. 1, pp. 101–109, 2010.
- [165] V. Knobloch *et al.*, "Mapping mean and fluctuating velocities by Bayesian multipoint MR velocity encoding-validation against 3D particle tracking velocimetry," *Magn. Reson. Med.*, vol. 71, no. 4, pp. 1405–1415, 2014.
- [166] M. Buehrer, K. P. Pruessmann, P. Boesiger, and S. Kozerke, "Array compression for MRI with large coil arrays," *Magn. Reson. Med.*, vol. 57, no. 6, pp. 1131–1139, 2007.
- [167] J. I. Tamir, F. Ong, J. Y. Cheng, M. Uecker, and M. Lustig, "Generalized Magnetic Resonance Image Reconstruction using The Berkeley Advanced Reconstruction Toolbox," in *Proceedings of the ISMRM 2016 Data Sampling and Image Reconstruction Workshop*, 2016, vol. 2486, p. 9660006.
- [168] J. Snoek, H. Larochelle, and R. P. Adams, "Practical Bayesian Optimization of Machine Learning Algorithms," *Adv. Neural Inf. Process. Syst.*, pp. 2951–2959, 2012.
- [169] J. Busch, D. Giese, and S. Kozerke, "Image-based background phase error correction in 4D flow MRI revisited," *J. Magn. Reson. Imaging*, pp. 1–10, 2017.
- [170] D. G. Altman and J. M. Bland, "Measurement in medicine: the analysis of method comparison studies," *Stat.*, pp. 307–317, 1983.
- [171] Y. Wang, S. J. Riederer, and R. L. Ehman, "Respiratory Motion of the Heart: Kinematics and the Implications for the Spatial Resolution in Coronary Imaging," *Magn. Reson. Med.*, vol. 33, no. 5, pp. 713–719, 1995.
- [172] A. T. Lee, G. Bruce Pike, and N. J. Pelc, "Three-point phase-contrast velocity measurements with increased velocity-to-noise ratio," *Magn. Reson. Med.*, vol. 33, no. 1, pp. 122–126, 1995.
- [173] A. Herment *et al.*, "Improved estimation of velocity and flow rate using regularized three-point phase-contrast velocimetry," *Magn. Reson. Med. An Off. J. Int. Soc. Magn. Reson. Med.*, vol. 44,

- no. 1, pp. 122–128, 2000.
- [174] M. Gewillig, “The Fontan circulation,” *Heart*, vol. 91, no. 6, pp. 839–846, 2005.
- [175] K. Jarvis *et al.*, “Caval to pulmonary 3D flow distribution in patients with Fontan circulation and impact of potential 4D flow MRI error sources,” *Magn. Reson. Med.*, no. February 2017, pp. 1205–1218, 2018.
- [176] V. Vishnevskiy, S. J. Sanabria, and O. Goksel, “Image Reconstruction via Variational Network for Real-Time Hand-Held Sound-Speed Imaging,” in *International Workshop on Machine Learning for Medical Image Reconstruction*, 2018, pp. 120–128.
- [177] J. Walheim, H. Dillinger, and S. Kozerke, “Multipoint 5D Flow Cardiovascular Magnetic Resonance - Accelerated Cardiac- and Respiratory-Motion Resolved Mapping of Mean and Turbulent Velocities,” *J. Cardiovasc. Magn. Reson.*, 2019.
- [178] S. Zhao, L. C. Potter, N. Jin, Y. Liu, S. Orlando P, and R. Ahmad, “PC-MRI with Phase Recovery from Multiple Wrapped Measurements (PRoM),” in *Annual Meeting ISMRM-ESMRMB, June 16-21 2018*, 2018.
- [179] S. W. Funke, M. Nordaas, Ø. Evju, M. S. Alnæs, and K. A. Mardal, “Variational data assimilation for transient blood flow simulations: Cerebral aneurysms as an illustrative example,” *Int. j. numer. method. biomed. eng.*, no. April 2017, pp. 1–27, 2018.
- [180] J. Garcia *et al.*, “Distribution of blood flow velocity in the normal aorta: Effect of age and gender,” *J. Magn. Reson. Imaging*, vol. 47, no. 2, pp. 487–498, 2018.
- [181] M. Grigioni, C. Daniele, G. D’Avenio, and V. Barbaro, “A discussion on the threshold limit for hemolysis related to Reynolds shear stress,” *J. Biomech.*, vol. 32, no. 10, pp. 1107–1112, 1999.
- [182] P. C. Lu, H. C. Lai, and J. S. Liu, “A reevaluation and discussion on the threshold limit for hemolysis in a turbulent shear flow,” *J. Biomech.*, vol. 34, no. 10, pp. 1361–1364, 2001.
- [183] A. P. Yoganathan, Y.-R. R. Woo, and H.-W. W. Sung, “Turbulent shear stress measurements in the vicinity of aortic heart valve prostheses,” *J. Biomech.*, vol. 19, no. 6, pp. 433–442, 1986.
- [184] A. P. Yoganathan, K. B. Chandran, and F. Sotiropoulos, “Flow in prosthetic heart valves: State-of-the-art and future directions,” *Ann. Biomed. Eng.*, vol. 33, no. 12 SPEC. ISS., pp. 1689–1694, 2005.
- [185] J. Walheim, V. Vishnevskiy, and S. Kozerke, “FlowNet: High-Speed Compressed Sensing 4D Flow MRI Image Reconstruction using Loop Unrolling,” in *Proceedings of the 27th Annual Meeting of ISMRM.*, 2019, p. 4653.
- [186] Y. Fung, *Biodynamics: circulation*. New York-Berlin-Heidelberg-Tokyo: Springer, 1984.

- [187] U. Gülan, B. Lüthi, M. Holzner, A. Liberzon, A. Tsinober, and W. Kinzelbach, "Experimental study of aortic flow in the ascending aorta via particle tracking velocimetry," *Exp. Fluids*, vol. 53, no. 5, pp. 1469–1485, 2012.
- [188] P. A. Yushkevich, Y. Gao, and G. Gerig, "ITK-SNAP: An interactive tool for semi-automatic segmentation of multi-modality biomedical images," in *2016 38th Annual International Conference of the IEEE Engineering in Medicine and Biology Society (EMBC)*, 2016, pp. 3342–3345.
- [189] P. Robson, A. Grant, A. Madhuranthakam, R. Lattanzi, D. Sodickson, and C. Mckenzie, "Comprehensive Quantification of SNR Ratio and g-Factor for Image-Based and k-space Based Parallel Imaging Reconstructions," vol. 60, no. 4, pp. 895–907, 2010.
- [190] M. Rosenblatt, "Remarks on some nonparametric estimates of a density function," *Ann. Math. Stat.*, pp. 832–837, 1956.
- [191] E. Parzen, "On estimation of a probability density function and mode," *Ann. Math. Stat.*, vol. 33, no. 3, pp. 1065–1076, 1962.
- [192] J. Walheim, A. Gotschy, and S. Kozerke, "On the limitations of partial Fourier acquisition in phase-contrast MRI of turbulent kinetic energy," *Magn. Reson. Med.*, vol. 81, no. 1, pp. 514–523, 2019.
- [193] L. E. Ma *et al.*, "Aortic 4D flow MRI in 2 minutes using compressed sensing, respiratory controlled adaptive k-space reordering, and inline reconstruction," *Magn. Reson. Med.*, vol. 81, no. 6, pp. 3675–3690, 2019.
- [194] A. Rich, L. C. Potter, N. Jin, Y. Liu, O. P. Simonetti, and R. Ahmad, "A Bayesian approach for 4D flow imaging of aortic valve in a single breath-hold," *Magn. Reson. Med.*, vol. 81, no. 2, pp. 811–824, 2019.
- [195] A. K. Maier *et al.*, "Learning with known operators reduces maximum error bounds," *Nat. Mach. Intell.*, vol. 1, no. 8, pp. 373–380, 2019.
- [196] T. Zhang, J. M. Pauly, S. S. Vasanawala, and M. Lustig, "Coil compression for accelerated imaging with Cartesian sampling," *Magn. Reson. Med.*, vol. 69, no. 2, pp. 571–582, 2013.
- [197] L. Landweber, "An iteration formula for Fredholm integral equations of the first kind," *Am. J. Math.*, vol. 73, no. 3, pp. 615–624, 1951.
- [198] Y. Liu and M. S. Lew, "Learning relaxed deep supervision for better edge detection," in *Proceedings of the IEEE Conference on Computer Vision and Pattern Recognition*, 2016, pp. 231–240.
- [199] D. Lee, J. Yoo, and J. C. Ye, "Deep artifact learning for compressed sensing and parallel MRI,"

- arXiv Prepr. arXiv1703.01120*, 2017.
- [200] M. Abadi *et al.*, “Tensorflow: A system for large-scale machine learning,” in *12th Symposium on Operating Systems Design and Implementation*, 2016, pp. 265–283.
- [201] Y. LeCun, D. Touresky, G. Hinton, and T. Sejnowski, “A theoretical framework for back-propagation,” in *Proceedings of the 1988 connectionist models summer school*, 1988, vol. 1, pp. 21–28.
- [202] J. Domke, “Generic methods for optimization-based modeling,” in *Artificial Intelligence and Statistics*, 2012, pp. 318–326.
- [203] Y. Yang, J. Sun, H. Li, and Z. Xu, “Deep ADMM-Net for Compressive Sensing MRI,” *Nips*, no. Nips, pp. 10–18, 2016.
- [204] V. Vishnevskiy, R. Rau, and O. Goksel, “Deep Variational Networks with Exponential Weighting for Learning Computed Tomography,” *arXiv Prepr. arXiv1906.05528*, 2019.
- [205] T. Hoh, J. Walheim, M. Gastl, A. Gotschy, and S. Kozerke, “Partial Fourier Acquisitions in Myocardial First Pass Perfusion Revisited,” in *Proceedings of the 26th Annual Meeting of ISMRM.*, 2018, p. 3517.
- [206] S. Gross, C. Barmet, B. E. Dietrich, D. O. Brunner, T. Schmid, and K. P. Pruessmann, “Dynamic nuclear magnetic resonance field sensing with part-per-trillion resolution,” *Nat. Commun.*, vol. 7, p. 13702, 2016.
- [207] D. S. Goolaub *et al.*, “Multidimensional fetal flow imaging with cardiovascular magnetic resonance: a feasibility study,” *J. Cardiovasc. Magn. Reson.*, vol. 20, no. 1, p. 77, 2018.
- [208] J. Stepišnik, “Measuring and imaging of flow by NMR,” *Prog. Nucl. Magn. Reson. Spectrosc.*, vol. 17, no. C, pp. 187–209, 1985.
- [209] P. T. Callaghan and J. Stepišnik, “Frequency-domain analysis of spin motion using modulated-gradient NMR.” Academic Press, 1995.
- [210] J.-F. Nielsen and K. S. Nayak, “SSFP and GRE phase contrast imaging using a three-echo readout,” *Magn. Reson. Med. An Off. J. Int. Soc. Magn. Reson. Med.*, vol. 58, no. 6, pp. 1288–1293, 2007.
- [211] A. M. Sallam and N. H. C. Hwang, “Human red blood cell hemolysis in a turbulent shear flow: contribution of Reynolds shear stresses,” *Biorheology*, vol. 21, no. 6, pp. 783–797, 1984.
- [212] B. E. Stähli *et al.*, “Impact of three-dimensional imaging and pressure recovery on echocardiographic evaluation of severe aortic stenosis: a pilot study,” *Echocardiography*, vol. 31, no. 8, pp. 1006–1016, 2014.

- [213] M. Froeling, E. Farag, R. N. Planken, T. Leiner, and P. van Ooij, "Machine learning for automatic three-dimensional segmentation of the aorta in 4D flow MRI," in *Proceedings of the 27th Annual Meeting of ISMRM.*, 2019, p. 0088.
- [214] O. Ronneberger, P. Fischer, and T. Brox, "U-net: Convolutional networks for biomedical image segmentation," in *International Conference on Medical image computing and computer-assisted intervention*, 2015, pp. 234–241.

Chapter 10 Acknowledgements

I would like to thank everyone who contributed to this thesis, paved the way in front of me, and kept me company and supported me throughout the last years.

First of all, I would like to express my gratitude to Prof. Dr. Sebastian Kozerke who gave me the opportunity to conduct a PhD project under his supervision. His office door was always open and I highly valued his prompt and constructive feedback which allowed me to rapidly progress in my research, his openness to new ideas, and the trust he gave me in letting me work very independently. In addition, I would like to thank Prof. Dr. Michael Markl for being co-referee and for taking the time to review my thesis.

Many thanks go to Dr. Christian Binter who introduced me to the research topic and ensured that I had a good start at IBT. I am particularly grateful for the detailed documentation and the massive amount of data and code he provided me with and on which I could build upon in my own research.

Furthermore, I would like to thank Hannes Dillinger for the great collaboration, discussions, and fun we had in the flow team and beyond.

I would like to thank Alexander Gotschy for organizing the patient scans and providing input from the clinical side.

My gratitude goes to the Gyrotools team and in particular Gérard Crelier and Martin Bühner for their advice and their software.

My gratitude also goes to Isabell Spiess who took care of everything organizational in the background.

I would like to thank Roger Luechinger for ensuring the operation of our scanners and helping me with advice whenever I had issues with the change of software releases, the scanner environment crashing, etc.

Many thanks go to my officemates Robbert van Gorkum, Christian Günthner, Tobias Hoh, Hannes Dillinger, Mareike Gastl, Johanna Stimm, and Jonathan Weine for the great working atmosphere and the many discussions over coffee and beer. This extends to all other former and current members of the Cardio group, Mohammed Albannay, Ezgi Berberoglu, Patrick Bosshard, Stefano Buoso, Julia Busch, Christian Binter, Constantin von Deuster, Andreas Dounas, Christian Federau, Max Fütterer, Alexander Gotschy, Dian Liu, Claudio Santelli, Beat Schuler, Thomas Joyce, Grzegorz Kwiatkowski, Sophie Peereboom, Orso Pusterla, Georg Spinner, Jonas Steinhauser, Christian Stoeck, Julia Trächtler, Valery Vishnevskiy, Jochen von Spiczak, Patrick Wespi, Conny Waschkies, Lukas Wissmann, Gevin von Witte, Javier Montoya Zegarra, as well as everyone from the hardware group. Thanks for making IBT such a

pleasant working environment with such a great social life. I will keep in memory many great moments in the coffee corner, when going for after work drinks, at ski weekends, etc.

Last but not least, I would like to express my deep gratitude to my family and friends who were of great support during the last years and before and supported me throughout all the ups and downs. Thank you!

Chapter 11 List of Publications

Peer-Reviewed Publications

2019

V. Vishnevskiy, J. Walheim, and S. Kozerke, "Deep Variational Network for Rapid 4D Flow MRI Reconstruction," In Submission, 2019.

J. Walheim, H. Dillinger, A. Gotschy, and S. Kozerke, "5D Flow Tensor MRI to Efficiently Map Reynolds Stresses of Aortic Blood Flow In-Vivo," Sci Rep, in revision, 2019.

J. Walheim, H. Dillinger, and S. Kozerke, "Multipoint 5D Flow Cardiovascular Magnetic Resonance - Accelerated Cardiac- and Respiratory-Motion Resolved Mapping of Mean and Turbulent Velocities," J. Cardiovasc. Magn. Reson., 2019.

J. Walheim, A. Gotschy, and S. Kozerke, "On the limitations of partial Fourier acquisition in phase-contrast MRI of turbulent kinetic energy," Magn. Reson. Med., vol. 81, no. 1, pp. 514–523, 2019.

Conference Proceedings

2019

J. Walheim, V. Vishnevskiy, and S. Kozerke, "FlowNet: High-Speed Compressed Sensing 4D Flow MRI Image Reconstruction using Loop Unrolling," in Proceedings of the 27th Annual Meeting of ISMRM. , 2019, p. 4653.

J. Walheim, H. Dillinger, and S. Kozerke, "5D Flow Tensor MRI for Mapping Reynolds Stresses in the Aorta," in Proceedings of the 27th Annual Meeting of ISMRM. , 2019, p. 0089.

J. Walheim, H. Dillinger, and S. Kozerke, "Multi-Point 5D Flow MRI - Accelerated Cardiac- and Respiratory-Motion Resolved Mapping of Mean and Turbulent Velocities in 4 Minutes," in Proceedings of the 27th Annual Meeting of ISMRM. , 2019, p. 1179.

V. Vishnevskiy, J. Walheim, and S. Kozerke, "Probabilistic Optimization of Cartesian k-Space Undersampling Patterns for Learning-Based Reconstruction," in Proceedings of the 27th Annual Meeting of ISMRM. , 2019, p. 4777.

J. Walheim, H. Dillinger, R. Droste, and S. Kozerke, "5D Flow MRI – Respiratory-motion resolved quantification of flow and turbulent kinetic energy with compressed sensing and Bayesian multipoint velocity unfolding," in SCMR 22nd annual scientific sessions, 2019.

2018

Jonas Walheim and Sebastian Kozerke, "5D Flow MRI – Respiratory Motion Resolved Accelerated 4D Flow Imaging Using Low-Rank + Sparse Reconstruction," in Proceedings of the 26th Annual Meeting of ISMRM. , 2018, p. 0032.

J. Walheim, C. Santelli, and S. Kozerke, "k-t2 ESPIRiT – Image reconstruction of respiratory motion resolved undersampled 4D Flow MRI data in a higher-dimensional subspace," in Proceedings of the 26th Annual Meeting of ISMRM. , 2018, p. 4914.

V. Vishnevskiy, J. Walheim, H. Dillinger, and S. Kozerke, "Easy-to-Implement and Rapid Image Reconstruction of Accelerated Cine and 4D Flow MRI Using TensorFlow," in Proceedings of the 26th Annual Meeting of ISMRM. , 2018, p. 3522.

T. Hoh, J. Walheim, M. Gastl, A. Gotschy, and S. Kozerke, "Partial Fourier Acquisitions in Myocardial First Pass Perfusion Revisited," in Proceedings of the 26th Annual Meeting of ISMRM. , 2018, p. 3517.

2017

J. Walheim and S. Kozerke, "On Partial Fourier Acquisition in 4D Flow MRI of Mean Velocities and Turbulent Kinetic Energy," in Proceedings of the 25th Annual Meeting of ISMRM. , 2017, p. 3226.